Inducing and Controlling Particle Motion in an Optical Trap

Dissertation
submitted to the Physics Department
of the Ludwig-Maximilians-Universität München
by

Spas Nedev Nedev
of
Plovdiv, Bulgaria

München, July 21st, 2015

The cover image of this dissertation is designed by Nanosystems Initiative Munich. It illustrates two plasmonic Janus particles, one of which is in a laser trap.

First reviewer:	Prof. Dr. Jochen Feldmann
Second reviewer:	Prof. Dr. Dieter Braun

Date of the oral examination: 20.10.2015

Scientific publications of results presented in this work

- Spas Nedev, Sol Carretero-Palacios, Paul Kühler, Theobald Lohmüller, Alexander S. Urban, Lindsey J. E. Anderson, and Jochen Feldmann
  An Optically Controlled Microscale Elevator Using Plasmonic Janus Particles
  ACS Photonics 2 (4), 491–496 (2015)

- Spas Nedev, S. Carretero-Palacios, S. R. Kirchner, F. Jäckel, and J. Feldmann
  Microscale Mapping of Oscillatory Flows
  Applied Physics Letters 105, 161113 (2014)

Further scientific publications

- Silke R. Kirchner, Spas Nedev, Sol Carretero-Palacios, Andreas Mader, Madeleine Opitz, Theobald Lohmüller, and Jochen Feldmann
  Direct optical monitoring of flow generated by bacterial flagellar rotation
  Applied Physics Letters 104, 093701 (2014)

Contributions to conferences and workshops

- Talk
  An Optically Controlled Microscale Elevator Using Plasmonic Janus Particles
  Internal Workshop on Photonics and Optoelectronics, Riezlern, Austria, September 2014

- Talk
  Optical Trapping and Lifting of Plasmonic Janus Particles
  SPIE Optics + Photonics, San Diego, California, August 2014

- Talk
  Microscale Mapping of Oscillatory Flows
  DPG Spring Meeting, Berlin, Dresden, April 2014

- Poster presentation
  Optical Control of Plasmonic Janus Particles
  CeNS Workshop Venice 2013 "Nanosciences: Great Adventures on Small Scales", San Servolo/Venice, Italy, September 2013

- Invited talk
  Parallel Laser Printing of Nanoparticles
  Lasers and Electro-Optics (CLEO), 2012 Conference, San Jose, California, May 2012

- Talk
  Optical Force Stamping Lithography
  DPG Spring Meeting, Berlin, March 2012

- Talk
  Optical Force Stamping Lithography
  From Biophotonics to Optoelectronics, Riezlern, Austria, October 2011

- Poster presentation
  Laser Printing of Nanoparticles in Parallel CeNS Workshop Venice 2011, San Servolo/Venice, Italy, September 2011

Table of Contents

Kurzfassung

Optische Kräfte, verursacht durch Wechselwirkungen zwischen Licht und Materie, ermöglichen die kontaktfreie Manipulation von Mikro- und Nanopartikeln. Optische Pinzetten können dazu benutzt werden, auf einzelne Partikel Kräfte auszuüben und auf sie wirkende, externe Krüfte zu bestimmen. In dieser Arbeit werden optische Kräfte dazu benutzt, lichtangetriebene Partikel (Mikroschwimmer) zu fangen, auszurichten und ihre Bewegung zu kontrollieren. Außerdem werden optische Kräfte dazu benutzt, mikrometergroße Oszillatoren anzutreiben und die Geschwindigkeit der oszillierenden Strömung um diesen Oszillator zu messen.

Janusparticel, die aus zwei Hemisphären mit unterschiedlichen physikalischen oder chemischen Eigenschaften bestehen, sind eine der einfachsten Implementationen von Mikroschwimmern. Im ersten Teil dieser Arbeit wird gezeigt, wie plasmonische Janusparticel mit einer optischen Pinzete stabil gefangen und durch ein Zusammenspiel optischer und thermischer Kräfte kontrolliert entlang der Strahlachse des Lasers bewegt werden können. Eine Reihe von Experimenten zeigt, dass Streukräfte das Partikel räumlich ausrichten, während starke Absorption auf der Metallseite einen thermischen Gradienten induziert, der die Bewegung des Partikels bewirkt. Es wird gezeigt, dass eine Erhöhung der Laserleistung zu einer Aufwärtsbewegung, eine Absenkung hingegen zu einer Abwärtsbewegung führt. Bei der Untersuchung der umkehrbaren axialen Auslenkung wird ein hysteretischer Sprung in der Partikelposition beobachtet, der von der komplexen Intensitätsverteilung über der fokalen Ebene des stark fokussierten Laserstrahls verursacht wird. Außerdem wird das gleichzeitige Fangen eines Goldnanopartikels und eines Janusparticels demonstriert, was erste praktische Anwendungsmöglichkeiten des Systems aufzeigt. Es wird gezeigt, dass dieser photonische "Fahrstuhl" auf der Mikrometerskala ein vielversprechendes Werkzeug für die Untersuchung thermischer Kräfte, für ferngesteuerte Detektion und für optische und thermische Manipulation auf der Mikroskala darstellt.

Im zweiten Teil dieser Arbeit wird eine optofluidische Methode vorgestellt, die es erlaubt, das vektorielle Nahfeld von Schwingungsströmungen in zwei Dimensionen auf der Mikroskala zu kartieren. Bei der Untersuchung dient ein lichtgetriebenes Mikropartikel als Quelle für die oszillierenden Strömungen, die dann mit einem in der Nähe gefangenen Silikapartikel detektiert werden. Mit Hilfe einer räumlichen und zeitlichen Fourier-Analyse der Bewegung des detektierenden Partikels wird eine vektorielle Karte der Strömungen um die Schwingungsquelle erstellt. Eine Verwendungsmöglichkeit dieser Methode ist die in-situ-Charakterisierung von Anordnungen zur schnellen Mischung von Flüssigkeiten auf der

Mikroskala. Des Weiteren ermöglicht die Analyse des vektoriellen Flussfeldes die Erkennung und Lokalisierung sich bewegender Schwingungsquellen, was sowohl für künstliche als auch biologische Mikroobjekte, wie etwa Zellen und Mikroorganismen, angewendet werden kann.

1 Introduction

The first speculations on the exchange of momentum between light and matter date back to 1619 [1]. The invention of the laser 55 years ago led to discovery of an ever-increasing number of applications that utilize optical force. An optical trap, known as *optical tweezers*, can trap objects as small as 5 nm [2, 3] and can be used to exert and to determine forces exceeding 100 pN [4–6] with resolutions as fine as 100 aN [7–10]. The ability of optical tweezers to exert and detect well-defined forces and remotely manipulate objects makes them a standard research tool in biology, chemistry, and physics [10–12]. Thirty years after the invention of optical tweezers their applications continue to grow in number. The goal of this dissertation is to use the well-defined properties of optical tweezers to study two microscale systems of increasing interest: The motion of a self-propelling particle (d= 1.3 µm) in optical tweezers, and the flow around a microscale oscillator.

Self-propelling structures at the nano- and microscale are of great interest for controlling processes in microfluidic chips, as well as aiding in therapeutics, diagnostics and performing in vivo tasks [13–15]. Motion at this scale presents challenges because viscous forces dominate the inertial forces. In order to swim in the low Reynolds number regime, some biological organisms exhibit nonreciprocal motion, which has been the inspiration for many artificial microswimmers [16–19]. However, one of the simplest forms of autonomous microswimmers are spherical Janus particles, which consist of two hemispheres with different physical or chemical properties [20]. Optically induced heating of plasmonic Janus particles provides a versatile means of actuation that can be switched on and off almost instantaneously. Upon illumination, heat generated on the metal side of a Janus particle induces a local thermal gradient resulting in particle motion in the direction opposite of the metal side in liquid media. At short times (< 0.2 s) this results in linear motion, whereas at longer times the random reorientations lead to enhanced diffusion [21].

As outlined previously, optical trapping has been shown to be an effective tool for controlling micro- and nanoscale particles [22]. Stable three dimensional optical trapping of individual microscale plasmonic Janus particles, however, has been challenging for most geometries. This is due to strong scattering forces acting on the particle as well as the efficient heat generation in the metal resulting in a large thermophoretic force and subsequent ejection from the trap. Merkt et al. [23] have reported 2-dimensional rotational motion around a trap as the result of competing optical forces on a Janus particle. The first study in this dissertation demonstrates the controlled trapping of a gold/silica Janus particle in a laser beam. A special particle geometry is chosen so that optical and thermal forces are balanced and 3-dimensional immobilization of the particle is achieved. Remarkably, the axial position of the nanoparticle is not fixed, but is found to depend on the power of the trapping laser. By adjusting the power, it is possible to move the particle up and down within the trap, effectively creating a microscale photonic elevator.

The control of microscale flow offers a unique opportunity to explore complex microscale systems. Flow at this scale has attracted renewed interest in the control of macromolecules, including DNA stretching [24, 25] and blood flow [26], as well as detection of microorganisms, such as bacteria cells [27]. The velocity fields of steady flows in microchannels and in microchambers have been measured with micron-scale resolution using trapped particles [28, 29]. Oscillatory flows, on the other hand, are of great importance for pumping and mixing different substances at the microscale [30, 31]. As flow devices become smaller turbulence stops playing a major role and mixing becomes increasingly difficult. Although controlled, oscillating flows are of great importance for the catalysis of chemical reactions and for future generations of fast speed detection sensors on the nano- and microscale [30], their detailed micron-scale mapping has not been demonstrated until now. The second study in this dissertation introduces an optofluidic method to quantitatively map two-dimensional oscillating flows with microscale resolution.

This thesis is organized in six Chapters. In Chapter 2, after this general introduction, the theoretical concepts necessary for understanding the experiments and their results are presented. The chapter focuses on the optical forces in a focused Gaussian beam, the concept of force measurement with optical tweezers, particle thermophoresis and self-thermophoresis with plasmonic Janus particles and the

concept of oscillatory flows. Chapter 3 lists all of the methods and materials used to prepare the samples for the measurements and to perform the actual experiments. It also describes in detail the optical setups constructed for the studies presented in chapters 4 and 5. Chapter 4 presents the study on Janus particles, composed of a silica sphere with a gold half shell, in a single beam optical trap. The second microscale study in this dissertation is presented in Chapter 5. It introduces an optofluidic method that allows the 2-dimensional vectorial near-field mapping of oscillatory flows with micron-scale resolution. The last and 6th Chapter summarizes the results and presents the conclusions of this work. It also gives an outlook of possible applications and future research.

2 Theoretical Foundations

This chapter guides the reader through the fundamental theoretical background necessary to understand the studies presented in this dissertation. It begins with an introduction to the concept of optical force. The first section follows optical forces from the suggestion of their existence through their theoretical description and the first experimental measurements. The section ends with an explanation of the limited importance and applicability of optical forces in the absence of a coherent light source. The second section of this chapter introduces the reader to the revolution of optical manipulation made possible by the invention of the laser. It considers in detail the simplest and most widely used optical force tool - the single beam optical trap, commonly known as optical tweezers. This section is essential for the studies presented in Chapter 4 and Chapter 5, since they employ optical trapping as the main tool. The physical origin of the force components involved in optical tweezers are presented with the help of two intuitive theoretical models. The section continues by introducing a practical model for total optical force calculations, the generalized Lorentz-Mie theory, applicable for spherical particles of any size. The following third section introduces thermophoretic motions. Optically induced thermophoresis is discussed in detail. This section is central for the studies in Chapter 4. The final section introduces the concept of oscillatory flow in a viscous fluid.

2.1 Optical Forces

In addition to illuminating and conveying information, light can also move physical objects. The first known speculations about light momentum date back to 1619 when Johannes Kepler attributed the specific shape of comets' tails to a repulsive force from the Sun [1]. He explained the repulsion as a result of the pressure exerted by the Sun's rays on the matter tail. More than a 100 years later, Leonhard Euler, who was inspired by the same effect, assigned pressing forces to a light beam and made an attempt to justify them theoretically [32]. The theoretical basis for the pressure of radiation was given by James Maxwell in 1873 [33], as a consequence of the electromagnetic theory of light, and by Adolfo Bartoli in 1876 as a consequence of the second law of thermodynamics [34]. Shortly afterwards, in 1899, the theory was experimentally confirmed by Pyotr Lebedev, who was the first to measure the pressure of light on a solid body [35]. Both theory and experiment showed that the ratio of momentum flux to energy flux is very small (less than 10 nN per watt in air). In the case of a parallel bundle of beams impinging steeply on a flat surface, the amount of *light pressure*, p, is given by the amount of *optical power*, P, (energy, **E** impinging per second), the *reflectivity* of a surface, $1+q$, and the *speed of light*, c as follows:

$$p = \left(1+q\right)\frac{P}{c}, \tag{2.1}$$

where q is in the range between 0 for a perfect absorber and 1 for a perfect reflector. Optical manipulation, on the other hand, requires forces such as gravity, friction and viscous drag to be overcome. These forces (except friction) scale with the size of the object to be manipulated. Thus, optical manipulation is naturally restricted to micrometer-sized or smaller objects. For maximal optical force, a light beam has to be focused to a spot with the size of the microparticle or smaller. Consequently, in order to lift a particle with a diameter smaller than 200 µm, one needs a light beam with power, $P = 1\,\mathrm{W}$ beam focused on an area of $10^{-8}\,\mathrm{m}^2$. This requires a black body with a very high temperature (over 6000 K) according to the brightness theorem [36]. Therefore, optical forces found no application before the 1970s. The lack of a powerful coherent optical source restricted the importance of optical forces to cases in which frictional forces are negligible, common in astronomy [37] and to

investigations in stellar atmospheres. In the former case, small accelerations could result in large changes in velocity over time, while in the latter case irradiances can reach extremely high values. The invention of the laser enabled greater irradiances to be achieved, allowing the limits to the irradiance achievable by focussing light from extended sources to be overcome. From the early 1970s on, the pioneering work of Arthur Ashkin and his team proved that optical forces are capable of manipulating small objects. They showed that microparticles can be propelled in a liquid [38] and levitated in air [39] by moderately focused laser beams. Furthermore, they demonstrated 3-dimensional, stable, all-optical trapping using a single tightly focused laser beam, later dubbed optical tweezers [40]. In this dissertation optical trap and optical tweezers mean the same and are used interchangeably. Optical manipulation developed into two branches: atom cooling and optical tweezers. The former led to Nobel Prizes in Physics in 1997 [41–43] and 2001 [44, 45].

2.2 Optical Tweezers

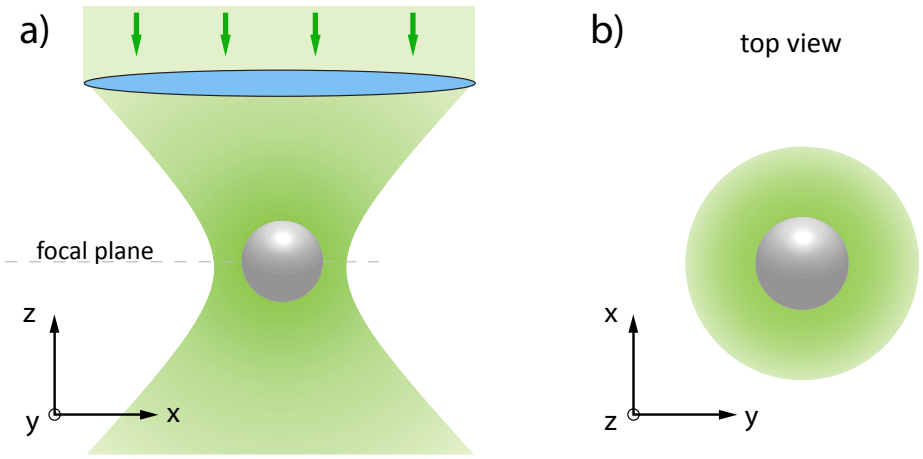

Figure 2.1 | Optical tweezers: a) Axial cross section of optical tweezers. A particle with refractive index higher than the surrounding medium is confined (trapped) in three dimensions close to the focal plane of a lens. b) Radial cross section of the focused beam at the trapping plane. The particle is trapped in the center of the focused beam.

Optical tweezers are the simplest and most widely employed optical trap [10, 11, 22, 46–48]. They are formed by focusing a laser beam with an objective lens of high

numerical aperture (typically NA ≥ 0.9). A particle brought into contact with the beam is subject to an optical force which draws it to the trapping point near the focus (see Figure 2.1). To understand the principle of the trap it is useful to split the total optical force on a particle in the focused beam into two contributions: (1) *scattering force*, acting in the direction of energy flux and (2) a *gradient force*, acting along the energy density gradient (see Figure 2.2). This decomposition is merely a convenient and intuitive way of discussing the overall optical force.

In optical tweezers, incident light impinges on the particle from one direction. It can either be scattered by the particle or be absorbed. Both processes result in a net momentum transfer to the particle from the incident photons. For symmetric scatterers, the resulting forces cancel in all but the forward direction, and an effective scattering cross section can be calculated for the object. The magnitude of the resulting scattering force is proportional to the laser power and depends on the particle material, size, shape, and the surrounding medium. The second component of the optical force, the gradient force, is responsible for the optical trapping of particles. The gradient force represents the attraction of a particle to the highest intensity region (the focal spot) in an electric field gradient (see Figure 2.2). If strong enough, it confines the particle near the focal spot, a phenomenon called *optical trapping*. Its magnitude is proportional to the gradient of the intensity within the beam, which in turn depends on the *numerical aperture* (NA) of the focusing lens and the laser power. Both force components have opposite directions below the focal plane (see Figure 2.2). Thus, the condition for 3-dimensional optical trapping is that the gradient force must have a larger magnitude than that of the scattering force and that of the force due to Brownian motion combined.

There are two theoretical models among others that allow for the decomposition of the optical force into gradient and scattering forces. They give a clear physical insight into the origin of the scattering and the the gradient component. Each of them applies in a different size regime, which is defined by the ratio of the laser wavelength and particle size. The first model, described in subsection 2.2.1, considers optical forces on an electric dipole in an intensity gradient, while the second model (see subsection 2.2.2) employs geometrical optics to determine optical forces as a result of the scattering and refraction of light by a particle. In the following a "spherical particle" will be referred to only as a "particle".

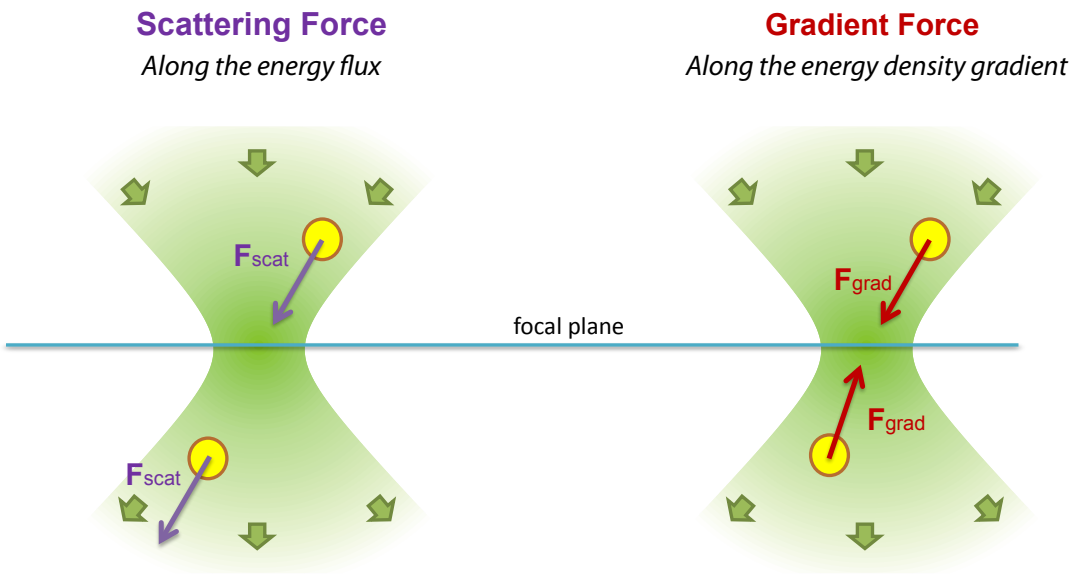

Figure 2.2 | Optical force components: a) Scattering force acting along the light energy flux, shown for particle above and below the focal plane of an objective lens. b) Gradient force acting along the energy density gradient, with different directions above and below the focal plane.

2.2.1 Rayleigh Regime - Dipole Force

If the particle is much smaller than the laser wavelength (radius $a \leq \lambda/20$) one can assume that the external electric field does not vary within the particle. In this electrostatic approximation, one can consider the particle as a combination of induced dipoles, oscillating in phase with the frequency equal to that of the incident field. Furthermore, a particle with homogeneous and isotropic polarizability can be considered as a single induced oscillating dipole with a dipole moment defined as a function of the polarizability α of the material it is made of:

$$\vec{p}_0 = \alpha \vec{E}_0. \tag{2.2}$$

The instantaneous optical force exerted on the particle is then simply the Lorentz force stemming from the interaction of the dipole with the electromagnetic field in its vicinity. However, since the field oscillates very fast harmonically with time (typically $f > 200 \times 10^{12}$ Hz) the motion of the particle cannot follow these changes.

As a result, only the time average of the electromagnetic force is observed. The time-averaged force is given by [46, 49]:

$$\langle F_m \rangle = \frac{1}{T}\int_{-T/2}^{T/2} \sum_{j=x,y,z} p_j \frac{\partial E_m}{\partial r_j}\, dt + \frac{1}{T}\int_{-T/2}^{T/2} \sum_{j,k=x,y,z} \epsilon_{mjk} \frac{\partial p_j}{\partial t} B_k\, dt \tag{2.3}$$

where T is the period of the time-harmonic field, p_j, E_j, B_j are the jth components of the time-harmonic dipole,

$$\vec{p}(\vec{r},t) = \mathrm{Re}\left[\vec{p}_0\, e^{-i\omega t}\right], \tag{2.4}$$

the electric field

$$\vec{E}(\vec{r},t) = \mathrm{Re}\left[\vec{E}_0\, e^{-i\omega t}\right] \tag{2.5}$$

and the magnetic field

$$\vec{B}(\vec{r},t) = \mathrm{Re}\left[\vec{B}_0\, e^{-i\omega t}\right] \tag{2.6}$$

respectively, with $\vec{E}_0$, $\vec{B}_0$ and $\vec{p}_0$ complex functions of position in space. Indices m, j, k run through the x, y, and z components of the vectors and ϵ_{mjk} denotes the Levi-Civita tensor. The time-averaged force in equation 2.3 consists of two terms. The first term corresponds to the force acting on the charges of the dipole placed in a spatially inhomogeneous electric field. The second one, corresponds to the Lorentz force acting on the moving dipole charges. Performing the integral, dropping the symbols for the time averaging and using the relations $\vec{B}_0 = \frac{c}{i\omega}\nabla \times \vec{E}_0$, $\vec{p}_0 = \alpha \vec{E}_0$ and $\dot{\vec{p}} = -i\omega\vec{p}_0$ yields:

$$\langle F_m \rangle \equiv F_m = \frac{1}{2}\mathrm{Re}\left[\sum_{j=x,y,z} p_j \frac{\partial E^*_{0j}}{\partial r_m}\right] = \frac{1}{2}\mathrm{Re}\left[\sum_{j=x,y,z} \alpha E_{0j} \frac{\partial E^*_{0j}}{\partial r_m}\right] \tag{2.7}$$

where * denotes the complex conjugate and p_j is the jth component of the induced dipole that satisfies $p_j = \alpha E_j$. $\alpha = \alpha' + i\alpha''$ is the complex, first-order, frequency

dependent polarizability which is a scalar for an isotropic material. The real part of the polarizability is associated with the property of particle material to be polarized by an external electric field. It relates directly to the force on a dipole in a spatially inhomogeneous electric field. This force is called the *gradient force*. The imaginary part of the polarizability, α'', is associated with two energy dissipative processes that occur within the particle. Both of these processes are the result of the oscillation of the dipole. The first one is the absorbtion of light by the particle, for example, in metal nanoparticles (see subsection 2.4.2.1). The second process, which is present even in the absence of absorption, consists of the elastic scattering of the incident light by the particle. It causes a phase shift between the dipole and the applied electric field. Both of these energy loss processes are in the origin of the *scattering force* which acts along the energy flux. The complex polarizability α can be expressed as [50]:

$$\alpha = \alpha' + i\alpha'' = \frac{a_0}{1 - \frac{2}{3}\frac{ik^3 a_0}{4\pi\varepsilon_0\varepsilon_1}} \simeq a_0 + i\frac{|a_0|^2 k^3}{6\pi\varepsilon_0\varepsilon_1} \tag{2.8}$$

where $\varepsilon_1 \equiv n_1^2$ is the relative permittivity of the surrounding medium, ε_0 is the permittivity of vacuum, $k = 2\pi n_1$ and $|\alpha_0|$ is the absolute value of α_0. α_0 is the the *static polarizability* which can be obtained from the Lorentz-Lorenz relation as follows:

$$\alpha_0 = 3\varepsilon_0 V \frac{\varepsilon_2 - \varepsilon 1}{\varepsilon_2 + 2\varepsilon_1} \tag{2.9}$$

For oscillating fields and absorbing particles, for example Au and Ag nanoparticles, ε_2 and consequently α_0 are complex. The real and the imaginary part of the complex polarizability α are then given by:

$$\alpha' \simeq \mathrm{Re}(\alpha_0),\ \alpha'' \simeq \mathrm{Im}(\alpha_0) + \frac{|\alpha_0|^2 k^3}{6\pi\varepsilon_0\varepsilon_1}. \tag{2.10}$$

If the complex electric field component of the light wave E_{0m} is expressed using a real amplitude E'_{0m} and a real phase ϕ' as $E'_{0m} = E_{0m}\, e^{i\phi'}$, then equation 2.7 for the total force on a particle in a laser trap can be rewritten as

$$F_m = \frac{1}{2}\sum_{j=x,y,z}\left[\alpha'\frac{1}{2}\frac{\partial\left(E'^2_{0j}\right)}{\partial r_m} + \alpha'' E'^2_{0j}\frac{\partial\phi'}{\partial r_m}\right]. \tag{2.11}$$

It follows from equation 2.11 that the optical force acting on a nanoparticle can be understood as a sum of the so-called *gradient* or *dipole force* and the scattering force [46]. The gradient force

$$F_m^{grad} = \frac{1}{4}\alpha' \sum_{j=x,y,z} \left[\frac{\partial \left(E_{0j}'^2 \right)}{\partial r_m} \right] \tag{2.12}$$

is caused by the gradient of the optical intensity $I \sim \sum_{j=x,y,z} E_{0j}'^2$. It is proportional to the real (dispersive) part of the particle polarizability. The scattering force, on the other hand, is proportional to the optical intensity (radiation pressure), the imaginary (dissipative) part of the particle polarizability, and also the gradient of the wave phase, and it is given as follows [46]

$$F_m^{scat} = \frac{1}{2}\alpha'' \sum_{j=x,y,z} \left[E_{0j}'^2 \frac{\partial \phi'}{\partial r_m} \right]. \tag{2.13}$$

These equations are not restricted to the spatial dependence of the incident field.

2.2.2 Ray Optics Regime - Refraction Force

If the particle is much larger than the wavelength of the laser radiation, a simple geometrical optics model can be used to explain and determine the scattering and gradient force contributions. Indeed, a particle (not totally reflective) located in a Gaussian beam changes the beam's propagation direction (refracts the beam) as shown in Figure 2.3. It pushes the beam in the radial direction. From momentum conservation, it follows that the beam pushes the particle in the opposite direction. Depending on which part of the beam is refracted, those forces have a different directions. Since the force originating from the refraction of the lower intensity region is consequently weaker, the particle will experience a net force towards the center of the beam. As soon as the particle reaches the beam axis both counteracting components cancel and there is no net-force on the particle. The difference in magnitude of the two components when the particle is displaced from the beam axis is proportional to the intensity gradient, which is defined by the focusing optics. The net refraction force acting along the gradient of the intensity is the *gradient force*. Similarly, the gradient force confines the particle axially at the focal plane as shown

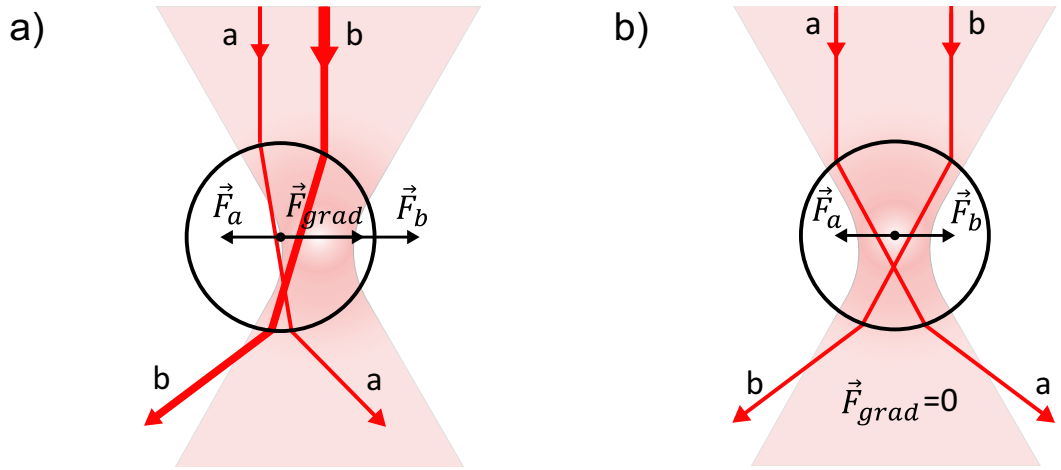

Figure 2.3 | Radial gradient force: a) Radial gradient force resulting from the difference of momentum exchange between ray **b** at the beam axis and ray **a** away from the beam axis. The net gradient force is different from zero if particle center is displaced from the beam axis. b) Particle center at the beam axis. All contributions to the gradient force cancel out due to symmetry reasons.

in Figure 2.4. The refractive index of the spherical particle has to be larger than that of the medium surrounding it. For particles with lower refractive index than the surrounding medium, the gradient force changes direction to the opposite, i.e the particle is repelled by the highest intensity spot. For a dielectric particle, the *scattering force* is defined as the force resulting from light reflection at the surface of the particle.

One can determine the gradient and the scattering force by defining the contribution of the components of each ray incident on the particle [51]. One can define the normal incidence components the rays as the ones that contribute to the scattering force. Consequently, the tangential components of the incident rays contribute to the gradient force. For beams of complex shape one can define the scattering and gradient forces of the beam as the vector sums of the scattering and gradient force contributions of the individual rays of the beam.

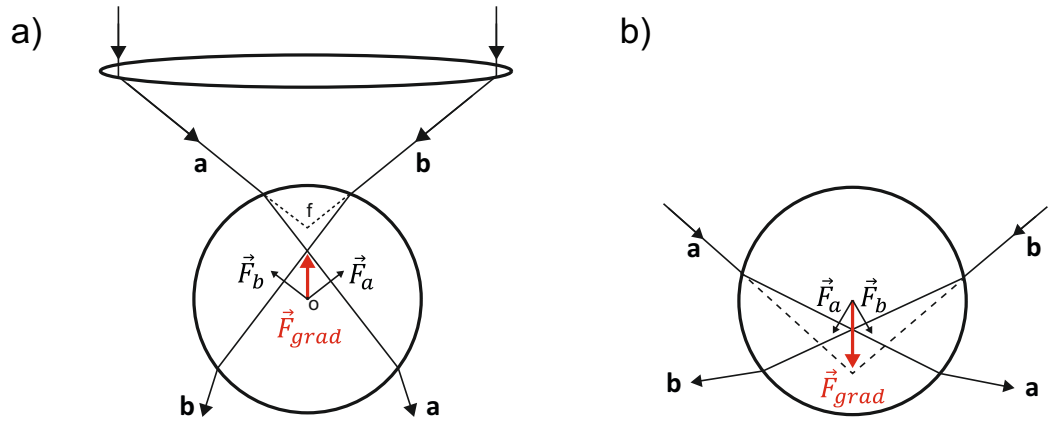

Figure 2.4 | Axial gradient force: a) Axial gradient force as a result of momentum exchange between two rays and a particle above the focal plane. b) Axial gradient force as a result of momentum exchange between two rays and a particle below the focal plane.

The scattering and the gradient force are then given by:

$$F_z = F_{scat} = \frac{n_1 P}{c}\left[1 + R cos2\theta - \frac{T^2\left[cos(2\theta - 2\varphi) + R cos2\theta\right]}{1 + R^2 + 2R cos2\varphi}\right] \tag{2.14}$$

and

$$F_y = F_{grad} = \frac{n_1 P}{c}\left[R sin2\theta - \frac{T^2\left[sin(2\theta - 2\varphi) + R sin2\theta\right]}{1 + R^2 + 2R cos2\varphi}\right]. \tag{2.15}$$

where θ and φ are the angles of incidence and refraction and the quantities R and T are the Fresnel reflection and transmission coefficients of the surface at θ.

2.2.3 Optical Force on a Sphere of Any Size

The models described above give clear physical insight of the components of the optical force in the Rayleigh and ray optics size regimes. However, the majority of objects that are useful or interesting to trap, including the particles used in the studies in Chapter 4 and Chapter 5, fall into the intermediate size range $(0.1 - 10\lambda)$, where both models are no longer applicable. There are several computational models that do not require restrictions on the size of the particle and can be used in this case. One such model is based on the generalized Lorenz-Mie theory (GLMT).

Generalized Lorenz-Mie theory

The optical forces on a particle in a light beam are the result of momentum transfer from the electromagnetic field to the particle. The particle alters the momentum of the beam through scattering. Thus, the calculation of the optical forces is essentially a problem of computational light scattering. Fortunately, an analytical solution to the problem of light scattering by homogeneous spherical particles of any size already exists. It was first published by a Danish physicist Ludvik Lorenz in 1890, however only in Danish. Later, Gustav Mie "rediscovered" it in 1908 [52], therefore it is generally known as Lorenz-Mie theory or Mie theory. The Lorenz-Mie theory assumes plane wave illumination which is very limiting and does not allow for force calculations involving focused laser beams. The generalization of the theory to allow a arbitrary shape of the incident beam is achieved in the form of generalized Lorenz-Mie theory [53–57]. However, GLMT, as well as the Lorenz-Mie theory apply only to spherical particles and spheroids.

The standard laser beam representations are solutions to the paraxial scalar wave equation. Consequently, the standard representations, are not radiation fields, but only approximations of radiation fields. The generalized Lorenz-Mie theory (GLMT), on the other hand requires representation of the fields as sums of vector spherical wavefunctions which are solutions of the vector Helmholtz equation. This can be done with the point matching approach reported in [58]. The incident field, U_{inc}, can then be written in terms of a discrete basis set of functions ψ_n^{inc}, where n is the mode index labelling the functions, each of which is a solution of the Helmholtz equation,

$$U_{inc} = \sum_{n}^{\infty} a_n \psi_n^{inc}, \tag{2.16}$$

where a_n are the expansion coefficients for the incident wave. The infinite sum must be truncated at some finite n_{max} for computational reasons. The finite sum places restrictions on the convergence behavior of useful basis sets. For a finite and compact scatterer, the most useful set of basis functions is given by vector spherical wavefunctions (VSWFs) [58–61]. The discrete nature of VSWFs, together with their well known convergence [62], allows for straightforward representation of the fields on a computer.

One can write an expansion similar to 2.16 for the scattered wave,

$$U_{scat} = \sum_{k}^{\infty} p_k \psi_k^{scat}, \tag{2.17}$$

where p_k are the expansion coefficients for the scattered wave. For scatterers (particles) with linear optical response, the relation between the incident and scattered fields is linear and can be written as a simple matrix equation,

$$p_k = \sum_{n}^{\infty} T_{kn} a_n, \tag{2.18}$$

or

$$\vec{\mathrm{P}} = \mathbf{T}\vec{\mathrm{A}}. \tag{2.19}$$

where **T** is the transition matrix (T-matrix), or system transfer matrix [59–61]. GLMT usually uses such a matrix description implicitly, as in Lorenz-Mie theory. Further, GLMT provides a method for calculating the T-matrix (the Mie coefficients), as well as methods for calculating the expansion (beam shape) coefficients of the beam. For a spherical scatterer the T-matrix is diagonal, since the VSWFs are orthogonal over a sphere, and there is no coupling between different modes. The T-matrix depends on the properties of the scatterer (composition, size, shape, orientation) and the wavelength of the incident beam. It is otherwise independent of the incident field intensity distribution as well as the position of the particle with respect to the beam. Thus, the T-matrix for any particular particle only needs to be calculated once. It can then be used for repeated calculations of optical force and torque, which result from differences between the incoming and outgoing fluxes of electromagnetic momentum and angular momentum. The required calculation of these fluxes can be done by integration of the Maxwell stress tensor, and its moment for the torque, over a surface surrounding the particle. The bulk of this integral can be determined analytically. An overview and detailed treatment of the theory can be found in the following references [56, 63–70]. The optical force calculations required in the following chapters were performed using a computer implementation (code in Matlab) of the theory. It is presented in details in references [69, 70] together with the accompanying manual (Manual Optical Tweezers Toolbox).

2.3 Force Measurements with Optical Tweezers

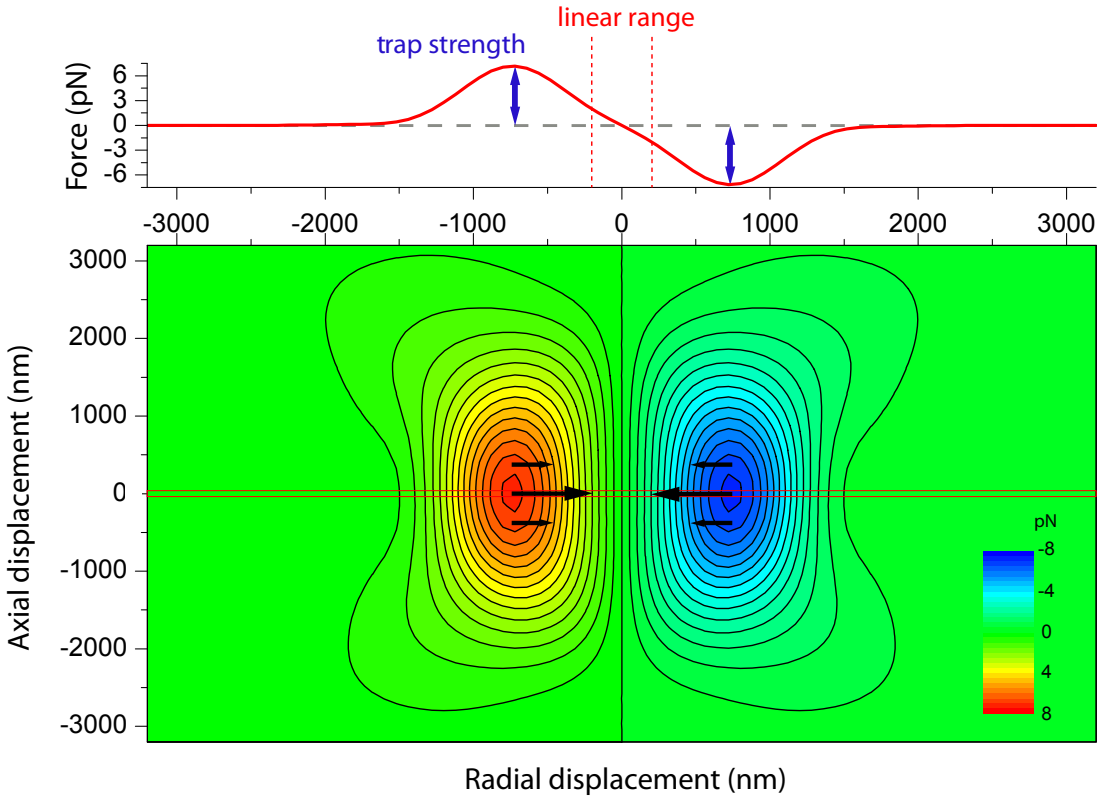

Figure 2.5 | Radial optical force: Axial cross section of radial optical forces in optical tweezers obtained by focusing a 10 mW beam of a 1064 nm laser through an microscope objective lens with NA = 1. The figure contains only the radial component of the optical force acting on a silica bead with diameter 1.3 µm. It is acting always toward the center of the beam at (0,0). The colors in the plot indicate the change of force direction passing the beam axis. The force at the focal plane is plotted versus the distance from the beam axis. The region of linear dependence, centered at the equilibrium point, is shown in black. The maximal radial restoring force for this power is shown in blue.

Since their invention, optical tweezers have found many applications in physics [71–77], biology [78–85], chemistry [86] and nanotechnology [87]. In some of these contexts, the tweezers are only used to grab and hold an object (particle, cell, bacteria, etc.). In other contexts, they are used to exert a prescribed force or to measure a force. Optical tweezers can be used to exert and measure forces exceeding 100 pN [4–6]. Considering motion only in the focal plane, when a trapped particle is displaced from

the beam axis it experiences a restoring optical force compensating for the external force which caused the displacement. For small displacements of $\approx 150\,\text{nm}$ (see Figure 2.5), the restoring gradient force is linearly proportional to the offset from the beam axis. The optical trap acts as a Hookean spring whose characteristic stiffness, k, is proportional to the light intensity gradient (proportional to the NA of the focusing lens and the laser power). The external force is then given by:

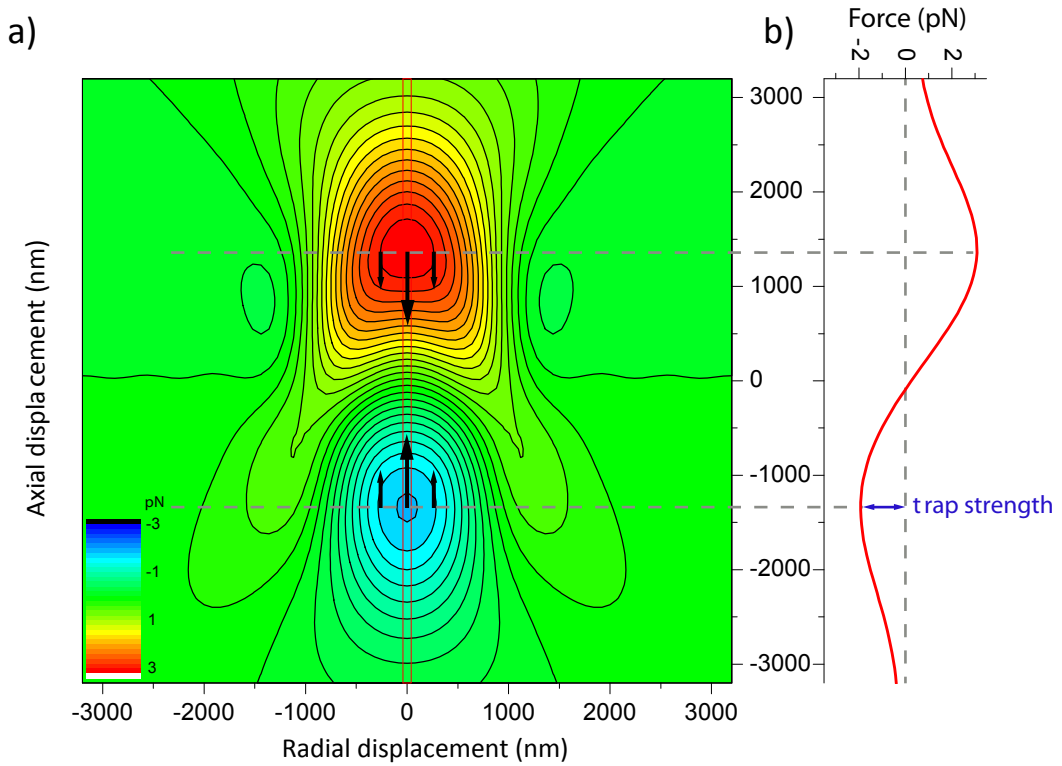

Figure 2.6 | Axial optical force: a) Axial cross section of axial optical force in optical tweezers obtained by focusing a 10 mW beam of a 1064 nm laser through an microscope objective lens with NA = 1. The figure contains only the axial component of the optical force acting on a silica bead with diameter 1.3 µm. It is always acting toward the center of the beam at $(0, 0)$. The colors in the plot indicate the change of force direction passing the focal plane. b) The force along the beam axis is plotted versus the distance from the focal plane. The smaller maximum of the axial restoring force for this power is shown in blue.

$$F_{grad} = -k \cdot |d| = -F_{ext} \tag{2.20}$$

Consequently, knowing the displacement, d, and the *trap stiffness*, k, one can determine the magnitude of the external force. Alternatively, the total force at a displacement d can be obtained using the theoretical model in subsection 2.2.3. The precision of the force determination is defined by the precision with which the position of the particle and the trap stiffness can be determined. Applying position detection in the back focal plane of the objective (back-focal-plane-interferometry) to determine k allows to calibrate tweezers with less than 1% error when the trapping force is in the pN range [8, 9]. The maximal restoring force (for fixed laser power) keeping the particle within the trap is called *trap strength*. The value of the trap strength depends on the direction of the external force acting on a trapped object. The trap is weakest along the beam axis in the direction of propagation ("downbeam"), where the scattering force acts to push the particle out of the trap (see Figure 2.6).

2.3.1 Trap Stiffness

Optical forces on a trapped particle using an ideal optical system can be predicted theoretically. However, such systems do not exist, and the effect of the experimental circumstances has to be considered when the absolute value of the force has to be determined. Thus, calibration is necessary. The power spectrum analysis of the position of a trapped bead to calibrate optical tweezers is usually considered to be the most reliable option [88]. This method provides the trap stiffness, k, via analysis of the experimentally observed Brownian motion of a trapped particle.

A particle freely diffusing in a viscous fluid performs a random walk (Brownian motion) due to the continuous bombardment by the neighboring solvent molecules. The particle diffusional motion can be predicted using Einstein's expression for the free diffusion coefficient D [89]:

$$D = \frac{k_B T}{\gamma} \tag{2.21}$$

if the hydrodynamic drag coefficient, γ, for steady motion is known. According to equation 2.21, random diffusion is proportional to the absolute temperature T. In terms of D, each coordinate $x(t)$ of a diffusing particle is described by

$$\mathrm{Var}[x] = \overline{x^2} - \overline{x}^2 = 2Dt \tag{2.22}$$

and for 3-dimensional diffusion, the squared distance from the origin grows as $r(t)^2 = 6Dt$. Equation 2.22 states that the random excursions of the particle from its starting point grow larger and larger as time goes by.

A particle in an optical trap, on the other hand, "feels" not only random forces from solvent molecules, but also a restoring optical force confining it within the trap and preventing its long-range diffusion. Consequently, the particle wiggles in the trap with an average amplitude that depends on the trap stiffness and the temperature. Near the center of the trap, the restoring optical force is proportional to the displacement, as for a harmonic spring (as shown in Figure 2.3). For the case of a harmonic potential or linear restoring force, the position $x(t)$ of a particle trapped with a spring constant k varies according to a Gaussian distribution, with a displacement variance [89]:

$$\mathrm{Var}[x]_{trap} = \overline{x^2} - \overline{x}^2 = \frac{k_B T}{k} \tag{2.23}$$

According to equation (2.23), a trapped particle will move randomly with a root mean square displacement of approximately 20 nm for biological temperatures (up to 50°C) and typical trap stiffness values of up to 1×10^{-2}pN/nm for optical tweezers. This well-defined characteristic of Brownian motion can be exploited to calibrate the viscoelastic parameters of optical tweezers such as the spring constant. The position $x(t)$ of the trapped particle can be approximated by a Langevin equation with a random force $F(t)$:

$$\gamma \frac{dx}{dt} + kx = F(t) \tag{2.24}$$

Equation 2.24 states a balance of forces, in which the drag force and optical restoring force are balanced by a random force $F(t)$ from bombardment of the solvent molecules. This is a simplifying approximation in which the random force, $F(t)$ is assumed to be an ideal white noise force and the friction coefficient γ is assumed to be frequency independent. However, it describes the Brownian motion of a micrometer-sized particle in water very well. If $X(f)$ is the Fourier transform of $x(t)$,

$$x(t) = \int_{-\infty}^{\infty} X(f) e^{-2\pi f i t} df, \tag{2.25}$$

then the Fourier transformation of both sides of Equation (2.24) gives

$$2\pi\gamma(f_c - if)X(f) = F(f), \tag{2.26}$$

where f_c is the characteristic frequency (also called corner frequency) of the trap, which is defined as $f_c \equiv k/2\pi\gamma$. Both sides of Equation (2.26) are complex expressions. By taking their squared modulus one obtains

$$4\pi^2\gamma^2\left(f_c^2 + f^2\right)|X(f)|^2 = |F(f)|^2, \tag{2.27}$$

where $|X(f)|^2 = S_x(f)$ and $|F(f)|^2 = S_F(f)$ are the *power spectral densities* of $x(t)$ and the random force $F(t)$, respectively. $F(t)$ has an average value of 0, and its power spectrum ($S_F(f)$ plotted against f) is a constant (as for an ideal white noise force):

$$\overline{F(t)} = 0 \text{ and } S_F(f) = |F(f)|^2 = 4\gamma k_B T. \tag{2.28}$$

In contrast, the power spectrum of the motion of the particle in an optical trap has a Lorentzian shape [90]. Substituting $|F(f)|^2$, Equation (2.27) can be written for $S_x(f)$ as follows:

$$S_x(f) = \frac{k_B T}{\gamma\pi^2(f_c^2 + f^2)}. \tag{2.29}$$

Equation (2.29) shows that a Lorentzian (power spectral density) function describes how fluctuations are distributed over different frequencies f. The corner frequency f_c divides the Brownian motion into two regimes. For frequencies $f << f_c$, the power spectrum is approximately constant, $S_s(f) \approx S_0 = 4\gamma k_B T/k^2$, which refers to the confinement of the particle. At higher frequencies, $f >> f_c$, $S_x(f)$ falls off like $1/f^2$, which is characteristic of free diffusion. Over short times the particle does not feel the confinement of the trap. The power spectral density in (2.29) depends on two parameters, γ and k, which can be obtained by fitting equation (2.29) to the data [7, 88, 91, 92].

$$k = \frac{2k_B T}{\pi S_0 f_c} \tag{2.30}$$

$$\gamma = \frac{k_B T}{\pi^2 S_0 f_c^2} \tag{2.31}$$

If γ is know in advance (as could be for a sphere), then k can be obtained directly from $k = 2\pi\gamma f_c$ which follows from equations (2.30) and (2.31).

The Effect of Laser Polarization

The trap stiffness along the polarization direction of the laser is typically about 10% larger than that in the orthogonal direction [93]. Thus, the stiffness of a linearly polarized laser trap needs to be determined for both directions. This is usually done by analysing the Brownian motion components along and orthogonal to the laser polarization separately.

2.4 Self-thermophoresis with Plasmonic Janus Particles

2.4.1 Thermophoresis

The relative motion of the components of a complex fluid when a temperature gradient is applied is called *thermophoresis*. This motion leads to relaxation towards a steady state non-uniform concentration [94]. The effect was first discovered in liquids by Ludwig [95] who noticed that concentrated salt solutions easily crystallize around a cooled body. Later, the effect was quantified for many electrolyte solutions by Soret [96]. Therefore, the separation of the components in liquid mixtures and solutions in thermal gradient is known as *thermal diffusion*, *Soret effect* or *Ludwig-Soret effect* [97]. Thermophoresis is also observed in aerosol mixtures. An aerosol is a colloidal suspension of fine solid particles or liquid droplets in air or in another gas [98]. In the presence of a hot body, the molecules of the nearest gas medium are heated and create a fast flow away from the hot surface, down the temperature gradient. As a result, the heavier and slower-moving solid particles in the gas are

thus pushed away and a thin particle-free layer (less than 1 mm) is formed at the hot surface. The effect can be observed by the naked eye, provided good illumination, with tobacco smoke and a hot rod of a heater. The first observation of this effect was reported by Tyndall [99].

The thermal gradient that causes thermophoresis acts as a generalized force on suspended particles, molecules, droplets or micelles, and drives them to the cold or to the warm. The drift velocity $\vec{v}$ is given by:

$$\vec{v} = -D_{\mathrm{T}} \nabla T, \tag{2.32}$$

where D_{T} is usually called *thermal diffusion coefficient* despite of the fact that it does not have the dimension of diffusion coefficient. That is why sometimes the term *thermophoretic mobility* is used instead [100–102]. The drift velocity depends on the surface properties of the solute and its interactions with the solvent [103]. Experimental studies on thermophoresis in macromolecular solutions and colloidal suspensions have revealed a rich behavior and dependences of $\vec{v}$ on salinity and solute concentration [104–106], surface coating [107] and molecular weight [102, 108, 109]. Consequently, in order to determine the sign and the magnitude of the thermophoteric mobility one has to consider each of the system-specific mechanisms causing the particle motion. For low contraction of particles suspended in simple liquids, however, a simple expression can be used to determine the drift velocity. In simple liquids particle thermophoresis is caused by the inhomogeneity brought on by the thermal gradient in the thin layer that physically constitutes the interface between particle and solvent [101, 102]. More precisely, the thermoosmotic flow along a solid-liquid interface is mainly due to the solvent density gradient. Simple liquids expand upon heating (except for water below 5°C). Consequently, the lower density at the hot side of the particle causes a solvent flow along its surface to higher T. As a result of this flow the particle moves in the opposite direction, towards its cold surface. Particle's drift velocity is given by

$$\vec{v} = -\frac{2\beta H}{9\pi\eta d_0} \nabla T, \tag{2.33}$$

where η is the solvent viscosity, β is the solvent thermal expansivity, and H is the Hamaker constant [110]. This motion leads to the steady-state concentration gradient ∇c. For low particle concentrations $\vec{\nabla} c$ is given by

$$\nabla c = -c S_T \nabla T, \tag{2.34}$$

where

$$S_T = D_T / D \tag{2.35}$$

is called the *Soret coefficient*. The sign of the Soret coefficient, S_T, determined by the sign of the thermophoretic mobility D_T, shows whether the particles move towards the cold or the hot side (along or against ∇T). For $S_T > 0$ and for $S_T < 0$ the particles move to the cold and the hot side respectively. A similar migration effect is observed when an external driving force, such as gravity or an electric field, is applied to the suspension. In those cases the migration can be directly related to the external field. In contrast, in the case of particle thermophoresis no real external field is actually present and no such simple relation is possible. A common approach to find the "thermal force" f_t for systems not too far from equilibrium is trying to model an "effective force" $\vec{f}$ on the particles, leading to the same steady-state condition induced by the thermal gradient [103, 110–113]. The Soret coefficient can be determined by the relation $S_T \nabla T = -\beta \vec{f}$, obtained by the stationary solution of the Smoluchowski equation (2.36) for the time evolution of the probability $P(\vec{r}, t)$ to find the colloid at position $\vec{r}$ [114].

$$\frac{\partial P}{\partial t} = \nabla \cdot \left[D(\nabla P - \beta \vec{f} P) \right], \beta = 1/k_B T \tag{2.36}$$

The models for determination of $\vec{f}$, applicable in the specific case of thermophoresis of solid colloidal particles in simple liqiuds, are introduced in the following references [103, 113].

2.4.2 Plasmonic Janus Particles

A plasmonic Janus particle (JP) is a particle which has two or more surfaces with different physical or chemical properties. One of the surfaces is comprised of a plasmonic material. From here on, a JP is simply a silica sphere, half-coated with a thin percolated gold layer (not a complete film) as shown in Figure 2.8. One can naturally assume that the optical properties of such particle are a combination of the properties of the materials of which it is comprised. However, the compositional structure and the effect of each material on the other material's properties is often what defines the optical response of the new material. Noble metals (Au, Ag) do not form complete ultrathin (ca. $1-10\,\mathrm{nm}$) films when evaporated on silica [115, 116]. Instead, island-type films are formed (see Figure 2.8). They exhibit transmission spectra showing an absorption band attributed to localized surface plasmon excitation, similar to systems consisting of dispersed metal nanoparticles with a certain size distribution [117–129].

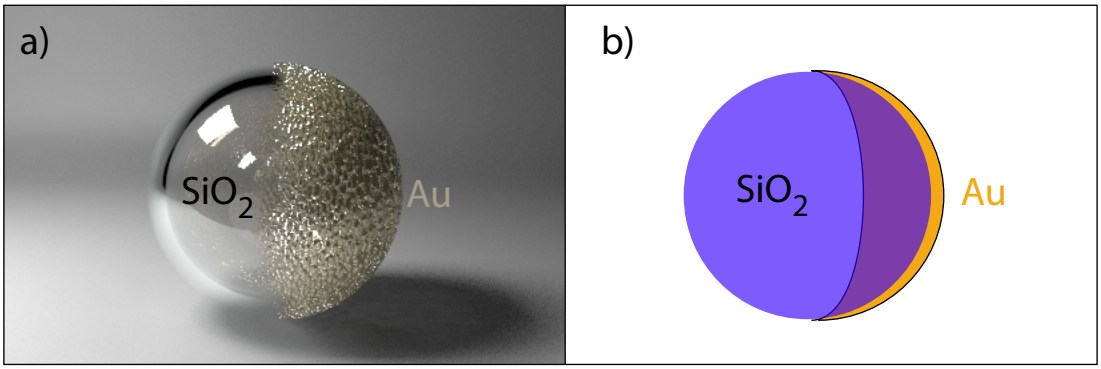

Figure 2.7 | Plasmonic Janus particle. The particle consists of a silica sphere and a thin layer of noble metal (typically gold). a) The metal layer covers only half of the sphere's surface. b) Schematic of a plasmonic Janus particle produced via evaporation of gold on a dielectric sphere (see subsection 3.2.1). The thickness of the evaporated gold decreases from the center of the coated half toward its ends.

2.4.2.1 Absorption at the Island Film

Ultrathin gold films consist of nanoislands. The conduction band electrons in metal nanoparticles can be excited by optical fields and oscillate coherently, turning the

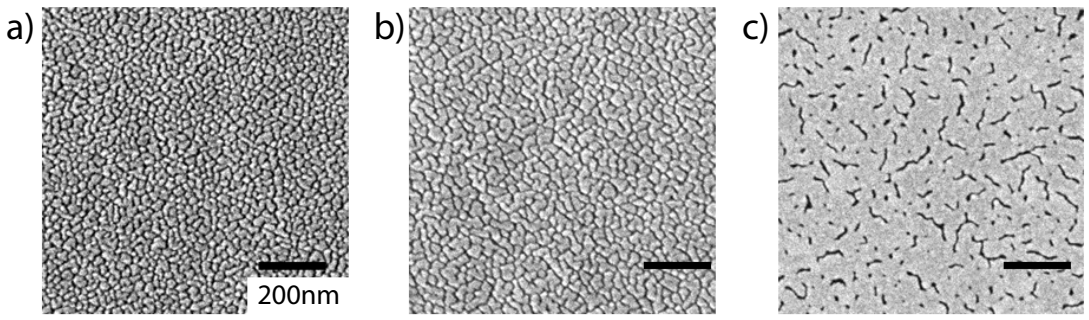

Figure 2.8 | Percolated gold films on glass substrates: a) with thickness 5nm b) with thickness 7.6 nm c) with thickness 10.2 nm.

particle into an electromagnetically driven oscillator. Indeed, the displacement of the negative charges due to an external electric field gives rise to polarization charges at the particle surface and hence to a linear restoring force which determines the eigenfrequency of the system. The resonance occurring at the eigenfrequency of the particle oscillator is called *localized surface plasmon resonance* (LSPR) (Figure 2.9), *particle plasmon* or just *plasmon*. The associated large optical polarization at the resonance frequency results in strong light absorption and light scattering. The oscillator's eigenfrequency and strength depend on the particle material, shape, size and on the surrounding dielectric medium [130].

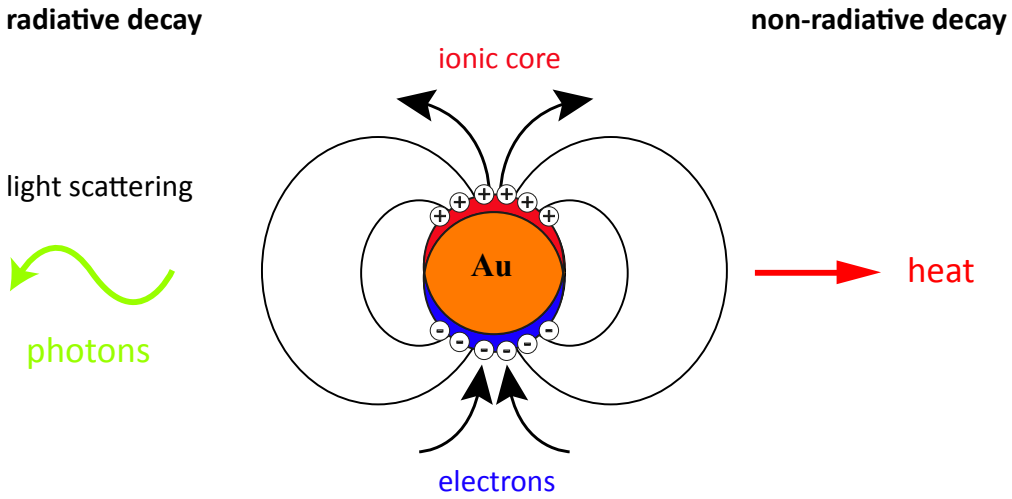

Figure 2.9 | Localized surface plasmon resonance: Schematic representation of the plasmon resonance in a single gold nanoparticle excited upon illumination. The non-radiative decay of the surface plasmon results in efficient conversion of electromagnetic energy into heat.

There are two main particle plasmon decay mechanisms. The first is the decay of the particle into photons (radiative decay). By the oscillation of the conduction band electrons in the nanoparticle oscillator, electric charges are accelerated. This causes an emission of electromagnetic wave with the same frequency as the incident (excitation) light, the incident wave is thus scattered. In the second decay mechanism the plasmon decays by creating electron-hole pairs. This nonradiative decay leads to absorbtion of the incident light, which is converted efficiently into heat. The electron-hole pairs are created mainly by electron-electron scattering [131]. For particles smaller than 10 nm there is an additional electron-surface scattering contribution [132]. As a result of this scattering, part of the electrons are excited above the Fermi-level and are no longer in thermal equilibrium with the remaining cold electron sea. The relaxation of these incoherently excited electrons is achieved through two processes, taking place at different time scales. The first and the much faster process consists of elastic scattering of the excited electrons among each other. It happens on a time scale of under 1 ps [133, 134] and produces a hot electron sea with the electrons reaching thermal equilibrium. The second process is achieved by scattering of the electrons with phonons. The high temperature difference between the hot electron sea, which can reach several thousands of degrees Celsius, and the cold ionic core is leveled out through electron-photon interactions in the next 10 ps [135–137]. After the thermal equilibrium within the particle is then reached, it transfers the heat to the surrounding medium in less than 1 ns (depending on its size and the properties of the surrounding medium) [138].

2.4.3 Optically Induced Particle Self-thermophoresis

2.4.3.1 Self-induced Temperature Gradients

Plasmonic Janus particles are one example of microparticles capable of generating temperature gradients along their diameter. This is due to their physical geometry which results in an anisotropic absorption. Upon illumination, light is absorbed at the semi-sphere covered with gold which generates heat that is consequently transferred to the surrounding medium. In contrast, the temperature of the other

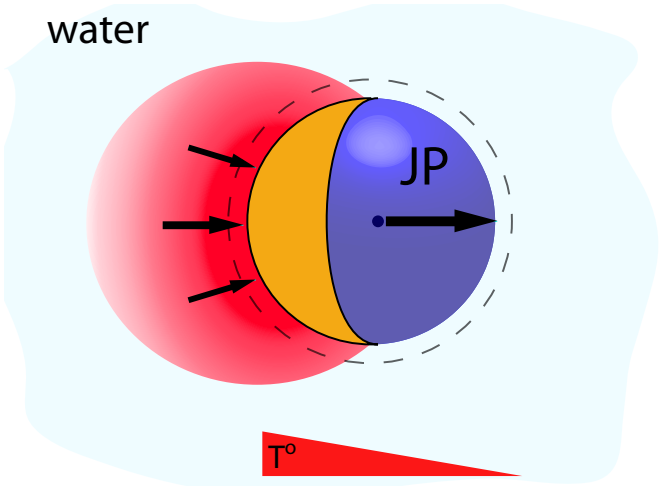

Figure 2.10 | Self-propulsion of a plasmonic Janus particle: Upon illumination, the particle generates a temperature gradient around itself. The difference of temperature in the thin water layer (dashed line) causes directional motion toward the cold side of the particle.

half of the sphere remains nearly unchanged. This anisotropic heat generation places the particle in a self-induced temperature gradient.

2.4.3.2 Self-thermophoresis

Figure 2.10 shows the distribution of heat around a resonantly illuminated particle. In the thin water layer around the Janus particle the temperature distribution does not differ from that of the usual particle thermophoresis in liquids (see subsection 2.4.1). Similarly, the average kinetic energy of the molecules bombarding the gold side is larger than that at the opposite side. As a result, the particle is subject to a thermophoretic force, which is proportional to the temperature gradient and drives it in the direction of its cold side. While the theoretical description is very much the same as for regular particle thermophoresis in liquids, the experimental verification of the Janus particle self-propulsion is slightly more complicated. The complexity comes from the fact that Janus particles are not symmetric particles. The orientation of their absorbing part defines the direction of the temperature gradient around the particle, and thus the direction of the thermophoretic force on the particle. Consequently, if the particle orientation is not fixed by some means it will not move in a straight line. Instead, increased particle diffusion caused by the active motion of

the particle will be observed. Such an increase of the diffusion, proportional to the laser power, was observed by Jiang et al. [21], who placed a plasmonic Janus particle in a defocused laser beam (see Figure 2.11).

The first, to the best of our knowledge, directed, optically induced motion of plasmonic Janus particles is demonstrated in Chapter 4.

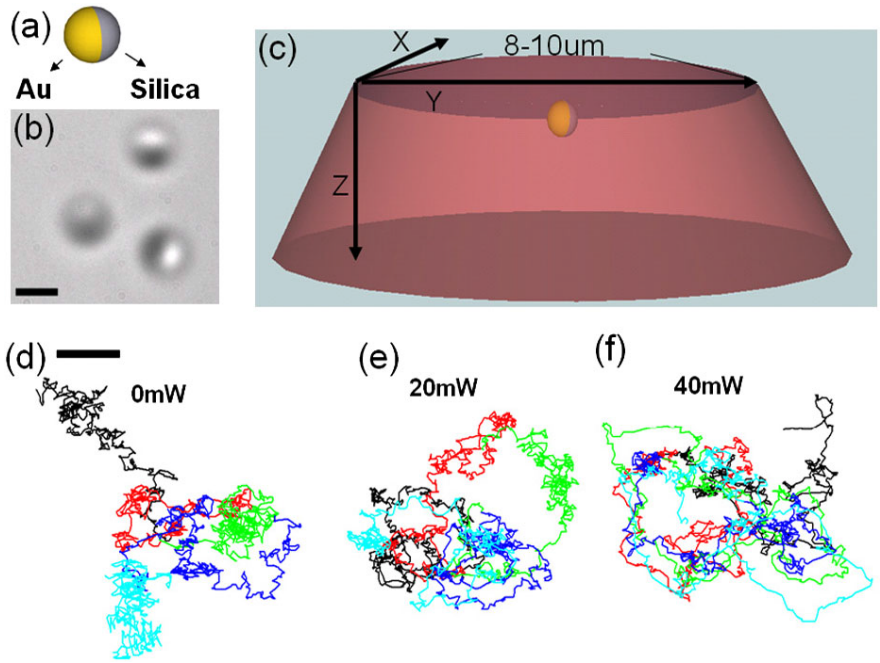

Figure 2.11 | Figure and caption taken from reference [21]. *(a),(b) Janus particle and its bright field image under microscope. The dark sides of the particles shown in (b) are the Au coatings (scale bar:* $1\,\mu m$*). (c) Schematic drawing of a Janus particle placed in a thin chamber (thickness:* $20\,\mu m$*). The laser, red (gray) cone, is fed in the Z direction from the bottom and the particles are visualized in the XY plane. (d) to (f) The trajectories of a Janus particle in the XY plane within* 10 *seconds. Each color corresponds to an interval of* 2 *seconds. (d) Without laser irradiation. (e)* $20\,mW$*, and (f)* $4\,mW$*. Bar:* $1\,\mu m$*.*

2.5 Oscillatory Flows

2.5.1 Acoustics and Hydrodynamics

When a solid body immersed in a viscous fluid oscillates, it generates a flow with characteristic properties. Depending on the compressibility of the fluid, one distinguishes between two categories: 1) oscillatory fluid motion in an incompressible fluid and 2) sound, which is oscillatory motion with small amplitude in a compressible fluid. Both types of oscillation obey the hydrodynamic equations, that is the Navier-Stokes equations. Moreover, acoustic oscillations are just a special case of the Navier-Stokes equations for a compressible fluid and a small amplitude of the source causing them. In this sense there is no fundamental difference between these fields. Indeed, a oscillation in the velocity of a fluid creates an acoustic pressure oscillation, and vice versa, analogous to the electric and magnetic fields in an electromagnetic wave. Thus, it is not possible to disentangle them if they are created by the same source. However, if the wavelength of sound is much larger than the system (the region of investigation), the compressibility of water becomes negligible. Consequently, in that case there will be no sound wave generation. The pressure and velocities around an oscillating source are then fully captured by the Navier-Stokes equation for an incompressible fluid.

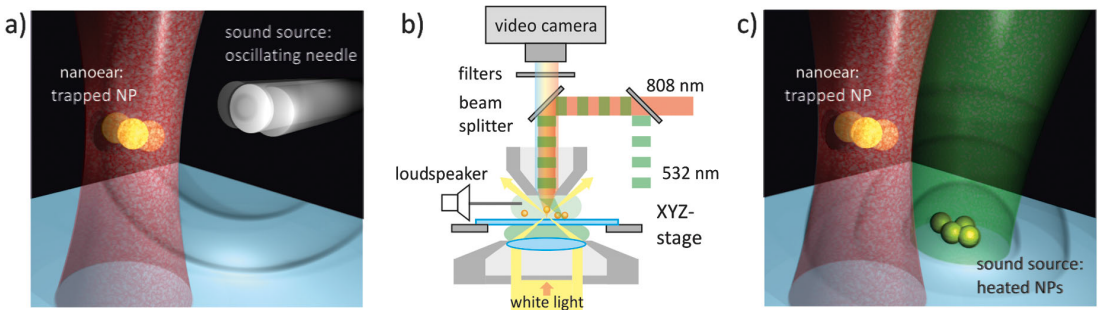

Figure 2.12 | Setup for acoustic detection at the microscale. Figure and caption taken from [139]. *(a) Schematic of the listening to a macroscopic sound source with a nanoear - an optically trapped gold nanoparticle. (b) Sketch of the experimental setup used for the listening experiment, which includes simultaneous three-dimensional optical trapping, optothermal and mechanical sound generation, and imaging of trapped gold nanoparticles. (c) Schematic of the listening to optothermally generated sound.*

2.5.2 Microscale Detection of Acoustic Waves and Oscillatory Flows

The behaviour of a viscous fluid at the microscale can be different from that at macroscale. This is because at the microscale factors such as surface tension, energy dissipation, and fluidic resistance become more pronounced and can even dominate the system. Thus, the precise modeling of sound and oscillatory flows at that scale can be a challenging task even if the geometry of the system and the source of the oscillations are well defined. For an unknown source, the velocity of the fluid can only be determined experimentally. Optical tweezers provide the base of a technique which allows for detection and quantification of oscillatory fluid motion with unprecedented sensitivity and spacial resolution [140]. In the study in reference [139] a 60 nm gold nanoparticle trapped in water served as an acoustic detector that could pick up sounds as low as −60 decibels. In the presence of an acoustic source in the solution, the particle was driven to oscillate with the same frequency as the source and an amplitude proportional to the velocity of the fluid around the particle. The sound source consisted of plasmonic nanoparticle aggregate which was heated periodically. As a result of the modulated heating, sound was generated via photoacoustic effect, 11 µm away from the detector particle. Figure 2.13a shows the position time series of the trapped particle. The acoustic contribution to the particle motion is hidden in its Brownian motion. In contrast, the Fast Fourier Transformation (FFT) of particle motion shows a peak at the frequency of the previously introduced sound source (see Figure 2.13b). The FFT amplitude at the source frequency is directly proportional to the peak speed of the oscillating fluid, which in turn is proportional to the acoustic power of the source.

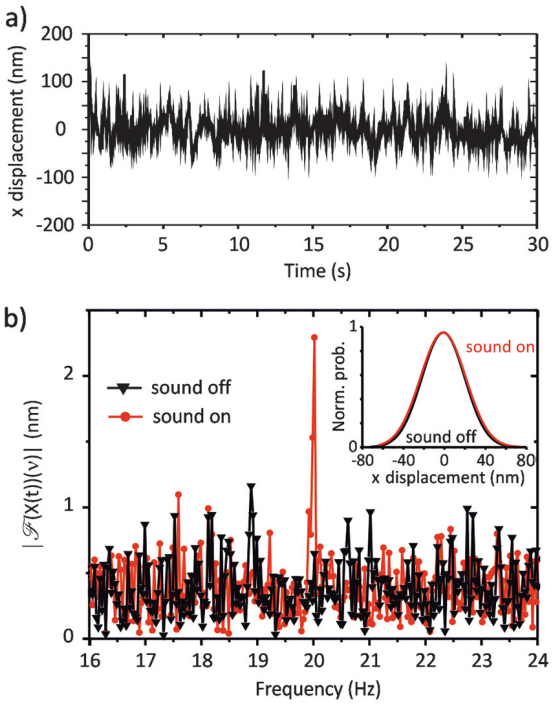

Figure 2.13 | Acoustic detection at the microscale. Figure and caption taken from [139]. *(a) Trajectory of the x displacement of a tracked trapped particle. The x coordinate in the analysis is chosen to be along a line connecting the sound source and the trapped nanoparticle. (b) Fourier transformation of the trajectory of a particle with sound switched off (black) and on (red). The inset shows the respective probability distributions of the particle displacement.*

3 Methods and Materials

This chapter lists all of the methods and materials used to prepare the samples for measurements and to perform the actual experiments. It furthermore describes in detail the optical setups constructed for the studies presented in the following chapters. The chapter begins with an introduction to dark-field microscopy, the basis illumination for the majority of the conducted experiments (section 3.1.1). The experiments can be categorized into two groups. The first group focuses on the demonstration of optothermal trapping of plasmonic Janus particles. Moreover, these experiments reveal the dependence of the axial trapping position as a function of the laser power, as presented in Chapter 4. The corresponding experimental setup is described in section 3.1.2. The second group of experiments is focused on demonstrating an all-optical method for two-dimensional, microscale mapping of oscillatory flows (Chapter 5). The corresponding experimental setup as well as the setup for allowing for the calibration of the detector trap are presented in section 3.1.3. The construction of the employed microfluidic source and the detector are discussed in detail as well as their principle of operation.

3.1 Experimental Setups

3.1.1 Dark-field Microscope

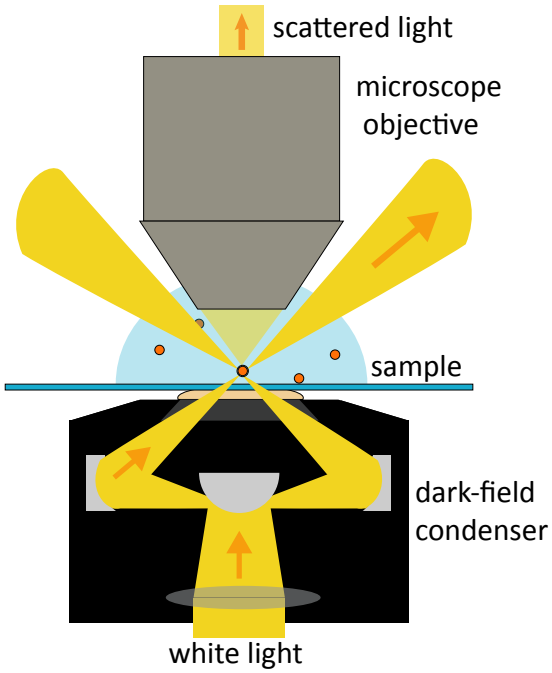

Figure 3.1 | Dark-field Microscope. The sample is illuminated through a Zeiss dark-field condenser only at angles in the range defined by its numerical aperture NA = 1.2 – 1.4. In the absence of scatterers (particles) in the sample, no light from the condenser is collected by the microscope objective (NA= 1.0). In a non-empty sample, particles scatter light in all directions. Some of it is collected by the objective and used to form an image of the sample. As a result the particles appear as bright spots on a dark background. The technique allows for imaging and spectroscopy of plasmonic particles as small as 20 nm. The sample is a drop of particle solution placed on a glass coverslip substrate. The optical contact between the dark-field condenser and the substrate is made by immersion oil.

Optical manipulation and analysis in the micro- and nano-scale requires a high contrast (signal-to-noise ratio) imaging system. This prerequisite, crucial for the studies in the following chapters, is provided by an upright dark-field microscope (Zeiss, Axio Scope.A1). Figure 3.1 shows its basic working principle. White light from a 100 W halogen lamp is sent to a high NA, oil immersion, dark-field condenser (Zeiss, Ultra condenser, NA =1.2-1.4). The condenser provides wide angle illumination of the sample in an angle range defined by its NAs. All other incident

angles including direct transmission are blocked. The contact between the condenser and a glass coverslip, of thickness 0.17 µm, is made by an oil drop with a refractive index n =1.518. A droplet of particles suspended in water is placed on the top of the coverslip. A typical volume of the droplet is between 50 and 100 µl. When scatterers (particles) are not present, the sample appears as a dark area because no light from the lamp is collected by the water dipping objective when it has a lower NA (NA = 1) than the condenser (see Figure 3.1). In the presence of scatterers in the sample, light from the condenser is scattered in all directions. Part of the scattered light is then collected by the objective lens and forms an image of the specimen after passing through the tube lens. The image is formed at the plane of the fixed diaphragm opening in the eyepiece (intermediate image plane) and/or onto a CCD chip of a digital camera. The only source of light in the sample image are the scatterers. They appear as bright spots on a black (dark) background, therefore giving the name of the illumination technique. Dark-field microscopy allows for the imaging and spectroscopy of solutions of small plasmonic nanoparticles (diameters of 20 nm and more) and percolated plasmonic nano-films (thickness of 5 nm or more), which is not possible with other light microscopy setups. It makes use of the fact that their scattering cross section is several times bigger than their actual size. Moreover, due to the high image contrast, optically trapped silica micro-spheres can be tracked with nanometer precision even with acquisition times as short as 1/1000 s.

Conditions for Dark-field Microscopy:
1. The numerical aperture of the dark-field condenser must be higher than the one of the objective lens. Otherwise light is collected directly from the condenser.
2. The focal spot of a microscope objective must be aligned with that of the condenser in the x,y and z dimensions.

3.1.2 Optical Setup 1

The experimental arrangement central for the experiments in Chapter 4 is shown in Figure 3.2. In addition to the dark-field microscope described above, it is equipped with optical tweezers which are described in detail in section 2.2. The trap is created by focusing the beam of a 1064 nm CW laser Rumba (Cobolt). The laser beam is

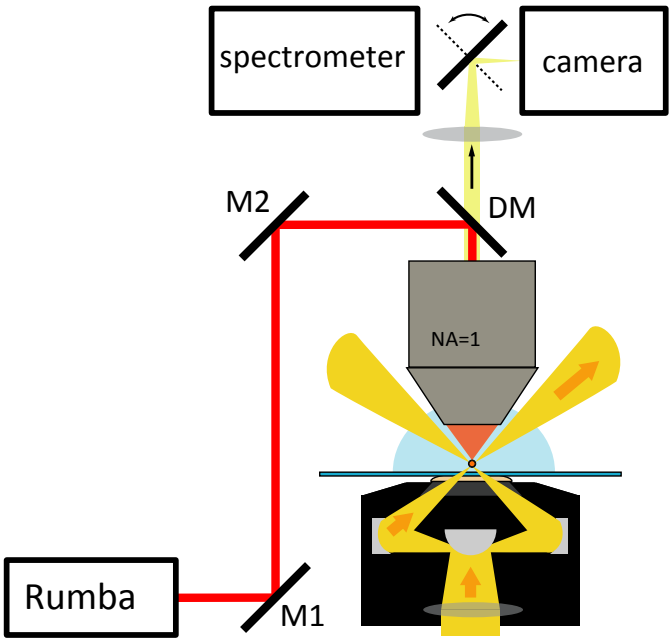

Figure 3.2 | Schematic of the experimental setup used for the trapping and elevation of plasmonic Janus particles presented in Chapter 4. The setup combines a dark-field microscope with 1064 nm optical tweezers, spectrometer and camera. It allows for simultaneous trapping, imaging and spectroscopy of particles.

first expanded 4 times by a beam expander (Edmund Optics) and then coupled to the microscope via two mirrors. Afterwards, it is focused through a microscope objective (Zeiss, Achroplan 100x/1.0 W Ph3) forming a 3-dimensional optical trap in the sample. The trap is brought to the center of the field of view of the objective via the coupling mirrors. The expansion factor 4 is chosen so that the expanded beam slightly overfills the back aperture of the objective which provides good focusing and consequently stiff optical trapping [141]. Backscattered laser light is blocked by a dual-notch filter (Semrock, 532/1064). Images and frame sequences up to 30 fps can be recorded using a digital camera Canon EOS 550D. Spectra of trapped objects can be recorded using a spectrometer (Princeton Instruments, Acton SP2500, LN/1340X400BR Excelon).

Note: The objective used for this study does not have a chromatic abberation correction for the wavelength 1064 nm. As a result, the laser beam is focused below

the objective focal plane. This mismatch is corrected by pre-focusing the beam using a plano convex lens with 1 m focal length placed 60 cm before the objective.

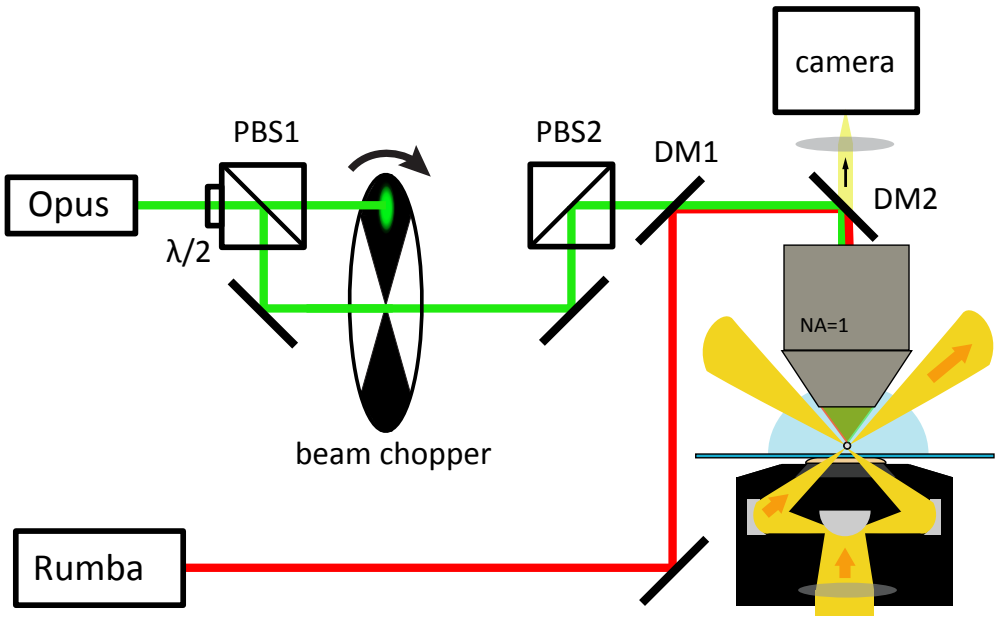

Figure 3.3 | Schematic of the experimental setup used for the microscale mapping of oscillatory flows in Chapter 5. The setup is based on a dark-field microscope equipped with three optical traps. Two of the traps are formed by splitting the beam of a a 532 nm laser. A beam chopper switches these traps on and off with a tunable frequency. The third optical trap is formed by focusing the beam of 1064 nm laser. The 532 nm and 1064 nm traps are used to trap a source and a detector particle, respectively (see Figure 3.4). A high-speed camera allows for recording of source and detector motion at 1000 fps.

3.1.3 Optical Setup 2

The oscillatory microfluidics study presented in Chapter 5 requires three optical traps in addition to the dark-field microscope. One of the traps is used for trapping a single silica sphere, which serves as an opto-fluidic force detector. The remaining two traps are used for the construction of a dipolar oscillator, serving as a source of fluid oscillations. Figure 3.3 shows a schematic of the complete experimental setup.

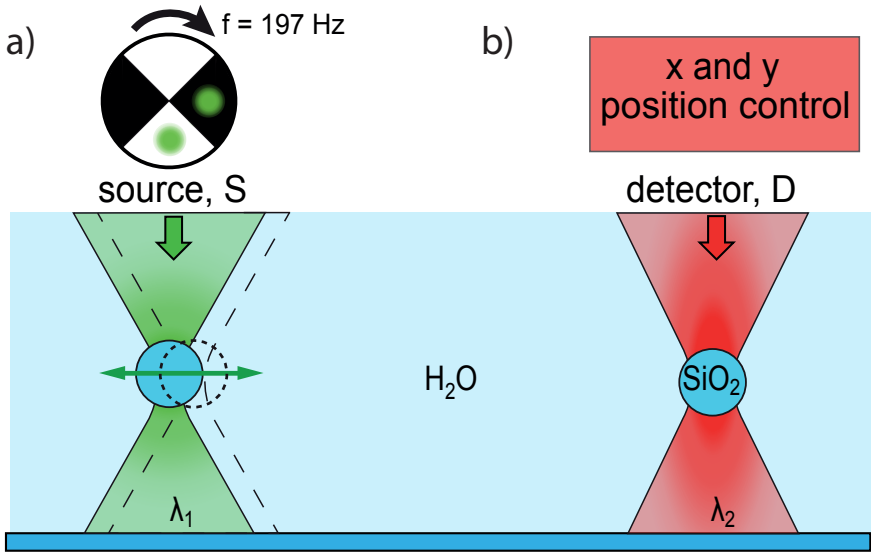

Figure 3.4 | Working principle of the optically driven microscale oscillator in Chapter 5 and the corresponding microfluidic detector. a) A trapped silica sphere with diameter of 1.76 µm oscillates between two optical traps (of equal power, $P = 60\,\text{mW}$) separated by distance of 405 nm. Both traps are switched periodically ($f = 197\,\text{Hz}$) on and off such that only one is on at a time. Since the sphere is attracted by each of the traps, it follows the one that is on at the time. As a result, it begins to oscillate between them. b) Trapped silica sphere with diameter 1.76 µm serves as a microfliudic detector. The displacement of the sphere allows for determination of the velocity of the fluid around it. It can be positioned at any point of the focal plane using two steering mirrors.

3.1.3.1 Dipolar Source

The microscale source of water oscillations, central for the studies in Chapter 5, is realized by two optical traps positioned 405 nm away from each other. Both traps are formed in the objective focal plane and are used for three dimensional trapping of a single silica spheres ($d = 1.76 \pm 0.04\,\mu\text{m}$, microParticles GmbH, Zeta potential $= -10\text{mV}$). They are created using a 532 nm CW laser (Laser Quantum, opus 532). The beam of the laser is expanded for efficient trapping and split into two beams using a *polarizing beam splitter* (PBS). A half wave plate in front of the PBS is used to adjust the laser power of each of the beams so that they are equal. Both beams are coupled back together using a second PBS and two mirrors. The mirrors are used to steer one of the beams with respect to the other, thus defining the spacing between the two traps. A laser beam chopper is used to block one of the beams at a time. The

modulated beams are focused through the objective lens. They form two, closely spaced optical traps alternating on and off. Once a single *silica* sphere is trapped, it is driven to oscillate between the traps along the x-axis (as indicated with the green arrow in Figure 3.4) at a frequency of $f = 197\,\text{Hz}$ defined by the laser chopper. The oscillating sphere acts as a dipole-like source of oscillatory flow in the medium around it. The amplitude of this source can be tuned by changing the separation between the traps. Its frequency is defined by the frequency set at the laser beam chopper and its orientation is defined by the position of the two traps with respect to each other.

3.1.3.2 Microfluidic Detector

Our opto-fluidic force detector is an optically trapped *silica* sphere with diameter $1.76\,\mu\text{m}$ (microParticles GmbH). The detector trap is constructed using a $1064\,\text{nm}$ CW laser (Cobolt, Rumba) expanded 5 times by a beam expander (Edmund Optics). The expanded laser beam is then coupled to the dark-field microscope described above via two 2-inch steering mirrors. Finally, the beam is focused through a water dipping objective (Zeiss WPlan-Apochromat 63x/1.0, VIS and IR) resulting in an optical trap in the focal plane with a position that can be defined by the steering mirrors.

Note: Detector and source beads are optically trapped in the same plane since the microscope objective is corrected for chromatic abberations for the visible and infrared region of the electromagnetic spectrum.

3.1.3.3 Detector Positioning

The detector bead can be placed in different positions around the source bead using the two-inch steering mirrors. Backscattered laser light from the bead is used as feedback granting no walkoff of the detector optical trap at the new position in the focal plane of the microscope objective. First the dual-notch filter (Semrock, 532/1064) is replaced by a long wave pass filter (Semrock, Edge Basic 532). Then, the

detector is moved to its new position using the steering mirrors. The backscattered light pattern is imaged by a high-speed digital camera (pco.dimax HD). After the desired new position is reached the filters are exchanged again. The motion of the particle is then recorded for 10 s using the camera at sampling rate of 1000 fps. The procedure is repeated until the whole region of interest in the focal plane is measured.

3.1.3.4 Detector Trap Calibration

As mentioned in section 2.3, in order to measure forces with optical tweezers one has to find the proportionality constant relating the particle displacement and the force acting on the particle. The method for finding k was chosen to be PSD fitting (see subsection 2.3.1) because it provides the highest precision in the pN force range [88, 91].

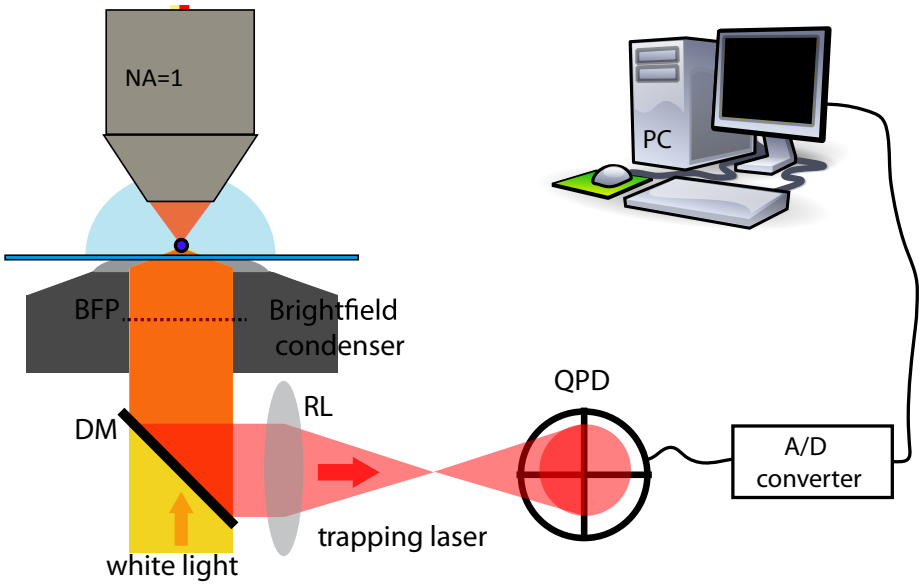

Figure 3.5 | Experimental setup suitable for force calibration of optical tweezers. Instead of a dark-field condenser the setup is equipped with a bright field condenser used to simultaneously illuminate and track a trapped particle. The condenser collects the light of the trapping beam and guides it to its *back-focal-plane*. The focal plane is then shifted to a photodiode with four quadrants (4QPD) via a relay lens [142]. The output voltages of the four quadrants are then sent to an analog digital converter and recorded with a PC.

This method requires acquisition of the Brownian motion of a trapped particle with high temporal resolution (sampling rate $10 - 100$ kHz). Figure 3.5 shows a

schematic of a modified version of Optical Setup 2 (Figure 3.3) which allows for such measurements. The setup in Figure 3.5 is designed for particle tracking via *back-focal-plane interferometry* (BFPI), the principle of which is shown in Figure 3.6. BFPI takes advantage of the fact that a small displacement of a trapped object at the focal plane of a microscope objective results in a well pronounced change in the interference pattern (the intensity distribution) on the back-focal-plane of the condenser lens. For an empty trap, the intensity distribution at the BFP is axis symmetric. Consequently, one can place the photodiode in a way that all four quadrants collect equal amounts of laser light (beam axis at the center of the diode). Once this is done, a particle is trapped. The intensity distribution in the back-focal-plane of the condenser shifts its center of mass proportionally to the motion of the particle in the trap. The effect is due to interference between the light scattered by the particle (in the forward direction) and the unperturbed (unscattered) beam (see Figure 3.6). As a result, the motion of the particle can be recorded in terms of output voltages of a 4QPD (see Figure 3.6).

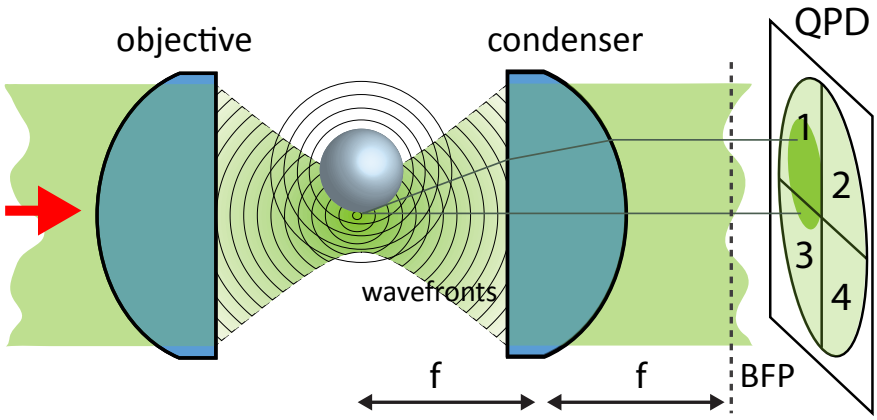

Figure 3.6 | Back-focal-plane Interferometry

The setup in Figure 3.6 is aligned for empty trap such that the x and y coordinates (in volts) are zero. A particle is then trapped and its Brownian motion is recorded via the 4QPD output voltages with sampling rates of 10kHz. A trapped particle displaced from the equilibrium position scatters laser light which in turn interferes with the unscattered part of the beam. The interference pattern on the back-focal-plane of the condenser lens shows a constructive interference region displaced from the center

of the 4QPD. This displacement is proportional to the displacement of the particle from the beam axis. The Brownian motion of a trapped particle in x,y and z can be recorded as a voltage sum of the four quadrants: $x = (2+4)-(1+3)$, $y = (1+2)-(3+4)$ and $z = (1+2+3+4)$. Provided that the drag coefficient of a trapped particle is known, its coordinates in Volts can be used directly (without conversion into meters) to determine the trap stiffness k (see subsection 2.3.1).

3.2 Sample Preparation

3.2.1 Preparation of Janus Particles

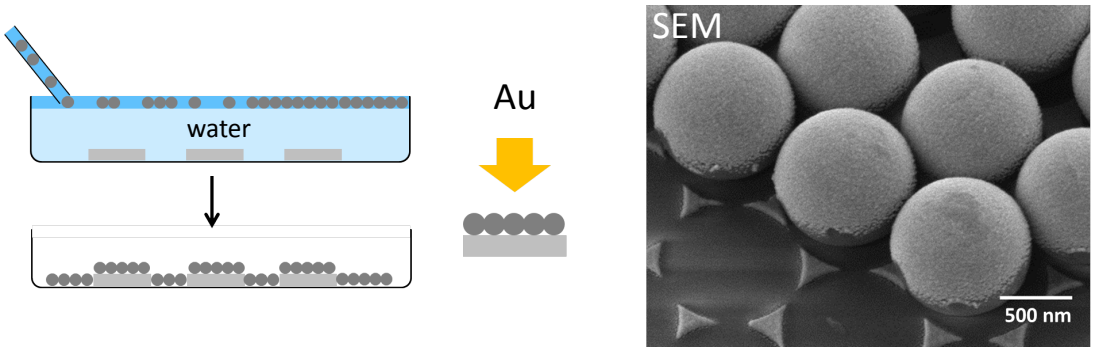

Figure 3.7 | Preparation of Gold/Silica Janus Particles: First, a monolayer of particles in water is assembled on top of a glass substrates. Once the sample dries, the particles are immobilized on the glass substrates and are placed in an evaporation chamber. There, a gold layer of 5 nm is evaporated on one side of the particle monolayer. Scanning electron microscope (SEM) image was made by Paul Kühler.

For the studies in Chapter 4, gold/silica (Au/SiO_2) particles were produced by evaporation of a thin gold layer onto silica microspheres. For that purpose, a monolayer of silica spheres with diameter 1.3 µm (Microparticles GmbH) was self-assembled on a surface of ultrapure water (Milli-Q). The monolayer of particles was then deposited on borosilicate glass coverslips by slowly pumping out the water (3.7). Afterwards, a 5 nm gold layer was evaporated onto the silica spheres with a thermal evaporator(Leybold) at a rate of 0.1 nm/s. Next, the Janus particles were dispersed in water by briefly immersing the substrate in a water-filled beaker which was held in an ultrasonic bath (Elma X-tra 50H) for 2 s.

3.2.2 Preparation of Glass Coverslips

The glass coverslips used in this thesis are 24x24 mm large and 0.17 mm thick. To clean the coverslips, they were first sonicated in acetone, then in 10% Hellmanex solution and finally in Milli-Q water for 10 min. Finally, the coverslips were blow-dried using a nitrogen gun and stored in wafer holders.

For some of the measurements it was necessary to coat the coverslips with a polymer layer. This was achieved using the following established method [143]: The cleaned substrates are first plasma etched for 60 s using a FEMTO equipped with a RIE electrode (Diener Electronic, Germany). Then they are immersed for 1 hour in a solution of polydiallyldimethylammonium chloride (PDADMAC) at 2 mg/ml in a 0.5 M solution of sodium chloride (NaCl). Finally, the coverslips are rinsed in Milli-Q water and dried again by a nitrogen gun.

4 Optothermal Elevation of Plasmonic Janus Particles

This chapter presents a study on Janus microswimmers, composed of a silica sphere with a gold half shell, in a single beam optical trap. It is demonstrated how plasmonic Janus particles can not only be stably trapped by optical tweezers, but also controllably displaced along the axis of the laser beam through an interplay between optical and thermal forces. Scattering forces orient the asymmetric particle, while strong absorption on the metal side induces a thermal gradient, resulting in particle motion. An increase in the laser power leads to an upward motion of the particle, while a decrease leads to a downward motion. A study of the reversible axial displacement revealed a hysteretic jump in the particle position that is a result of the complex pattern of a tightly focused laser beam structure above the focal plane. Additionally, simultaneous trapping of a gold nanoparticle and a plasmonic Janus particle is presented, suggesting first practical applications of the system. This photonic microscale "elevator" is a promising tool for thermal force studies, remote sensing, as well as for optical and thermal micromanipulation experiments.

4.1 Principles and Calculations

We use optical tweezers to study the behaviour of plasmonic Janus particles upon laser illumination. As revealed above, optical tweezers is a standard tool for manipulation of micro and nanoscale particles [22, 69]. Stable 3-dimensional optical trapping of individual microscale plasmonic Janus particles, however, has been challenging and to the best of our knowledge not reported until now. This is due to strong scattering forces acting on the particle combined with the efficient heat generation in the metal resulting in a large thermophoretic force and subsequent ejection from the trap. Merkt et al. [23] have reported two dimensional rotational motion around the trap as the result of competing optical forces on the particle. In our studies, we employ gold/silica particles. They were produced by evaporation of a 5 nm gold layer onto silica microspheres with a diameter of 1.3 µm by the method described in section 3.2.1. Because the gold layer is only 5 nm thick, it does not form

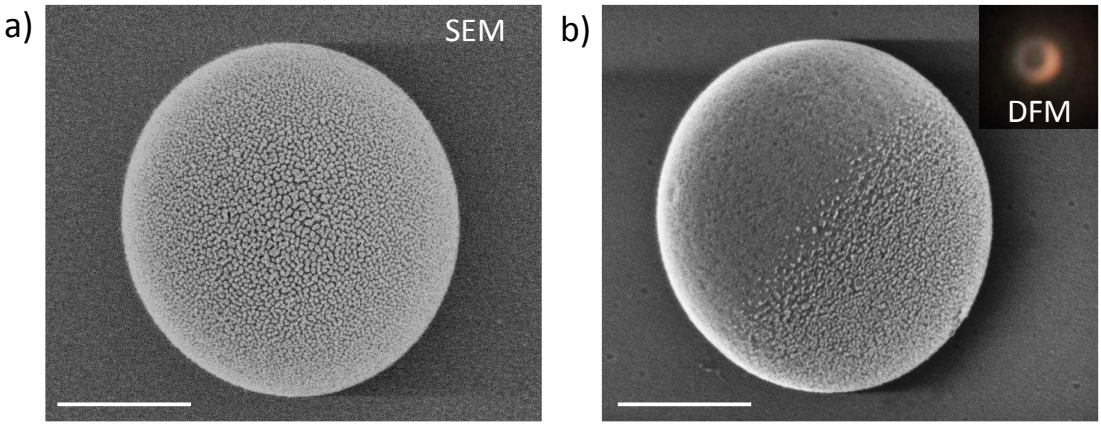

Figure 4.1 | SEM image of a 1.3 µmSiO_2/Au Janus particle with a 5 nm Au coating after (a) being trapped and pulled upward into a sticky polymer (gold side always visible) and (b) settling a sticky polymer under gravity. Inset is a dark-field image of the sedimented particle. Scale bar = 500 nm.

a complete film (see section 2.4.2). Instead, the gold forms small islands on top of the sphere, as seen in the scanning electron microscope images in Figure 4.1. On one hand, evaporating a thicker layer can produce a continuous gold film. However, these particles cannot be optically trapped due to the stronger scattering (repulsive) force caused by the gold film. On the other hand, a thinner gold layer will reduce the

plasmonic properties of the particles shifting their optical response closer to that of a bare silica sphere.

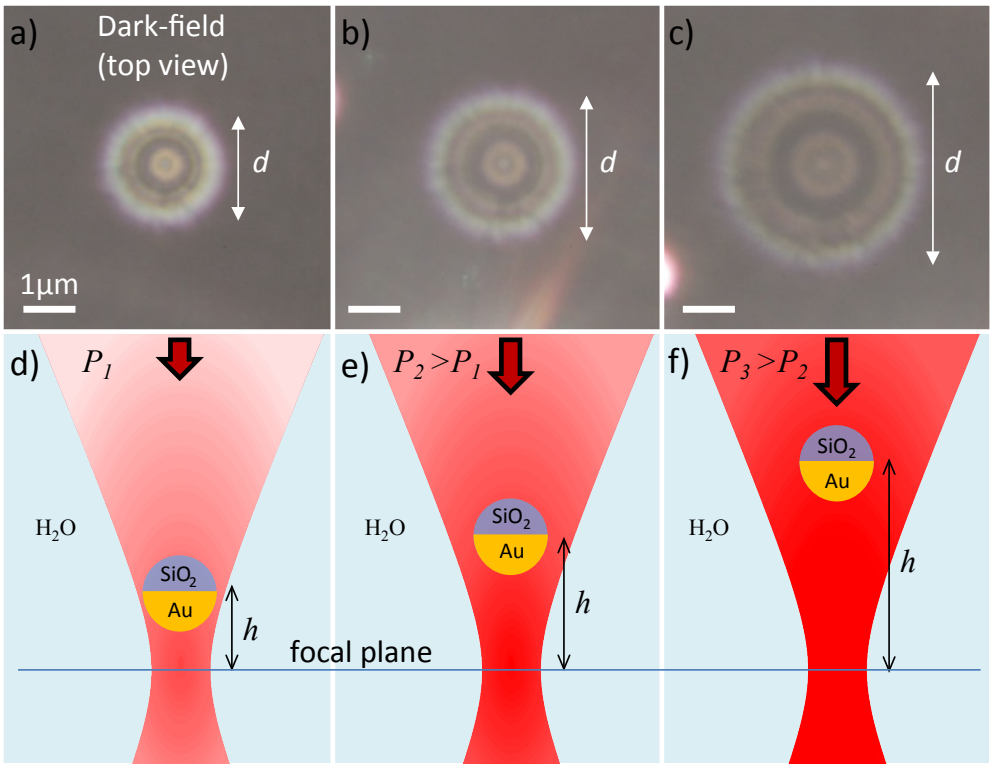

Figure 4.2 | (a-c) Dark-field images of a Janus particle in an optical trap for increasing laser powers (left to right). (d-f) Schematics with the incident illumination from above the experimental situations of (a-c). Increasing the laser power causes a reversible axial displacement in a direction opposite to the beam propagation.

4.1.1 Janus Particle in an Optical Trap

To study the behaviour of Janus particles in focused laser beam, we performed measurements using the dark-field trapping setup described in subsection 3.1.2. First, a small drop (50 – 100 µl) of an aqueous solution containing the Janus particles at low concentration is applied to a microscope cover slip. The microscope objective is then inserted directly into the drop. The near-infrared (1064 nm wavelength) optical trap is switched on and brought to the nearest particle imaged by the dark-field microscope. The Janus particles could be stably trapped in 3 dimensions. However,

the particles are not trapped in the focus of the laser beam. Instead, they are displaced axially above the focal point. This can be clearly seen by the defocussed rings stemming from the scattering of the Janus particles in dark-field images in Figure 4.2. Remarkably, the axial position of the Janus particle is not fixed, but is found to depend on the power of the trapping laser. Upon increasing the trapping laser power, the rings become larger (Figure 4.2b,c). The experiments showed that the effect is reversible. If the laser power is decreased, the rings become smaller. Thus, the higher the laser power is, the farther the Janus particle is pushed upwards with respect to the laser focus (Figure 4.2d-f). By adjusting the power, it is thus possible to steer the particle up and down within the trap, effectively creating a microscale photonic elevator. It is well known that the size of the observed rings is linearly dependent on the displacement of the particle from the focal plane, which we call *height* [144, 145]. To quantify the axial position of the trapped Janus particles, we performed an experiment allowing for the determination of the proportionality constant linking the diameter of the rings and the height. This constant is specific for each imaging system but easy to obtain. A Janus particle was fixed to the substrate and placed in the focal plane of the objective lens. The substrate was then shifted upwards, in steps with know height, using a three dimentional nanopositioner stage (PI, P-513). The size of the outer scattering ring was measured at various heights. With the obtained ratio of the measured ring size and the known distance from the focal plane, one can determine the *height* of the Janus particles in the optical trap.

4.1.2 Forces

All of the forces acting on the Janus particle were considered in order to qualitatively understand how these particles can be stably trapped far above the optical focus (Figure 4.3). Both components of the optical force, the scattering and the gradient force, act downwards on the Janus particles guiding them towards the focus of the laser beam. This is true as long as the particle is above the focal plane. The gravitational force acts in the same direction (if we assume that the particle is moving on the beam axis). Buoyancy acts in the reverse direction. A rough estimate (no gold layer considered) of the buoyancy and gravitational force is given using the density

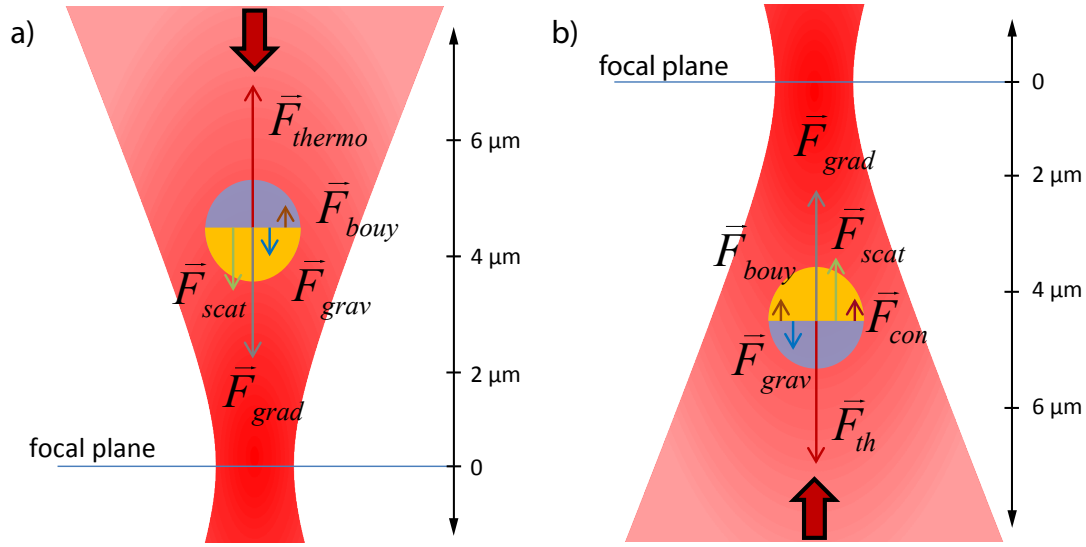

Figure 4.3 | a) Force diagram of the microelevator system in an upright configuration. Thermal force, the sum of the thermophoretic force and the force on the particle caused by convection of water, balances out with the optical forces and gravity. b) Force diagram of the microelevator system in an inverted configuration. The thermal force splits into two counteracting components, convection force F_{con} and thermophoretic force F_{th}.

of the silica particle and the water at room temperature, ρ_P and ρ_W, respectively, the diameter of the particle, D_P, and the gravitational acceleration, g:

$$|\vec{F}_{grav}| = \frac{\pi}{6} \cdot \rho_P \cdot D_P^3 \cdot g = 3.74\,\text{fN} \tag{4.1}$$

$$|\vec{F}_{buoy}| = \frac{\pi}{6} \cdot \rho_W \cdot D_P^3 \cdot g = 1.41\,\text{fN} \tag{4.2}$$

While the direction of the optical force is known, determining its magnitude proves more difficult. Due to the broken symmetry of the system, together with the complex geometry of the island-type gold layer, no analytical solution for the optical force exists. Moreover, the huge size difference between the silica sphere and the gold layer makes the system extremely difficult to handle numerically. We can, however, calculate the optical forces for a simple silica sphere of the same dimensions as the precursors used for the Janus particles. In this simplified geometry, the forces can be directly calculated using the generalized Mie theory described in section 2.2.3. This is done for the same parameters used in the experiment: laser wavelength 1064 nm,

NA= 1.0, $D_{JP} = 1.3\,\mu m$, laser power $P_{laser} = 4-12\,mW$ and the corresponding P_{laser} distances from the focal plane. For $P_{laser} = 4\,mW$ we obtain an optical axial force $F_z = 29.5 \pm 3.5$; $F_z = 70 \pm 5\,fN$ is obtained for the 12 mWcase. These values are lower than what the actual ones are since they do not include the scattering and absorption contribution from the gold layer. Nevertheless, these values are roughly an order of magnitude stronger than the buoyancy and gravitational forces, and without an additional force in the upward direction, the Janus particle would move towards the laser focus. The additional force acting on the Janus particle is due to the absorption of light by the gold semi-shell (see section 2.4.2). This leads to a strong heat increase in the gold and the surrounding water resulting in a thermophoretic force discussed in section 2.4.3. Accordingly, to counterbalance the optical forces together with gravity, the thermophoretic force must be of the order of several tens of femtonewtons and pointing upwards:

$$\vec{F}_{tot} = -|\vec{F}_{grav}| + |\vec{F}_{buoy}| - |\vec{F}_{scat}| - |\vec{F}_{grad}| + |\vec{F}_{thermo}| \tag{4.3}$$

The force model suggested above requires the Janus particle to have a fixed orientation inside the trap. Moreover, it has to be oriented with the gold part pointing towards the laser focus. To verify this, the orientation of the Janus particle inside the trap was determined experimentally. To this end, we added a second cover slip, coated with a polymer (polyDADMAC) to the experiment, sandwiching the Janus particle solution. A drop of water, into which the microscope objective was subsequently inserted, was applied to the second cover slip. We again trapped a Janus particle and then shifted the laser focus upward (by moving the sample away from the objective) until the trapped particle stuck to the polymer, becoming attached to the top cover slip. Imaging the decorated substrate surface in an SEM let us determine the orientation of the Janus particle inside the trap (Figure 4.1a). As can be seen, the gold surface faced away from the surface. This was the case for all 10 Janus particles affixed to the substrate in this manner. The orientation of the particle can be explained by the scattering force. It causes the trapped particle to rotate so that the gold surface points in the direction of beam propagation. In general, a polymer can be sticky for one material and repealing for others. In order to eliminate the possibility of preferential attachment, a control experiment was performed.

We let Au/SiO_2 particles sediment on a coverslip coated with polyDADMAC. The orientation of the affixed particles in the first experiment was in clear contrast to Janus particles that attached via sedimentation. In the later case, the particles were generally lying on their side (Figure 4.1b). As a consequence, the thermophoretic force acting on the Janus particle in the laser beam points upwards, counterbalancing the other forces and enabling the particle to be stably trapped above the laser beam focus (Figure 4.3a). To clarify the role of gravity and the convection flow contribution to the thermal force, we considered the same experiment in an inverted microscope set-up. In this case, the laser propagation direction is inverted, so the orientation of the particle and all of the forces are in the opposite direction, with the exclusion of gravity and the force caused by water convection (Figure 4.3b). The same microelevator behavior was observed in this inverted configuration, except with a downward axial displacement. This experiment ruled out convection as the mechanism of the axial displacement, because the power dependent displacement due to convection would be upward in either experimental configuration. The other possibility is self-thermophoresis resulting in a force on the trapped particle in the direction of which is fixed by its orientation. The experiment also confirmed that gravity does not play a pivotal role as a downward restoring force, as this would lead to a downward ejection in the inverted set-up. Consequently, the combined optical forces are the restoring force keeping the particle from ejection and together with the thermophoretic force are the dominant forces in this experiment. The strength of these two main counteracting forces depends differently on the laser power enabling stable trapping and leading to the upward and downward motion of the Janus particle with increasing and decreasing laser power, respectively.

4.1.3 Principle of Motion and Equilibrium Points

The thermophoretic force F_{th} and the total optical force F_{opt} depend differently on the laser power. We denote the *power of the laser light interacting with the particle* with P_p. The magnitude of P_p depends on two parameters - the particle height and the total laser power. An increase in the total power naturally leads to an increase of P_p if the particle does not move. An increase in the particle height (the distance

from the focus), on the other hand, leads to a decrease of P_p. These two ways of tuning the power at the particle are essential for stable trapping positions, as well as for the motion of the microelevator. A schematic of the principle of motion and the force equilibrium points is shown in Figure 4.4. First, the particle is trapped above the focus at a point E_1. At this point, there is an equilibrium between the optical force

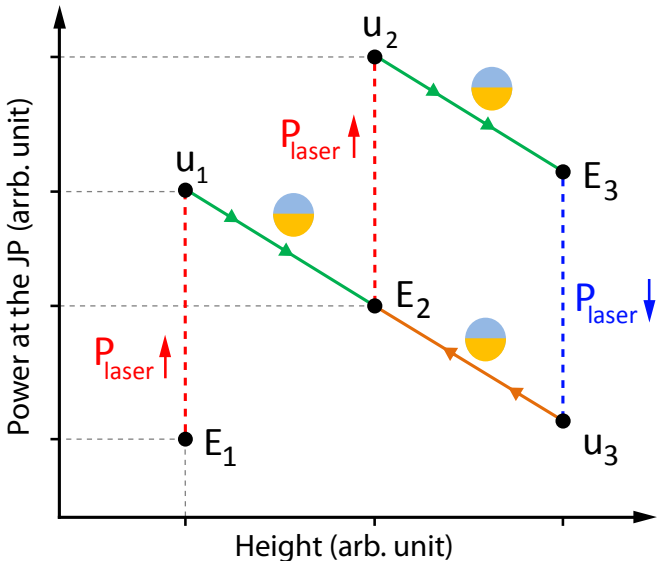

Figure 4.4 | A schematic of the motion of Janus particle in an optical trap as a function of the laser power. Stable trapping positions and disequilibrium positions are denoted with **E** and **u** respectively.

F_{opt} acting downward and the thermophoretic force F_{th} acting upward. An increase of the laser power P_{laser} leads to an increase of $P_p(h, P_{laser})$, thereby distorting the force equilibrium (point u_1). As a result, the particle moves upward. This is due to the steeper dependence of F_{th} on the power in comparison to the optical force F_{opt}. The upward motion leads to a decrease of $P_p(h, P_{laser})$. As a result, both F_{th} and F_{opt} decrease. Since $F_{th}(P_p)$ not only grows but also decreases faster than F_{opt}, both forces equalize in a new equilibrium position E_2. The processes repeat for a further increase of the total laser power. If the laser power is decreased, then F_{th} can no longer balance out the optical force (point u_3) since its magnitude is decreased more than that of the optical force. The particle thus moves downward, which in turn leads to an increase of P_p, and the faster increasing F_{th} equalizes with the optical force at point E_2. Unless the properties of the surrounding medium change, this process can

be repeated unlimited number of times without a change of the equilibrium positions corresponding to the applied laser powers.

4.2 Potential Landscape Effects

The limits of the particle displacement were tested by increasing the laser power, starting at the lowest power (approximately 3 mW) at which trapping was possible. Increasing the laser power led to a displacement of the particle in a nearly linear fashion shown in Figure 4.5a. As the actual size of the particles and the thickness of the gold varied, the exact height (as a function of P_{laser}) varied accordingly, yet we obtained an average displacement capability of approximately 330 nm per mW of trapping laser power. Astoundingly, at around 13 mW trapping power, the linear fashion was interrupted by a discontinuity. The particle jumped inside the trap, moving by roughly 5.3 µm, more than ten times the amount previously determined. Further increasing the laser power led again to a nearly linear displacement of

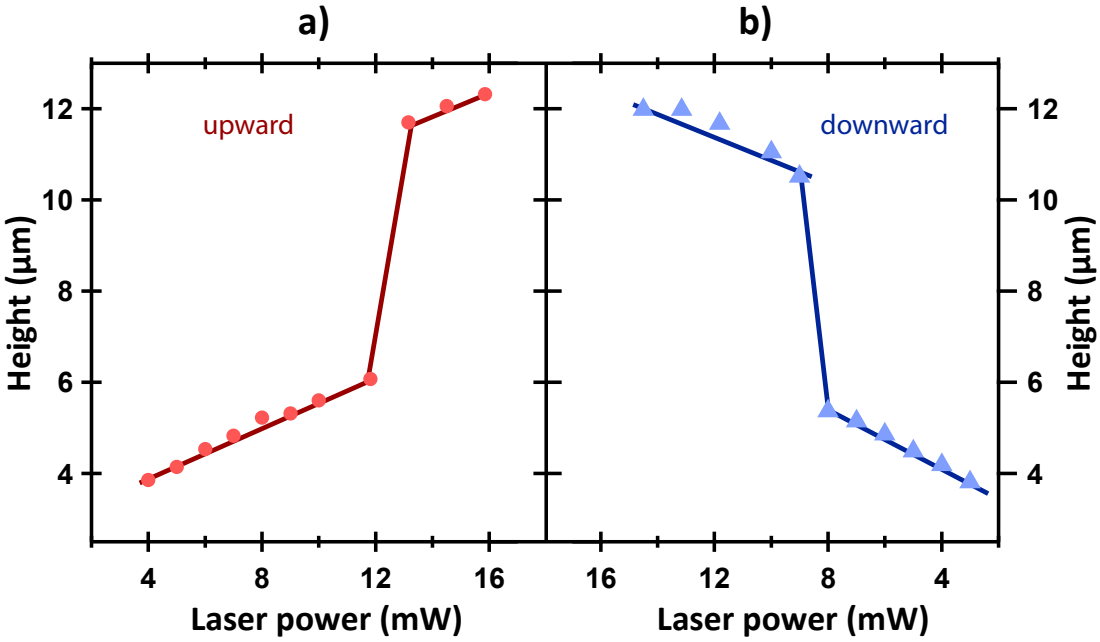

Figure 4.5 | Axial displacement (height) as a function of a) increasing and b) decreasing trapping laser power. Increasing the laser power leads to an upward motion of the Janus particle, while a decrease in the laser power leads to a downward motion.

the Janus particle, with roughly the same slope as determined for low trapping powers. Reversing the direction by reducing the trapping power initially resulted in a linear decrease in particle displacement with the same slope (Figure4.5b). The linear fashion in this reverse process was also interrupted by a discontinuity. The jump had a similar magnitude of 5.4 µm, albeit at a lower laser power of approx. 11 mW and consequently at a different axial position. Decreasing the power even further again led to a linear decrease of the displacement with the slope again of the same size as in the forwards process. The measurement was repeated for many Janus particles. Each particle displayed a jump of the same distance from the focus, albeit at slightly varying laser powers, despite the aforementioned inhomogeneity between the particles. All studied particles displayed a hysteresis in the jump between upwards and downwards motion (Figure 4.5). These findings relate the cause for the observed discontinuity to certain characteristics of the optical trap (the focused laser beam). The jumping of the Janus particle was investigated further by modeling the intensity distribution of the laser beam using the same parameters as the experimental setup. High focusing (Fresnel number N<< 1) of a laser beam results in a complex 3-dimensional intensity pattern with multiple local maxima and minima. This structure has been investigated in detail previously using vector theory[146–149]. Here, we used the finite difference time domain (FDTD) method using the FDTD Solutions software to model the 3-dimensional intensity pattern relevant to our experiment. Due to the complexity of the system and the number of unknown parameters of the Janus particles, we looked only at the unperturbed light field and not what is modified through the presence of a trapped particle. Nevertheless, this simplification illustrates the cause of the discontinuity in the movement of the Janus particle upon changing the laser power. Figure 4.6a shows the spatial beam profile of a Gaussian beam focused through a thin lens of NA = 1.0. The expected complex pattern of local intensity maxima and minima can be seen above the central focal point. The light intensity averaged over the width of the particle along the beam axis is shown in Figure 4.6b. It is apparent that the light intensity at the particle oscillates between maxima and minima in the z-direction. Consequently, the sign of the intensity gradient, ∇I, oscillates between positive and negative values (Figure 4.6c) defining the direction of the gradient force. As the particle moves along the z-direction, it experiences an alternating pulling and pushing by

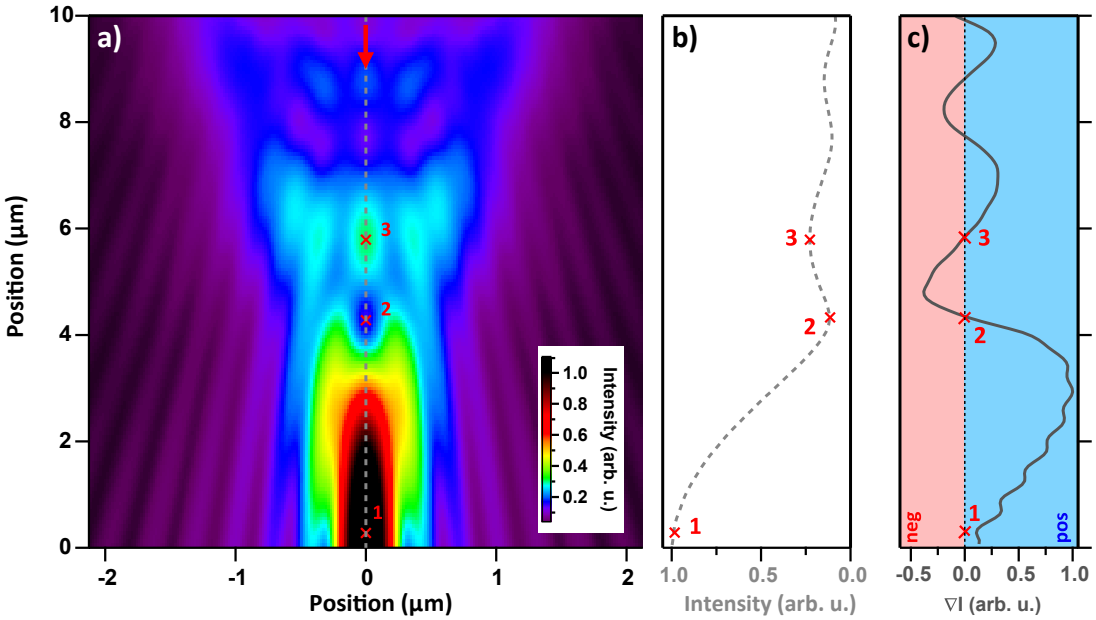

Figure 4.6 | a) Axial cross section of the intensity distribution (arbitrary units) of a focused Gaussian beam. The red arrow indicates the incident beam direction. b) The intensity summed over the cross section area of the Janus particle along the z-axis and c) the gradient of the intensity, ∇I.

the gradient force. These potential landscape effects explain the movement of the particle (including the discontinuity) observed when the laser power was increased. The promoted movement takes place as follows: first, an increase in the laser power disproportionately increases the thermophoretic force, driving the particle slowly upwards from its original position (point 1 in Figure 4.6a), as it was discussed above. Once the intensity gradient is reduced enough, it can no longer compensate for the thermophoretic force acting on the particle, and it moves upwards quickly, past point 2. Above the height of point 2, the gradient force becomes repulsive, driving the particle upward even more until a steady point is reached past point 3. At the steady point, the intensity gradient is once again positive and the gradient force balances out the thermophoretic force. Increasing the laser power further then leads to the upward movement of the particle seen in the experiments. The observed hysteresis of the particle jump is also explained by the intensity landscape. In both the forward and reverse case the Janus particle resists the change in position because it is attracted to the nearest local intensity maximum. The jump in the forward case

happens when the thermophoretic force becomes strong enough to overcome the potential barrier of the primary optical trap and push the particle upwards to the secondary trap. In the reverse case, the jump appears when the thermophoretic force is weak enough to allow the particle to settle into a position where it is mainly under the influence of the primary trap. In summary, the Janus particle trapped above the focus of a focused Gaussian beam sees an intensity landscape that is more complicated than in a classical optical trap. The multiple intensity peaks form smaller, secondary traps, which have been previously exploited and studied [150, 151]. Depending on the particle position, it can be attracted to one of those intensity peaks (traps). In our experiments, we observed only one jump due to the fact that beyond a certain height, the particle became too far out-of-plane to image.

4.3 First Applications

In all of the studies presented above the Janus particle was located several micrometers above the laser focus. Thus, the conventional optical trap can be employed for particle trapping in combination with the plasmonic Janus particle elevator. To explore the potentials of system, we used it to trap a 80 nm Au nanoparticle along with the previously trapped Janus particle (Figure 4.7). The Au nanoparticle was firmly trapped in all three dimensions at the focal point of the laser. No movement of the Au nanoparticle was visible in the dark-field microscope. At the time of trapping the particle and afterwards, there was no detectable effect on the height of the already trapped Janus particle. However, while the Au nanoparticle continued to remain stationary, the Janus particle could clearly be seen moving laterally inside the trap in circles around the beam axis. The later observation is a consequence of the secondary potential wells at the specific height discussed above. Applying different laser powers led, as before, to the Janus particle moving along the axis of the focused laser beam. As expected from the beam structure, as the height of the Janus particle increased, so also did the lateral motion of the particle. This experiment showed that the Janus particle does not modify the properties of the optical trap strongly, as the Au nanoparticles did not seem to be affected by the Janus particle becoming subsequently trapped. The experiment showed also that

the Au particle does not seem to disturb the trapping potential for the Janus particle, as this appeared to be trapped as stably as for the case without an additional trapped Au nanoparticle. Nevertheless, it was possible to optically control the distance between the Au nanoparticle and the Janus particle inside the trap, which, to our knowledge, is one of the first demonstrations of control of the separation between nanoparticles (a nanoparticle and a percolated film) within an optical trap. This control can potentially be exploited for several applications, such as remote sensing, force measurements or controlled heating.

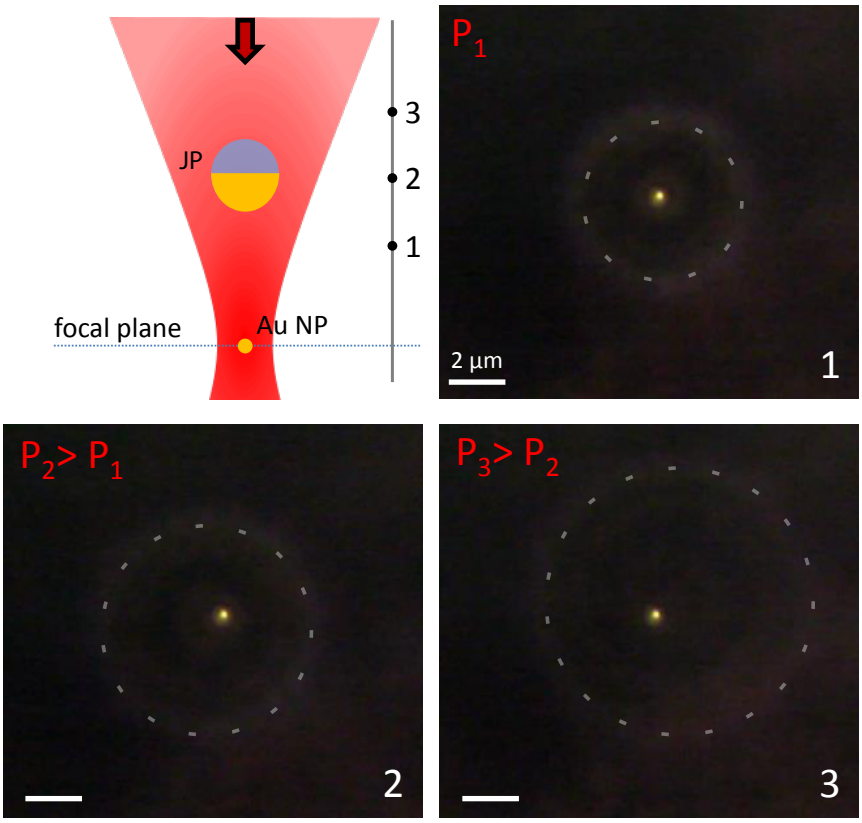

Figure 4.7 | Simultaneous trapping of a Janus particle (shown as white circle for better contrast) and an 80 nm Au sphere. While the sphere always stays in the same position, the height of the Janus particle varies according to the trapping laser power. Thus the distance between the two particles can be controlled through the trapping laser power.

4.4 Conclusion

In conclusion, we have demonstrated a controllable photonic microscale elevator composed of a gold/silica Janus particle in an optical-thermal trap. Compared to previous reports of optically induced thermophoretic motion of Janus particles, we have demonstrated unprecedented control over the particle height and orientation in a focused laser beam. The height at which the particle is trapped is determined by the equilibrium position at which the scattering, gradient and thermophoretic forces cancel out. It can be controlled in a highly reproducible way by adjusting the laser power. We observed a jump and a hysteresis effect on the position of the particle, which is otherwise linearly dependent on the laser power. Both the jump and the hysteresis effect are caused by the intensity distribution due to wave interference in the focused beam. The study described here opens the door to new high precision methods for controlling Janus microswimmers in and near optical traps. When combined with the variety of potential landscapes that can be produced via spatial light modulators (SLMs), it will be possible to move many Janus particles in complex, highly controllable configurations. We further extended the possibilities of this technique by simultaneously trapping a second 80 nm gold nanoparticle in the trap despite the Janus particle's presence. We showed that the distance between the nanoparticle and the Janus particle can be precisely controlled, leading to possible applications such as single molecule detection and force measurements.

5 Microscale Mapping of Oscillatory Flows

This chapter introduces an optofluidic method that allows the two-dimensional vectorial near-field mapping of oscillatory flows with micron-scale resolution. An oscillatory flow created by a microsource (an optically trapped silica particle set to oscillate in a dipole-type mode) is detected by another twin silica particle independently trapped and located in the vicinity of the source. Fourier analysis of the motion of the detecting particle at different points in space and time renders the vectorial velocity map around the oscillating microsphere. The method introduced here paves the way for in-situ characterization of fast mixing microscale devices and for new detection methods able to provide location and recognition (due to the field pattern) of moving sources that may be applied to both artificial and living microobjects, including macromolecules, cells, and microorganisms.

5.1 Basic Principles

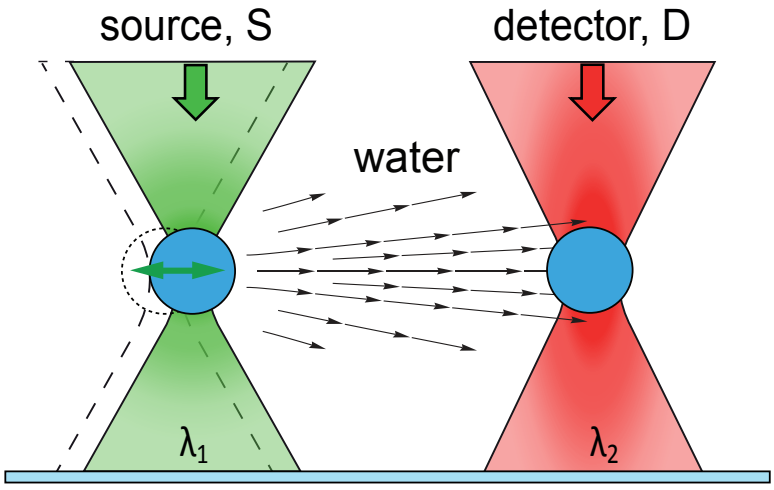

Figure 5.1 | Sketch of the interaction between detector and dipolar source via hydrodynamic flow. Both, the detector and the source are realized by trapping single SiO_2 spheres of 0.88 µm radius in water.

Detection of fluid motion on the micron scale requires force sensitivity on the piconewton scale. Optical tweezers provide this sensitivity via trapping and contactless manipulation of microparticles. We exploit the properties of optical tweezers to measure the vectorial velocity field around a microoscillator in water.

As discussed in subsection 2.3, a trapped particle is displaced at distance $|\vec{d}|$ when an external force is applied. At this distance, the external force is compensated by the optical restoring force (the gradient force). Its components are given by:

$$F_{opt,j} = -k_j \cdot |d_j| = -F_{ext,j}, \tag{5.1}$$

where $j = x, y$ and k is the trap stiffness (see section 2.2). Thus, knowing the trap stiffness and the displacement of the particle (including its direction) one can determine the magnitude and the direction of the external force acting on the particle. This method is widely used for force measurements in steady flows. However, if a trapped sphere is placed in an oscillating flow, as the one we want to study, it is a subject to a force of the form $\vec{F}_{ext}(t) = \vec{B} \cdot e^{i\omega_s t}$. The mean displacement of the particle, serving as a force detector, is then zero, as if there is no flow. To

overcome this hindrance, we process the motion of the particle in the frequency domain [139]. First, we record the motion of the detector particle in the plane of the microoscillator at a rate of 1000 fps. The position time series $d_x(t)$ and $d_y(t)$ are then Fast Fourier Transformed (FFT). The resulting amplitude-frequency plots in x and y directions show sharp peaks at the oscillating frequency of the source, $f_s = 197\,\mathrm{Hz}$ (see Figure 5.3c,d). The values at these peaks, given by

$$A_j(f_s) = \frac{2\sqrt{\mathrm{Re}\big(FFT(d_j)\big)^2 + \mathrm{Im}\big(FFT(d_j)\big)^2}}{n}, \tag{5.2}$$

provide the amplitudes of the detector oscillation caused by the dipolar source, which are the maximal displacements from the optical axis in x and y directions.

Consequently, the coordinates of the maximal external force on the detector particle are given by:

$$F_{ext,j}^{max} = k_j \cdot A_j(f_s) \tag{5.3}$$

Flow Velocity

To obtain the velocities of the fluid from the measured external force, we first determine its type. Since the detector particle interacts with the dipolar oscillator only via the water medium between them, the external force is a viscous drag force (Figure 5.1). Its magnitude, $|\vec{F}_{drag}|$, is given by the Stokes equation:

$$F_{drag,j}^{max} = 6 \cdot \pi \cdot \eta \cdot a_H \cdot u_j^{max} = F_{ext,j} = k_j \cdot A_j(f_s), \tag{5.4}$$

where η is the dynamic viscosity of water, a_H is the hydrodynamic radius of the silica sphere, and u is the speed of the water flow. The peak speed of the fluid in direction j can then be written as:

$$u_j^{max} = \frac{-k_j \cdot A_j(f_s)}{6 \cdot \pi \cdot \eta \cdot a_H}. \tag{5.5}$$

Consequently, the speed components are given by:

$$u_j(t) = u_j^{max} \cdot e^{i\omega_s t} \tag{5.6}$$

and the magnitude of the measured flow velocity is

$$|\vec{u}(t)| = \sqrt{u_x^2 + u_y^2} \cdot e^{i\omega_s t} \tag{5.7}$$

The flow velocity direction (the angle with the *x-axis*, θ_{exp}) is easily determined using the amplitudes $A_x(f_s)$ and $A_y(f_s)$ at the detector position. For measurements in the first quadrant it is given by

$$\tan(\theta_{exp}) = A_y / A_x. \tag{5.8}$$

The obtained magnitude and direction define the measured velocity of the fluid $\vec{u}$. In the sections that follow, we place the detector and record its motion at multiple points in the source oscillation plane. Then, using the method described above, we create a two-dimensional map of the flow velocity around it. Contributions due to Brownian motion of the detector particle are filtered out by the FFT and do not influence the final result.

5.2 Velocity Mapping

To demonstrate the capabilities of the method presented above, we quantitatively map the vectorial velocity field of an oscillatory flow in two dimensions around a microscale oscillator in water. The oscillator is chosen to be dipolar, thus serving as a model for oscillatory sources common in nature. The measurements are performed using a dark-field optical trapping setup described in subsection 3.1.3. Both the source and the detector are optically trapped silica spheres with diameter 1.76 µm. First, a small drop (100 µl) of aqueous suspension of spheres at low concentration is applied to a microscope cover slip. The microscope objective is then inserted directly into the drop. The near-infrared (1064 nm wavelength) optical trap is switched on and placed just on top of the substrate where a particle, later serving as a detector, is trapped. Next, a 532 nm wavelength laser trap is switched on in the same plane as the detector trap but 25 µm away. This is used to trap a second particle serving

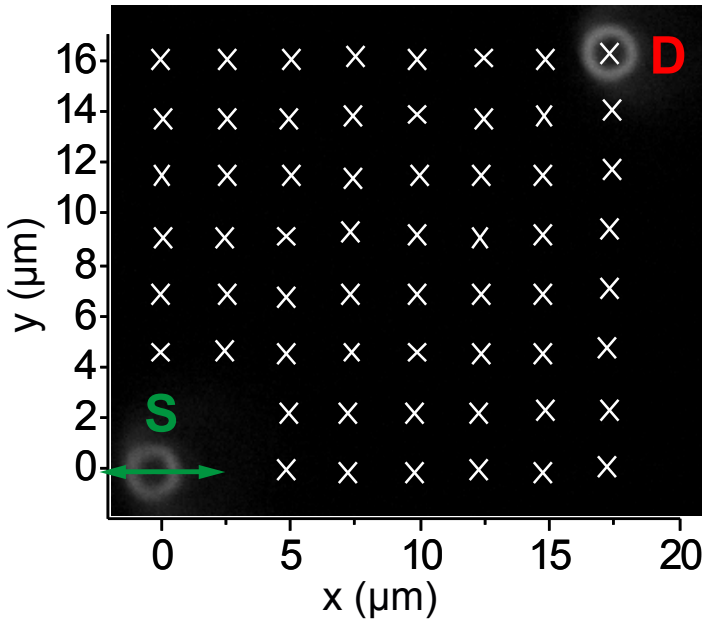

Figure 5.2 | Snapshot from a typical experimental video: The source is placed in the x-y plane at (0, 0). The detector position is varied with respect to the source according to the 60 markers [152].

as a source. The source bead is driven to oscillate between two traps (see subsection 3.1.3) along the *x-axis* indicated with the green arrow in Figure 5.2. The frequency of oscillation is set to 197 Hz, creating an oscillatory flow around the source. It is chosen such that it is of the same order of magnitude as those already reported for mixing in microscale systems [153, 154] and, at the same time, is not an integer multiple of 50 Hz. At 197 Hz, the position of the source bead resembles a harmonic function of the form $x_s = A_s \sin(\omega t)$, with $\omega = 2\pi f$ and the amplitude $A_s = (405 \pm 6)$ nm (see Figure 5.5). During the experiment, the source is permanently oscillating, while the detector bead is placed at different positions around it. To exclude additional drag caused by the substrate (wall effects), the trapping plane is lifted more than 100 µm away. Moreover, since the other spheres sediment, the lifted trapping plain is free of other particles, thereby providing obstacle free hydrodynamic interaction between the trapped particles. The detector particle is then placed at the first of 60 measuring

points. A dark-field image of the source and the detector particle is shown in Figure 5.2.

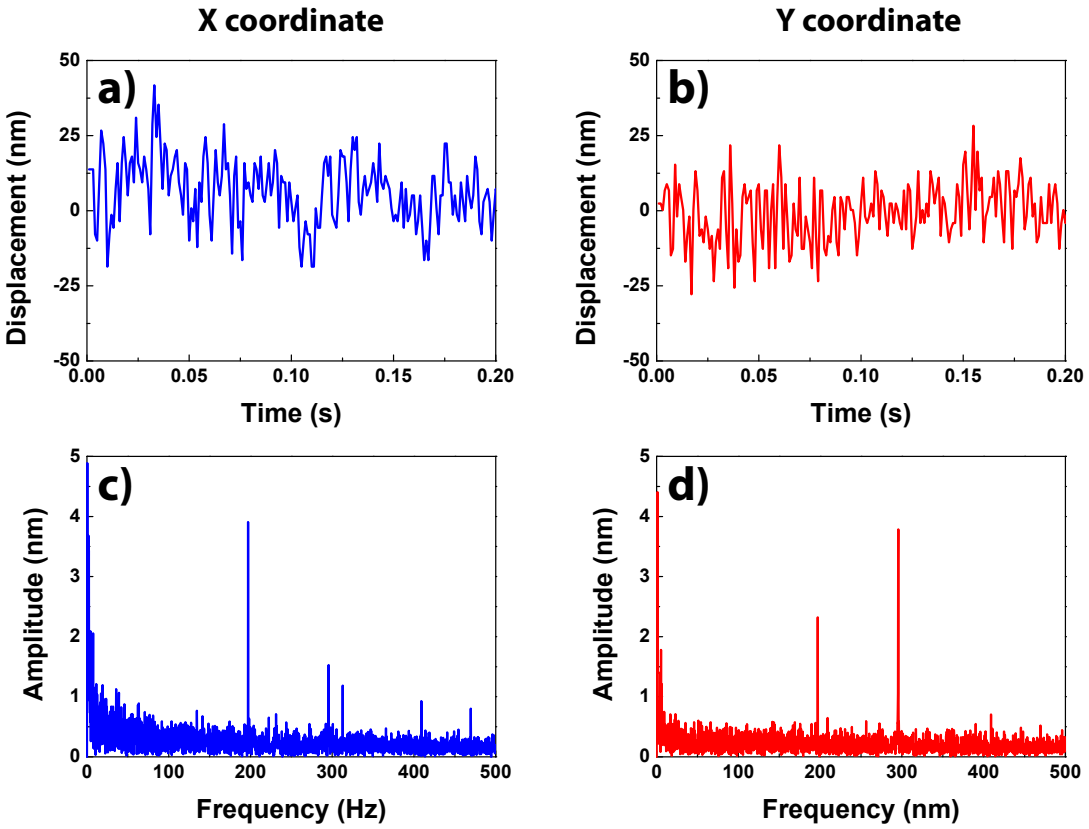

Figure 5.3 | (a) and (b): Trajectory of the x and y displacement, respectively, of the detecting particle at distance $\approx 25\,\mu m$ away from the dipolar source (see Figure 5.2). (c) and (d) show the corresponding FFT of (a) and (b).

The motion of both particles is recorded for 5 s with a high-speed camera at 1000 fps. After 5 seconds the detector trap is moved to the next measuring point of a previously created grid covering an area larger than $17 \times 16\,\mu m^2$ (see Figure 5.2). The motion of the particle in the new location is recorded ≈ 1 s after it has been reached. Back-scattered laser light from the particle is used as a feedback for eliminating laser walk-off in the new position. This is done by temporally replacing the notch filter, blocking the back-scattered light, with a long pass filter. The process is repeated again until the last point of the map is covered. To obtain the velocities at each measuring point, we first extract the detector coordinates $x(t)$ and $y(t)$ using a particle tracking software

Video Spot Tracker. They are then FFT using commercial software, Origin Pro. The obtained amplitudes are used to calculate the velocities, following the method presented above. We consider as the hydrodynamic radius the nominal radius ($a_H = a = (0.88 \pm 0.02)$), since the expected increment from the solvent layer $\approx 3\,\text{nm}$ is smaller than the size variation 20 nm. Analysis of different time ranges of the same measurement provides the same amplitude response, meaning that a steady state of the combined source and detector system is reached within 1 s. The 60 measured velocities $\vec{u}(x, y)$ reveal a two dimensional map of the vectorial velocity field around the source, presenting strong signal at distances 10× larger than the size of the source. Our key experimental result is displayed in Figure 5.4. It shows, in black, the

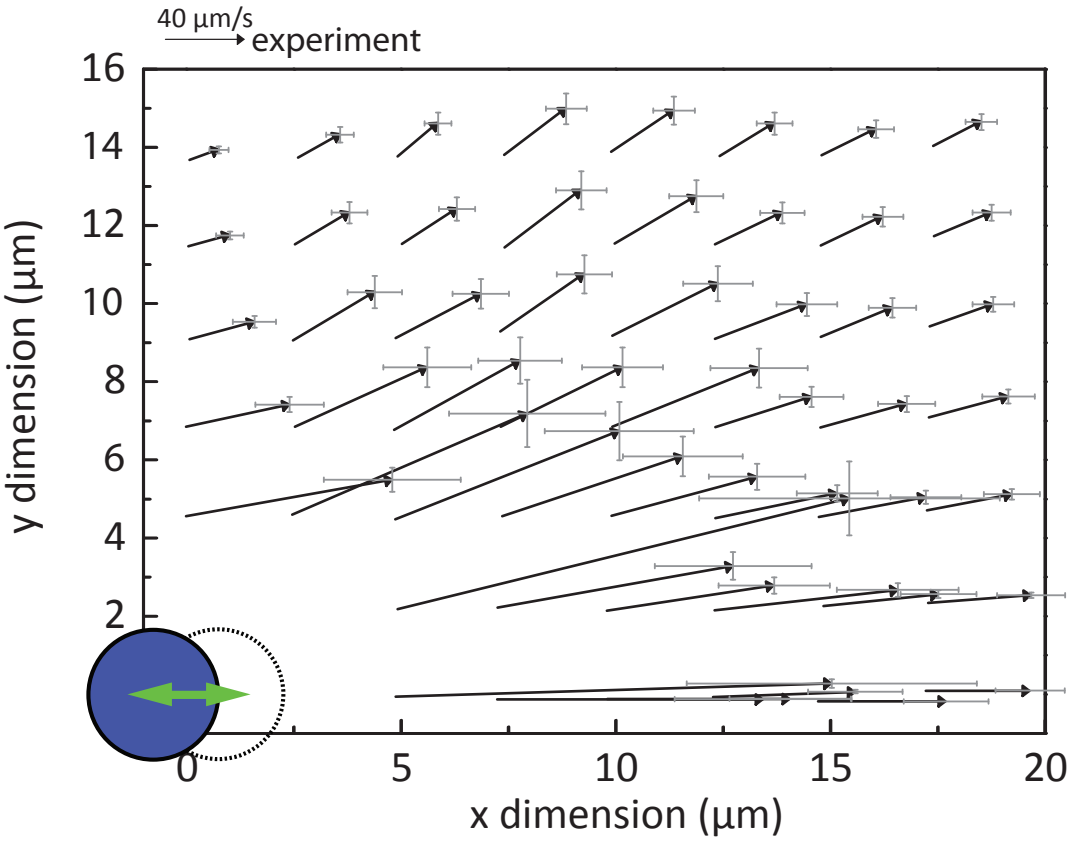

Figure 5.4 | Map of velocity of a water medium measured around a dipolar micro-oscillator. Black arrows display the direction and magnitude of the velocity field in each of the 60 measuring points. The corresponding error bars are shown in black. Vector scale bar = 40 m/s.

velocity field map measured close to the oscillating source and the corresponding

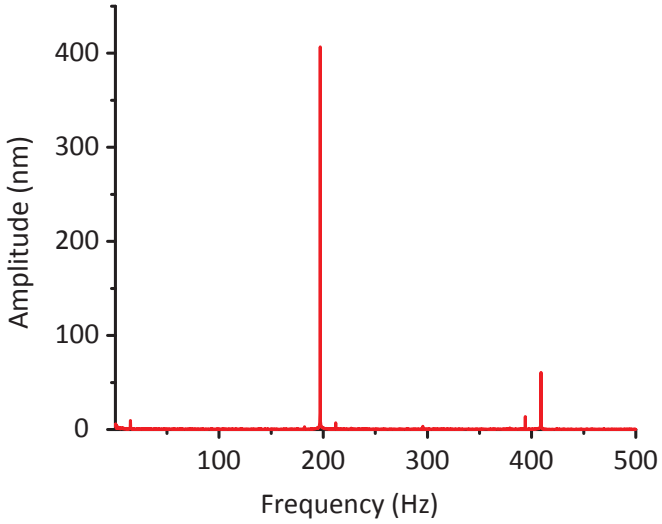

Figure 5.5 | FFT amplitude-frequency plot of the microscale dipolar source used in the experiments. The plot is obtained by FFT of the source position. It shows multiple small peaks besides the one at the oscillation frequency (197 Hz).

error bars ($\approx 9\%$), calculated through the propagation of error, are shown in grey. The arrows contain information of both the direction and the magnitude. No phase lag was found between the source and the detecting bead. The maximum velocity fields correspond to $\approx 250\,\mu m/s$, a value of the same order of magnitude as the maximum velocity of the source bead $500\,\mu m/s$. Moreover, strong signal (see Figure 5.3) is still detected when the detector bead is placed at $(x, y) \approx (17, 16)\,\mu m$ shown in Figure 5.2. The accuracy for the direction and magnitude of the velocity vectors is estimated to be $3\,deg$ and 3.5%, respectively. It was determined performing multiple repeated measurements with the same detecting particle. The remaining quadrants (below and to the left) exhibit the same signal in a symmetric fashion within the experimental accuracy. They do not provide different information about the flow around the oscillator.

5.2.1 FFT Peaks Analysis

The amplitude frequency plots in Figure 5.3c and 5.3d also show other peaks besides the one at the source frequency. These peaks are due to the contribution of other harmonics contained in frequency spectrum of the source, since it is not a perfect harmonic oscillator (see Figure 5.5).

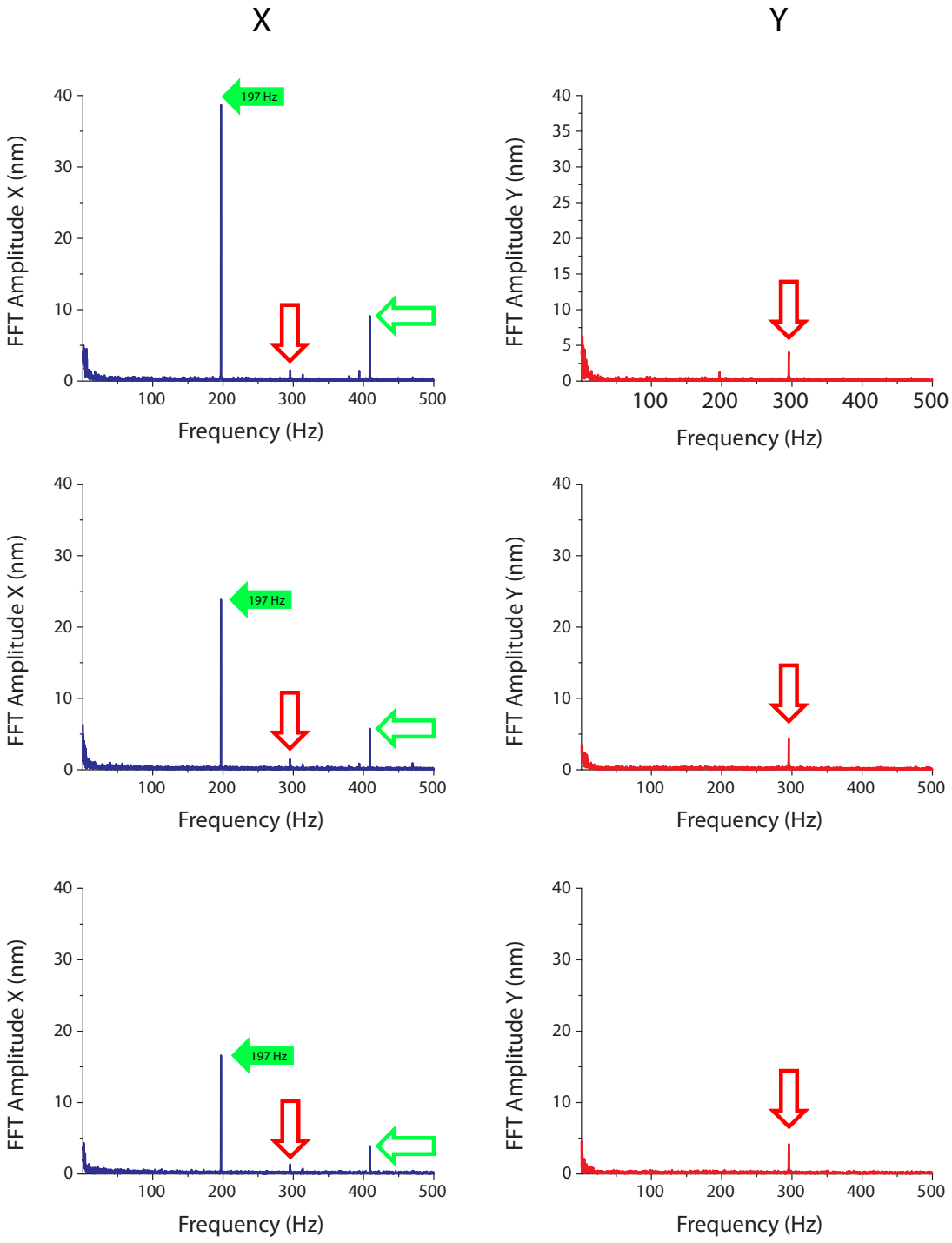

Figure 5.6 | Amplitude-frequency plots along the x and y directions corresponding three detecting positions along the *x-axis* $\approx 5,7$ and 10 µm away. Distance increases from top to bottom. The peak amplitude at 295.6 Hz has almost constant amplitude as the distance from the source increases while the other peak amplitudes decrease.

The amplitude dependence of the additional peaks as a function of the distance from the source is shown in Figure 5.6. Fortunately, all these additional contributions to the detector motion can be filtered out at the FFT step, resulting in a velocity map around an oscillator operating at 197 Hz.

5.2.2 Trap Stiffness k

To obtain the associated velocity field of the oscillatory flow, we calibrated the optical trap of the detector using the experimental setup in subsection 3.1.3. The calibration relies on the power spectrum fitting shown in Figure 5.7. A detailed description of the theory behind the method is given in subsection 2.3.1. The corresponding Matlab implementation, which we employed for our studies, is provided in reference [91].

The corner frequency f_c and the trap stiffness are related by:

$$f_c \equiv \frac{k}{2\pi\gamma_0}, \text{ and } \gamma_0 = 6\pi\rho\nu a, \tag{5.9}$$

where ρ is the density of water and ν its kinematic viscosity. For the x and y direction, respectively, the corner frequencies are $f_c^x = (603.6 \pm 7.9)$ Hz and $f_c^y = (532.3 \pm 6.7)$ Hz. These values and their error bars are the result of 20 measurements and yield trap stiffnesses along the corresponding directions of $k_x = (6.73 \pm 0.25) \times 10^{-5}$ N/m and $k_y = (6.00 \pm 0.23) \times 10^{-5}$ N/m. The obtained values for k are consistent with the literature [155] and show, as expected [93], that the lateral optical force parallel to the laser polarization direction (along the x-axis) is about 10% greater than the lateral forces perpendicular to it.

5.2.3 Error Calculation

The error bars (along each direction) were calculated through the propagation of error. For each velocity component ($u_j = \frac{k_j A_j}{6\pi\eta a}$, with $j = x, y$), an upper limit for the error is calculated as:

$$\frac{\delta u_j}{u_j} = \left(\frac{\delta a}{a} + \frac{\delta k_j}{k_j} + \frac{\delta A_j}{A_j}\right) \tag{5.10}$$

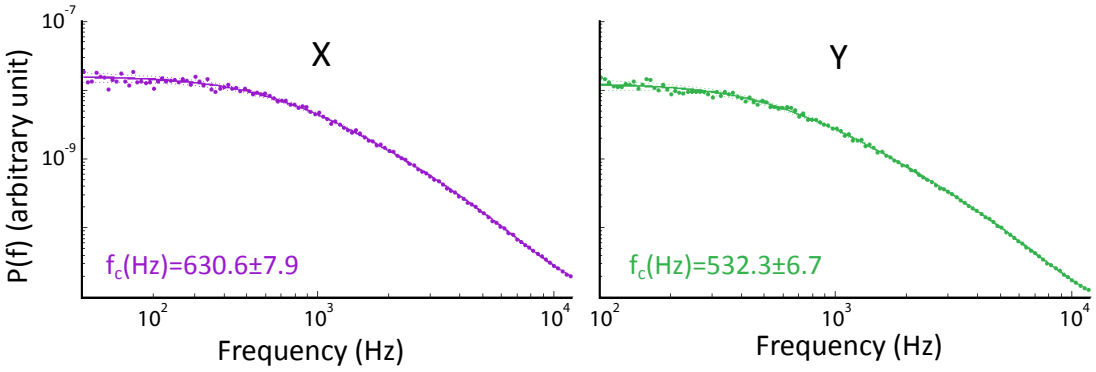

Figure 5.7 | Fitted power spectral densities of the detector bead motion without source. The fits provide the corner frequencies, f_c in x and y dimensions. The error bars of the obtained f_c values are obtained after 20 independent measurements.

with $a \pm \delta a = (0.88 \pm 0.02)\,\mu\text{m}$, $k_x = (6.73 \pm 0.25) \times 10^{-5}\text{N/m}$ and $k_y = (6.00 \pm 0.23) \times 10^{-5}\text{N/m}$ obtained from the size distribution and the calibration process, respectively. A maximum $\delta A_j \approx 3.5\%$ is obtained from statistics based on a control experiment consisting of 10 subsequent measurements each 10 s long for the detector amplitude measurement at a certain distance from the source.

5.3 Theoretical Modeling

For the frequencies ($< 100...200\,\text{Hz}$) and length scales (20 µm region of interest,$\lambda_{sound} \approx 7m$) considered here, the hydrodynamic near-field around a vibrating source is primarily governed by incompressible flow [156–158]. Simulations of the velocity field around an oscillating micro-sphere are performed by solving the Navier-Stokes equations for an incompressible fluid. In the simulations, we let a rigid sphere oscillate along the *x-axis* according to $x = A_s \sin(\omega t)$. Radius a of the sphere, amplitude A_s, and frequency f, are set to the experimental values, and the velocity of the liquid surrounding the bead, $\vec{u}$, is evaluated at the same 60 experimental points, as shown in Figure 5.2. The detector bead is not included in the simulations. Fluidic simulations are performed with the software COMSOL. The model considers a laminar flow and the Navier-Stokes equations for fluid motion are solved

$$\rho\frac{\partial\vec{u}}{\partial t}+\rho\left(\vec{u}\cdot\nabla\right)\vec{u}=\nabla\left[-\rho\hat{I}+\eta\left(\nabla\vec{u}+\left(\nabla\vec{u}\right)^{T}\right)\right] \tag{5.11}$$

with p the pressure, $\hat{I}$ the unity matrix and η and ρ the dynamic viscosity and density of water, respectively. In our two-dimensional axis-symmetric model, we consider a laminar flow and a moving mesh based on the arbitrary Lagrangian-Eulerian (ALE) application mode. The ALE mode enables the representation of free surface boundary with a domain boundary on the moving mesh. This allows for consideration of fluid structure interactions (viscous, pressure, and inertial fluid forces on the structure, even momentum transfer back to the fluid) and the accurate evaluation of surface properties such as curvature. To simulate the water droplet, the system is embedded in a simulation sphere of radius 1 mm. Imposing the corresponding no slip-boundary conditions, we evaluate the maximum velocity (when $\cos(\omega t) = 1$) exactly at the same positions where the detector bead was placed experimentally. The calculated fluidic field (in orange) is shown together with the experimental results (in black) in Figure 5.8. Maximum experimental deviations of the nominal parameters of the bead radius ($a = 0.90\,\mu$m) and source amplitude ($A = 411\,$nm) provide maximum variations of 2% in the simulated velocity fields. It should be noted that the velocity of two closely spaced beads is intrinsically different from single ones due to the influence of the flow field of one bead to the other. To account for that effect of ignoring the detecting bead in the simulations, we track the source and the detector bead in the experiment at the same time, attenuating the previous effect by looking at the amplitude of the source at each data point and normalizing the FFT detector amplitudes. It is also noted that the influence of the laser polarization along the x-axis has been included in the comparison as mentioned above. The comparison between numerical simulations and experiments in Figure 5.8 shows good agreement of the field pattern around the oscillating microsource when the detecting particle is located along the dipole axis (at $\theta \approx 0°$) and at intermediate positions far from the source (at $\theta < 90°$). At these positions, the revealed velocity field pattern resembles that of a dipole-type source in an incompressible flow. On the other hand, the magnitude of the measured signal is slightly larger than the numerical results at all positions. The largest differences between theory and experiments are found at the nearest points to the source ($\approx 5\,\mu$m) and at those positions perpendicular to the dipole axis (at

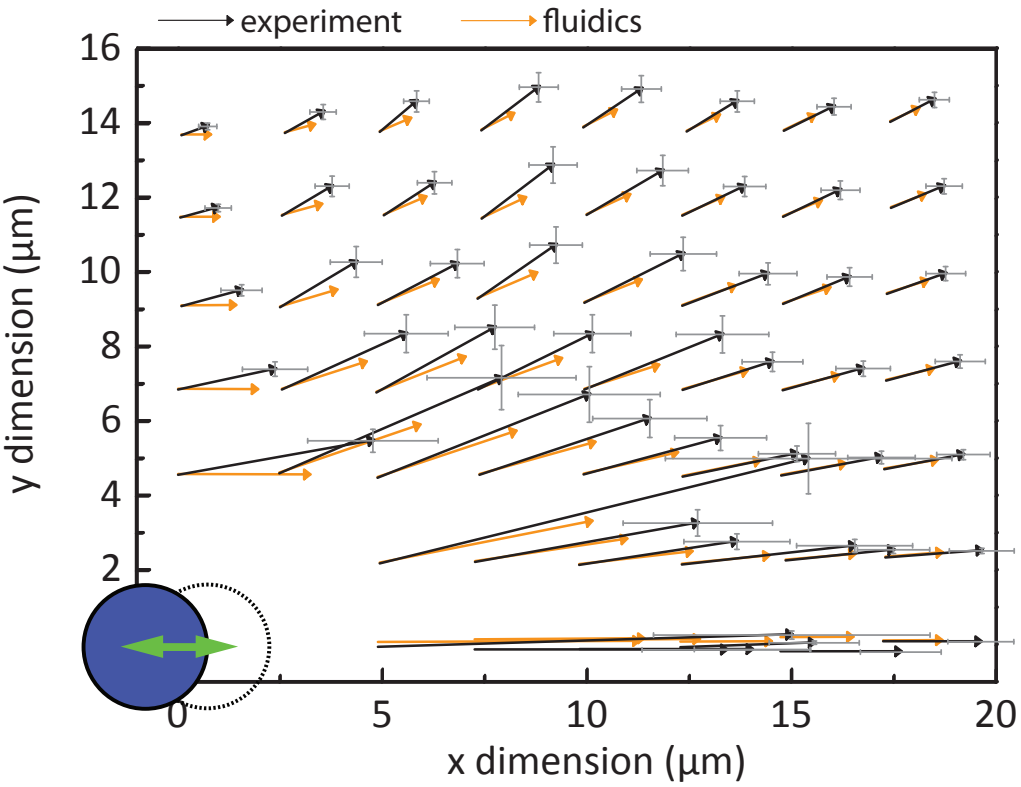

Figure 5.8 | Comparison between measured and modelled velocity map around a oscillating sphere. Black arrows display the direction and the magnitude of the velocity field measured experimentally. Orange arrows show the velocity filed around the source after solving Navier-Stokes equations. The arrows at the top of the figure represent scale bars of 40 µm/*s*. Error bars are shown in grey. Theoretical modelling done by Sol Carretero-Palacios.

$\theta \approx 90°$), where numerical results present strong signal parallel to the dipole axis but the experimental field points perpendicular to it. These differences may be attributed to the finite compressibility of water (sound) which is not included in the simulations. The addition of the velocity field of an acoustic dipole could compensate for the difference in magnitude and angles which are always smaller in the numerical simulations compared to experiment. Another source of the discrepancy found between simulations and experimental data is the fact that in our model the flow is assumed to be laminar, having a Stokes boundary layer that extends over the spatial region investigated here [159], therefore altering the oscillation of both the source and the detector beads.

5.4 Conclusion

In conclusion, we have demonstrated an optofluidic method to quantitatively map two-dimensional oscillating flows with microscale resolution. The vectorial velocity field around a micro-size silica particle in water and oscillating in a dipole mode is mapped by optically tracking a twin microparticle trapped in the vicinity. This experimental technique may serve as reference for understanding the fundamentals of oscillatory flows on this scale and frequency regimes, which is of great importance for mixing in microscale systems. The concept introduced in this Chapter opens the door to new methods for detecting, locating, and recognizing objects, such as cells, bacteria, and artificial micromachines, based on the velocity field pattern in their vicinity.

6 Summary and Outlook

In this dissertation, I presented two different studies of physics at the microscale, both based on the motion of a trapped particle.

First, in Chapter 4, I presented a sequence of experiments that demonstrate optical trapping of plasmonic Janus particles. Those experiments and the analysis of their results showed that: 1) plasmonic Janus particles can be optically trapped above the focal plane (the common trapping position) of optical tweezers, 2) the distance from that plane can be (i.e. the vertical position of the particle) controlled with the laser power showing an almost linear dependence, and 3) the trapped particles have a fixed orientation in the trap (gold part facing away from the beam). This power controlled vertical displacement of the particle was shown to be a result of a complex interplay between optical and thermal forces. The principles of this motion and the conditions for the observed stable trapping points were discussed. The potential energy landscape of the trapping beam was investigated, predicting a discontinuity in the linear power displacement relation. The investigated system shows that plasmonic Janus particles and gold nanoparticles can be simultaneously trapped, above and at the focal plane, respectively. Moreover, the distance between them, and more importantly the gold island film of the Janus particle and the gold nanoparticle can be controlled by changing the laser power. These findings lead to the following conclusions: the investigated system can find direct application in experiments where controllable spacing between trapped particles is needed. Apart from the experimental importance, the investigated system can serve to determinate the thermophoretic force which drives a plasmonic self-propeller to move. In contrast to previous studies, this force determination can be performed using only fixed 1-dimensional motion with the corresponding uniform illumination. This system works in much simpler conditions than what has been presented to date. Despite the huge interest, the determination of thermophoretic forces of microscale self-

propellers has only been achieved for very simple systems (not involving light driven self-propeller)[101, 102, 114]. Observing the vertical motion of the particle in an optical trap with time resolution of 1 ms or better, could give the acceleration of the particle right after the laser power increased. As described in Chapter 4 the counteracting optical force should in this case be insignificant with respect to the driving thermal force. Knowing the frictional force, the thermal force could be obtained from Newton's second law.

The second part of this dissertation introduces an optofluidic method that allows the 2-dimensional vectorial near-field mapping of oscillatory flows with microscale resolution. In the presented proof-of-principle experiment, the velocity around a dipolar oscillator was determined at 60 positions in space. The obtained data showed good agreement with the theoretical predictions. The method, presented in Chapter 5, can find direct applications in the design and exploration of microfluidic mixing devices and can be used as a tool for mechanical spectroscopy of oscillatory flows. There is no limit to the number of sources that can be used, the sensitivity of a single source is limited only by the precision of position determination of the trapped particle and can be overcome with trapping larger beads. Considering multiple detector particles, the introduced method allows for location of unknown micrometer sources (with nanometer amplitudes of oscillation) of oscillatory fluid motion by the means of triangulation. Thus, the method provides a basis for a microfluidic microscope.

Appendix A: Microfluidic Data

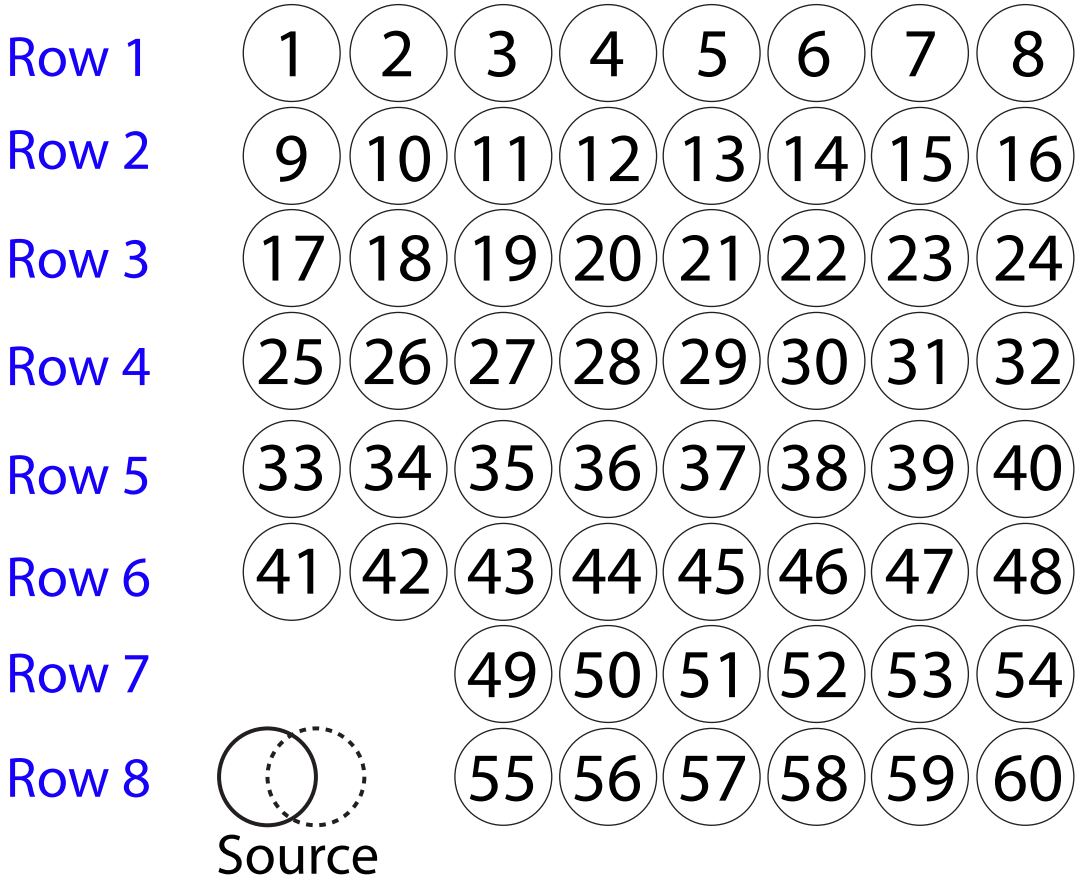

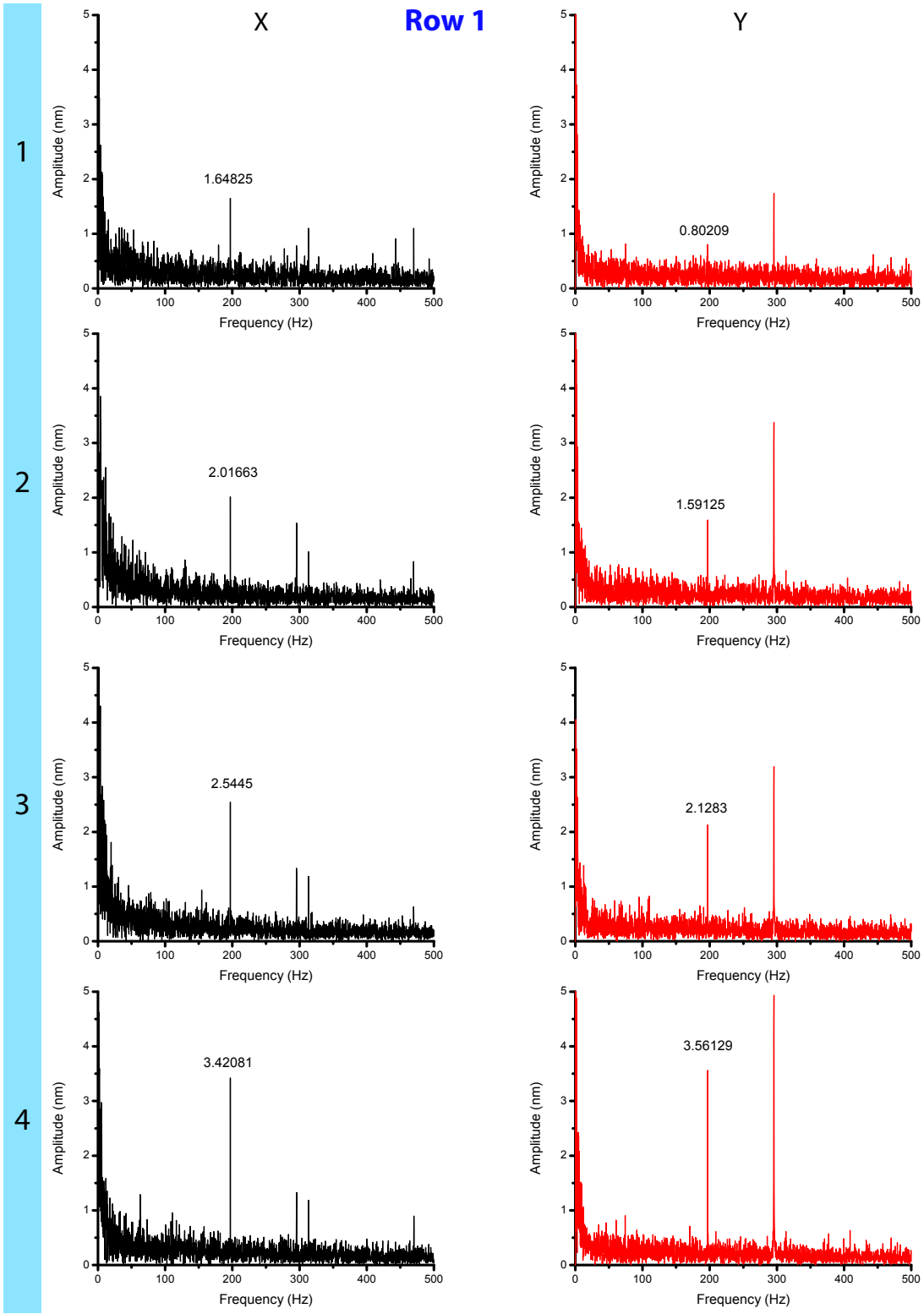
X
Row 1
Y
1
2
3
4
Amplitude (nm)
Frequency (Hz)
1.64825
0.80209
2.01663
1.59125
2.5445
2.1283
3.42081
3.56129

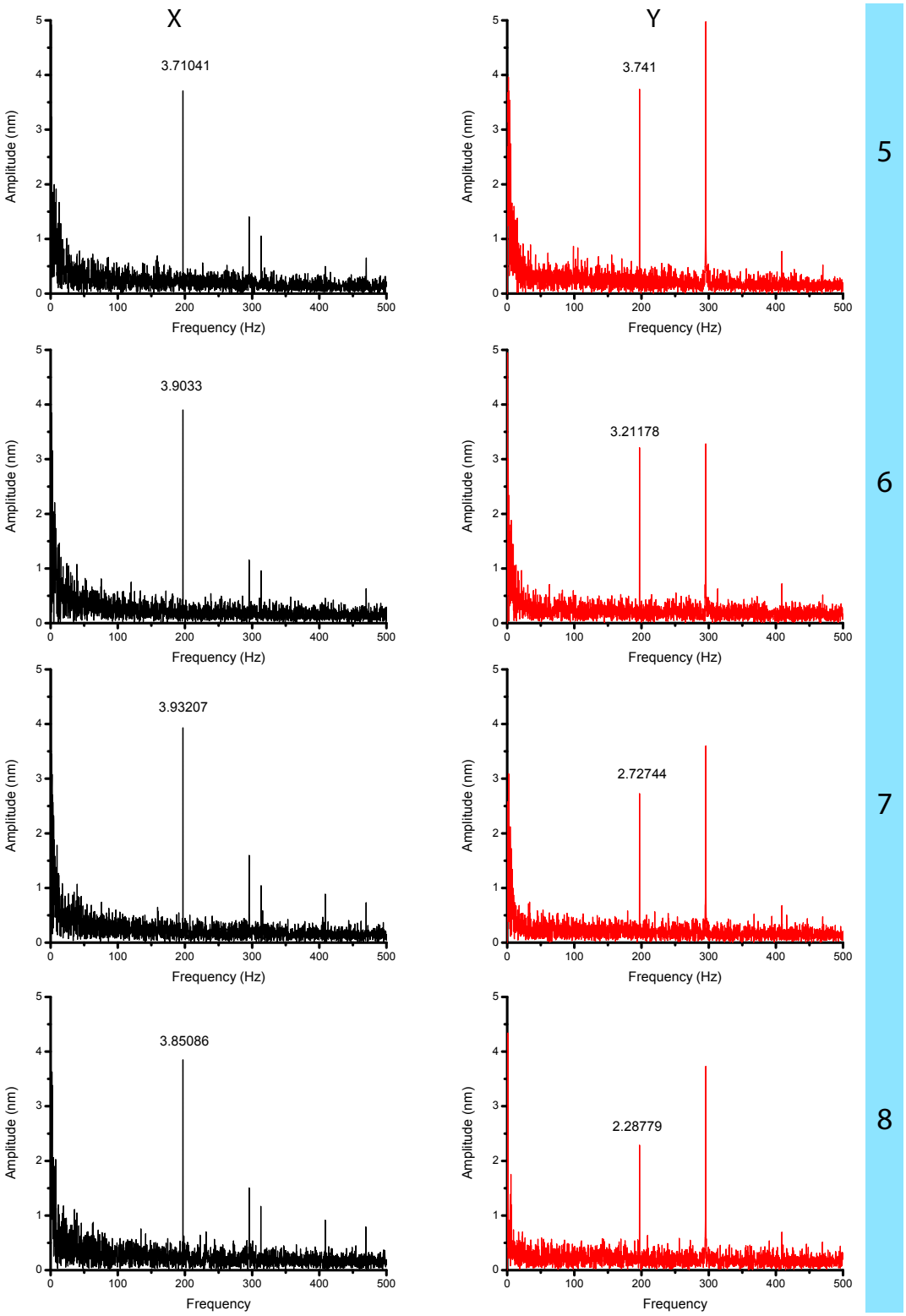
X
Y
3.71041
3.741
3.9033
3.21178
3.93207
2.72744
3.85086
2.28779
Amplitude (nm)
Frequency (Hz)
Frequency
5
6
7
8

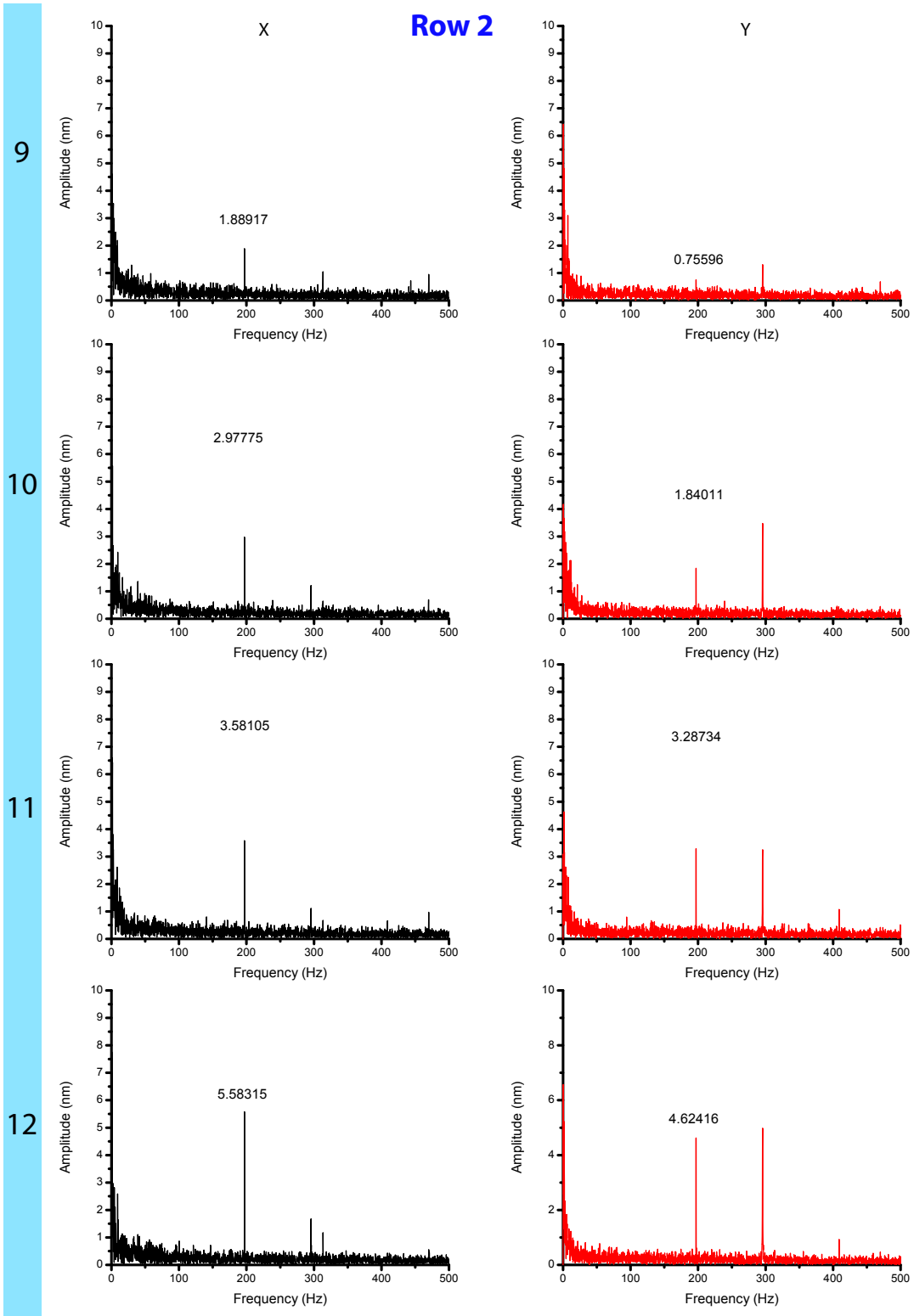
Row 2
X
Y
9
10
11
12
Amplitude (nm)
Frequency (Hz)
1.88917
0.75596
2.97775
1.84011
3.58105
3.28734
5.58315
4.62416

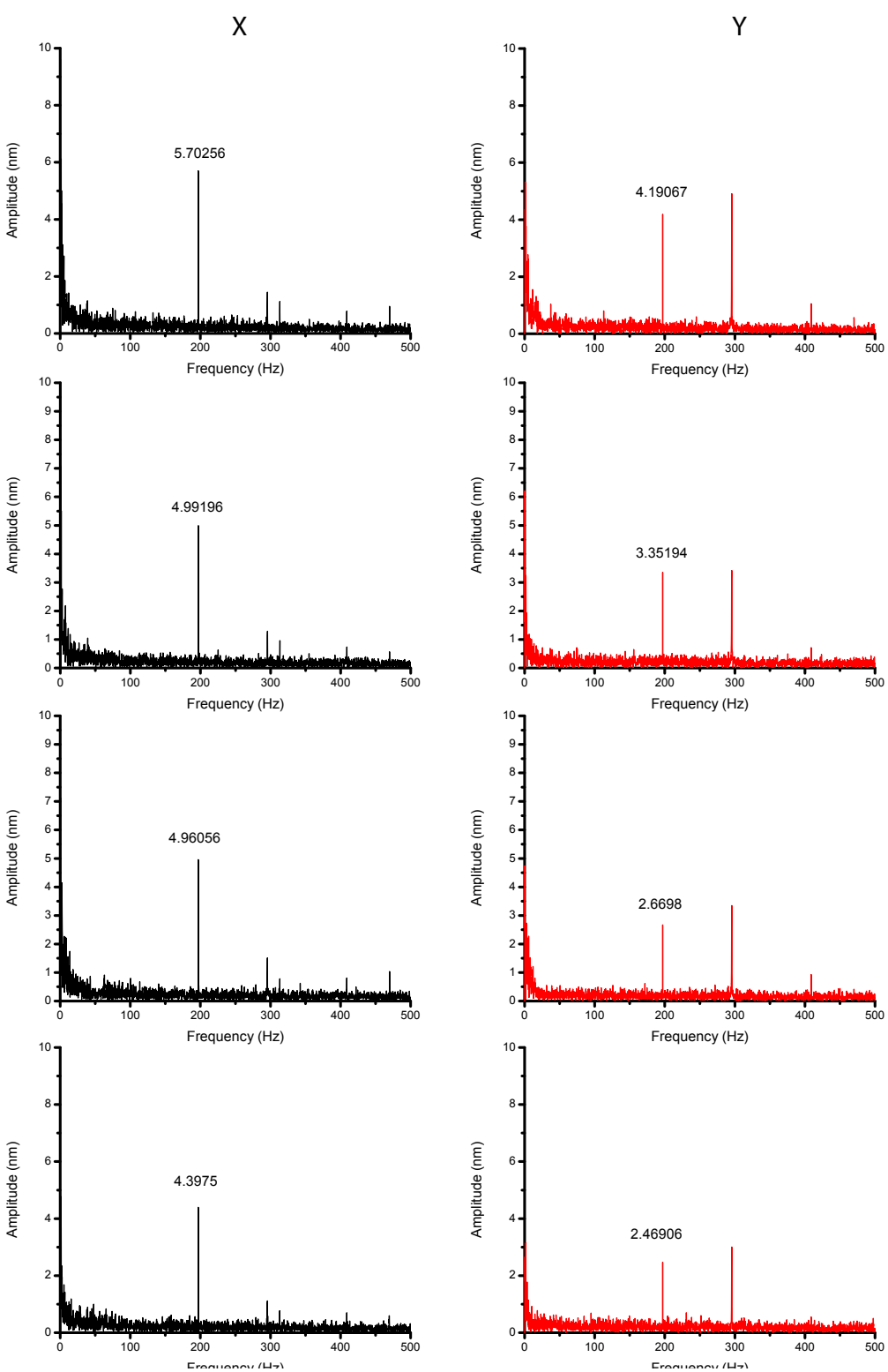
X
Y
Amplitude (nm)
Frequency (Hz)
5.70256
4.19067
4.99196
3.35194
4.96056
2.6698
4.3975
2.46906
13
14
15
16

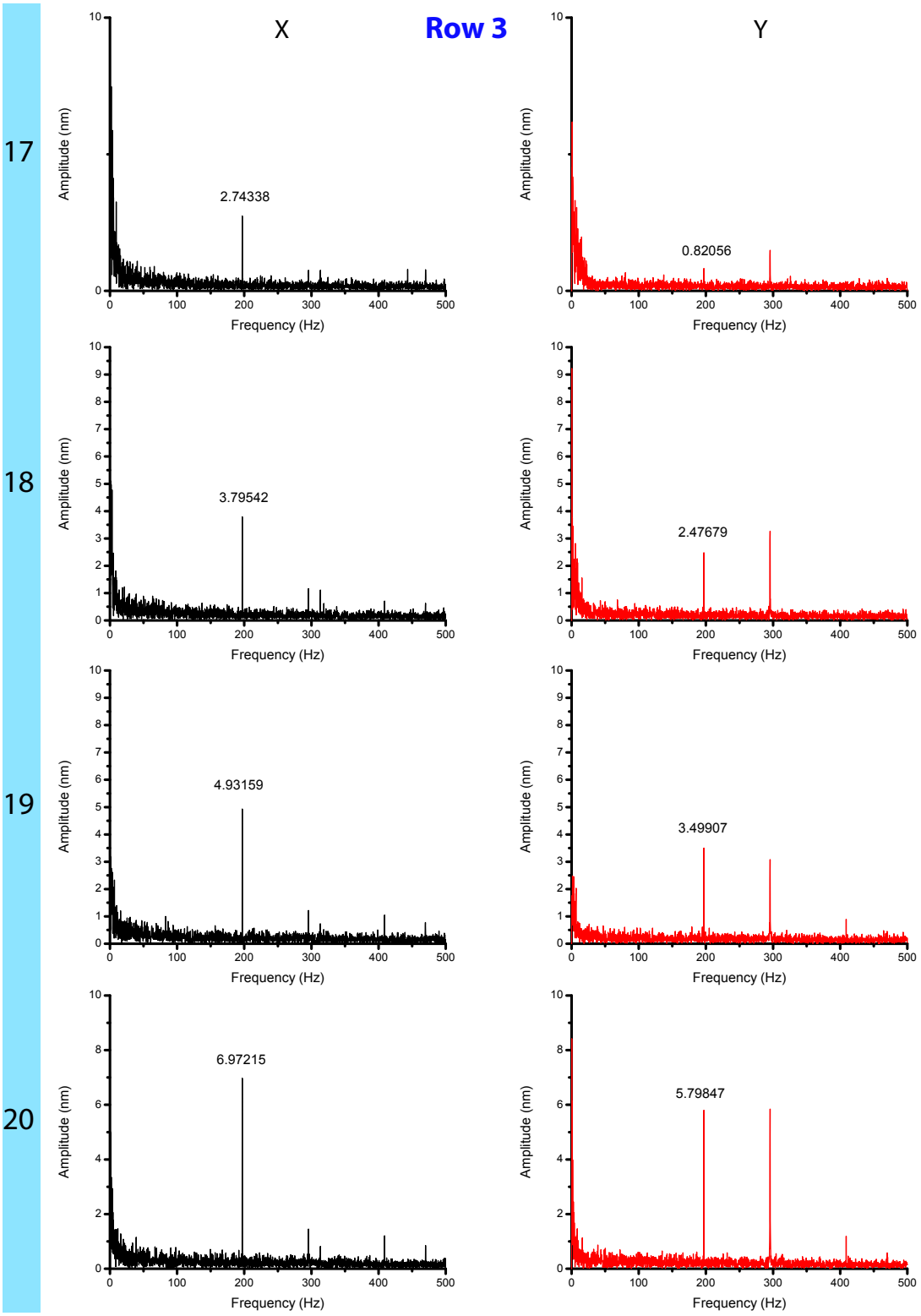
Row 3
X
Y
17
18
19
20
Amplitude (nm)
Frequency (Hz)
2.74338
0.82056
3.79542
2.47679
4.93159
3.49907
6.97215
5.79847

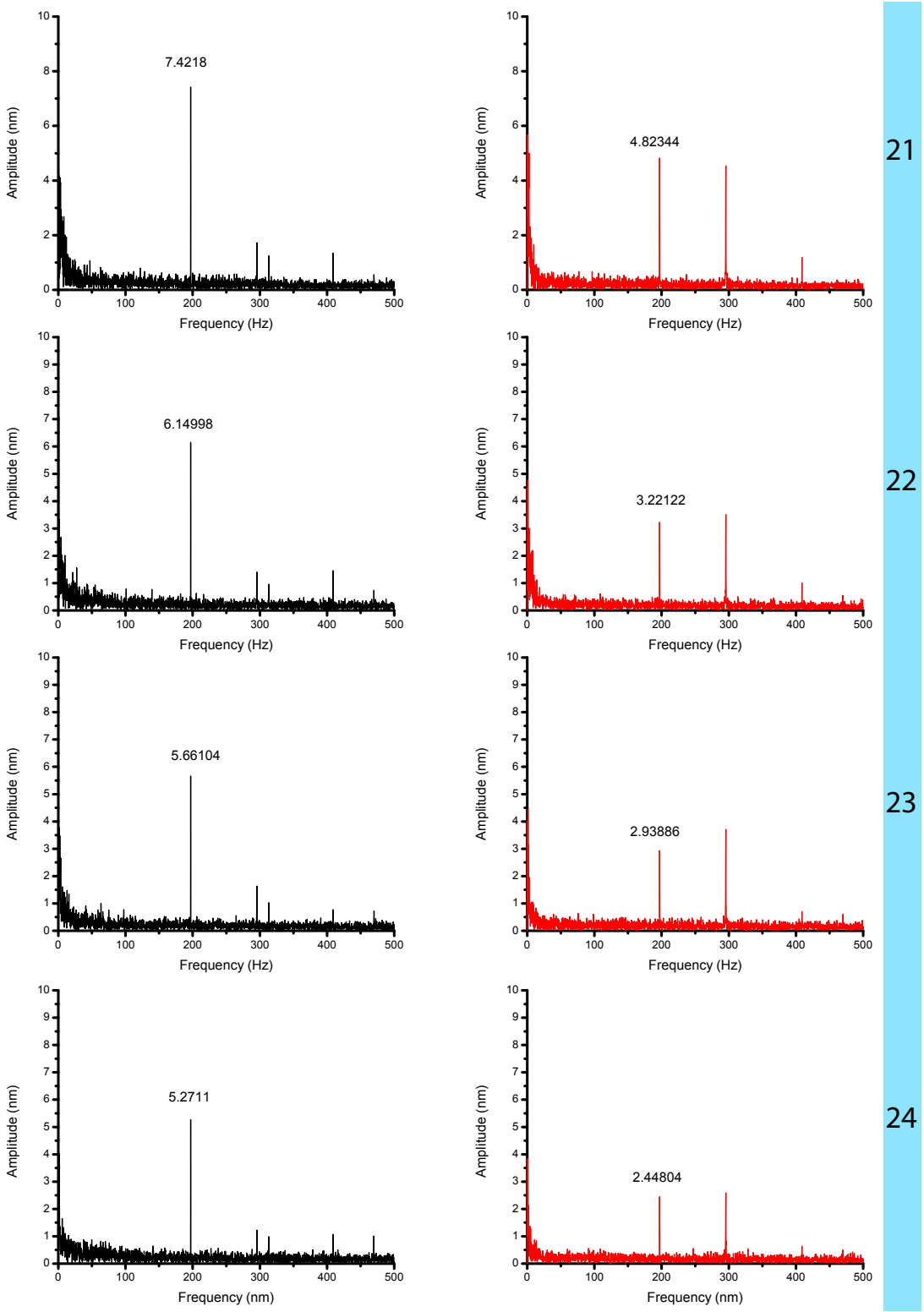
7.4218
Amplitude (nm)
Frequency (Hz)
4.82344
Amplitude (nm)
Frequency (Hz)
21
6.14998
Amplitude (nm)
Frequency (Hz)
3.22122
Amplitude (nm)
Frequency (Hz)
22
5.66104
Amplitude (nm)
Frequency (Hz)
2.93886
Amplitude (nm)
Frequency (Hz)
23
5.2711
Amplitude (nm)
Frequency (nm)
2.44804
Amplitude (nm)
Frequency (nm)
24

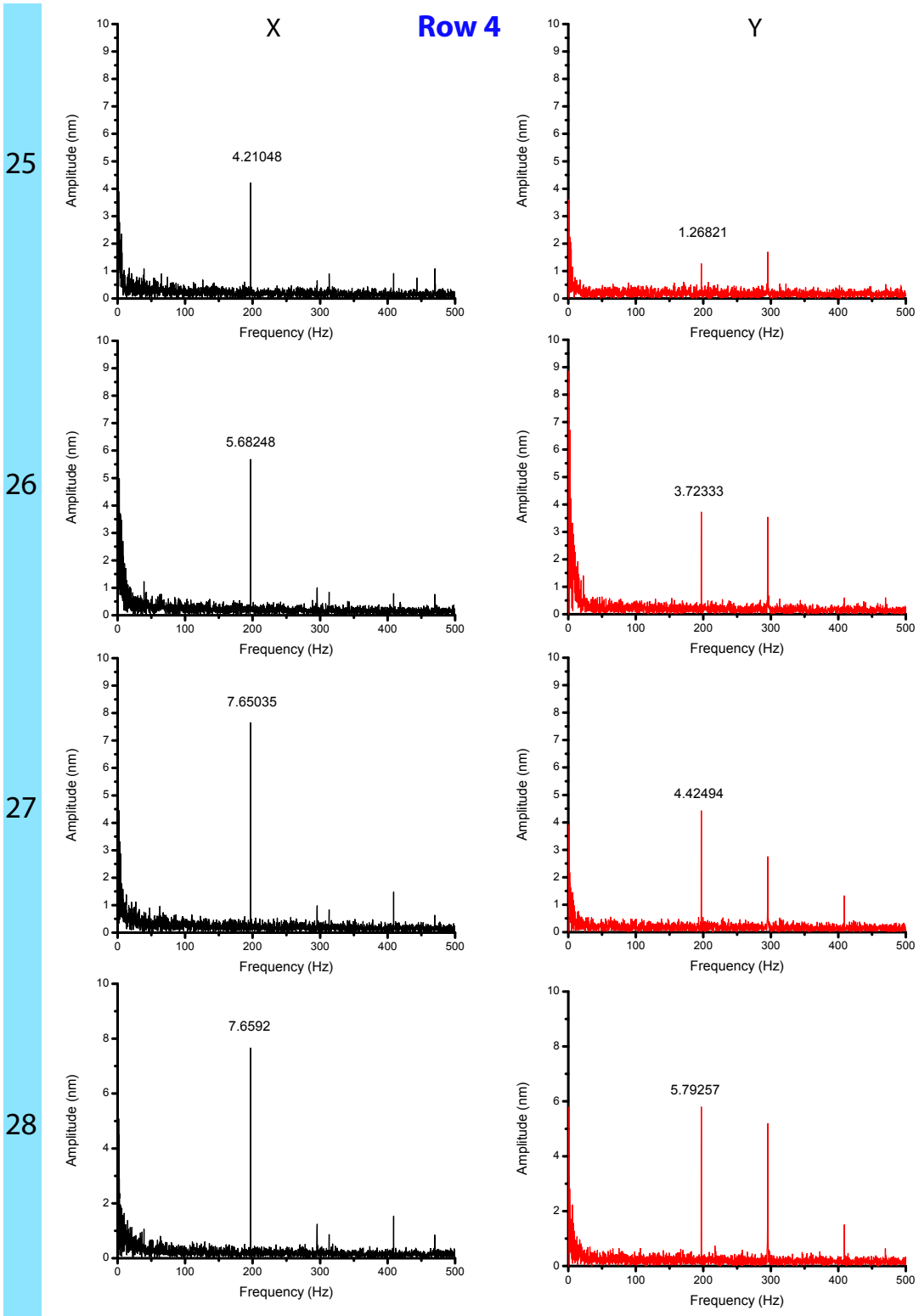
Row 4
X
Y
25
26
27
28
Amplitude (nm)
Frequency (Hz)
4.21048
1.26821
5.68248
3.72333
7.65035
4.42494
7.6592
5.79257

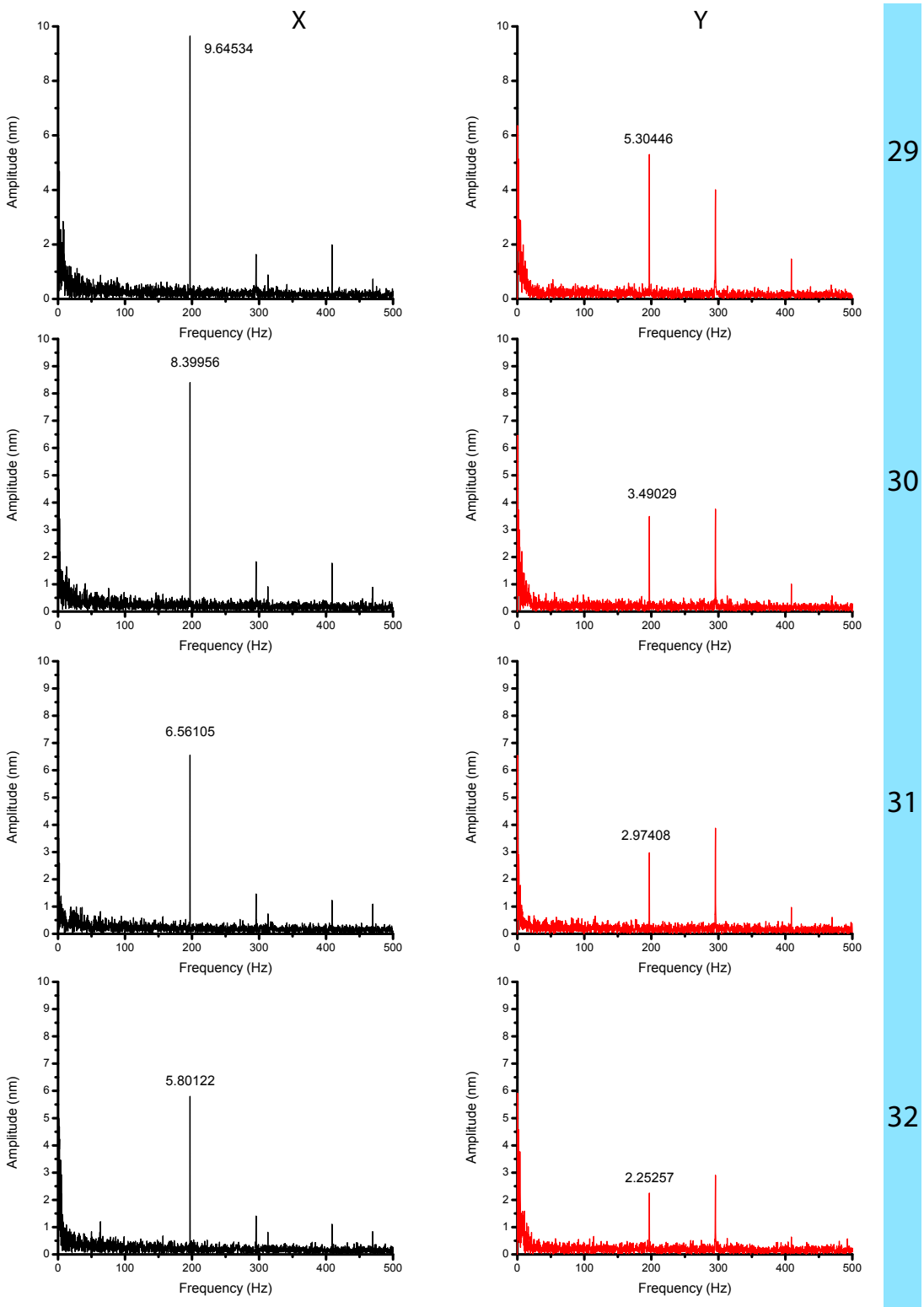
X
Y
9.64534
5.30446
8.39956
3.49029
6.56105
2.97408
5.80122
2.25257
Amplitude (nm)
Frequency (Hz)
29
30
31
32

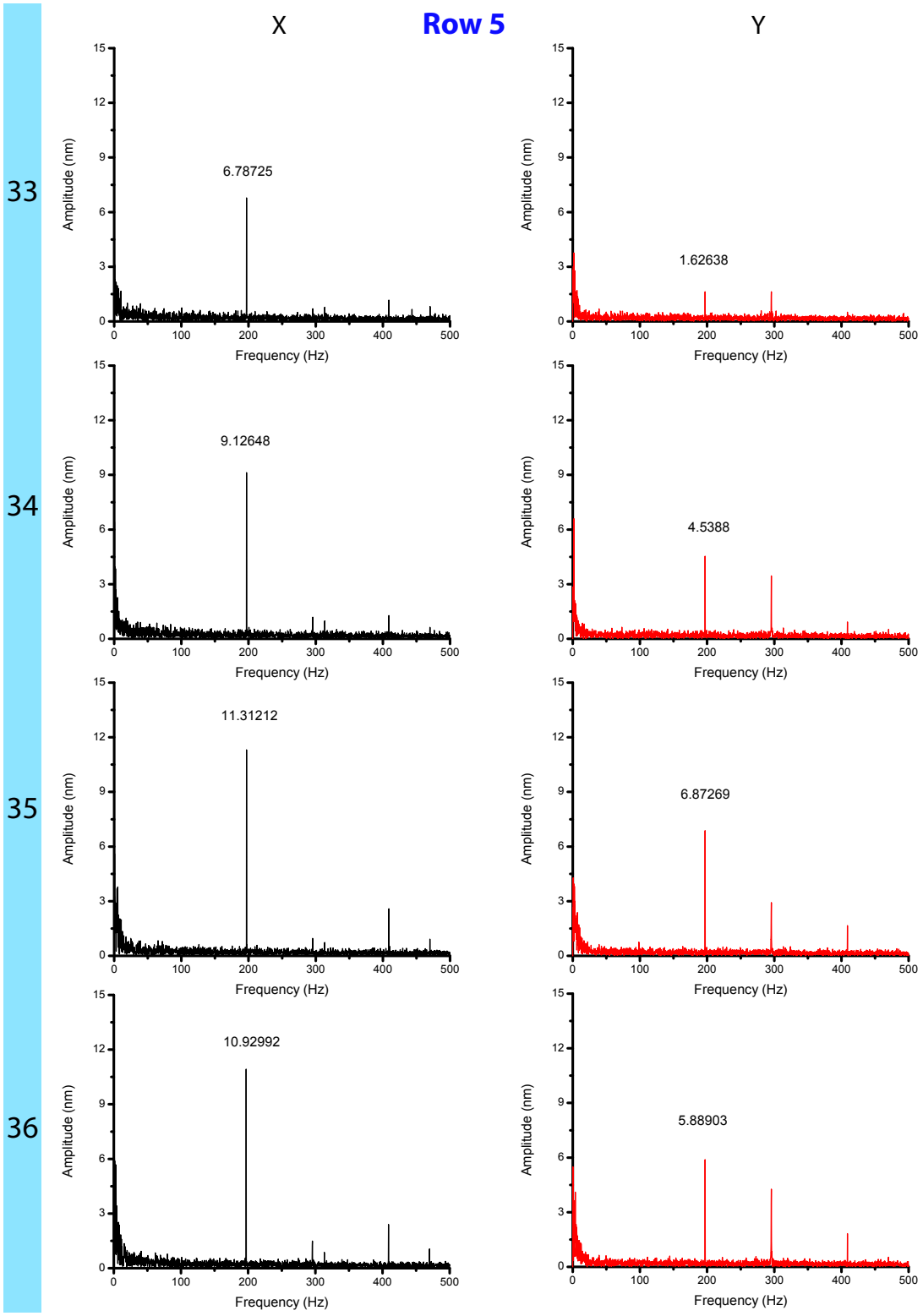
Row 5
X
Y
33
34
35
36
Amplitude (nm)
Frequency (Hz)
6.78725
1.62638
9.12648
4.5388
11.31212
6.87269
10.92992
5.88903

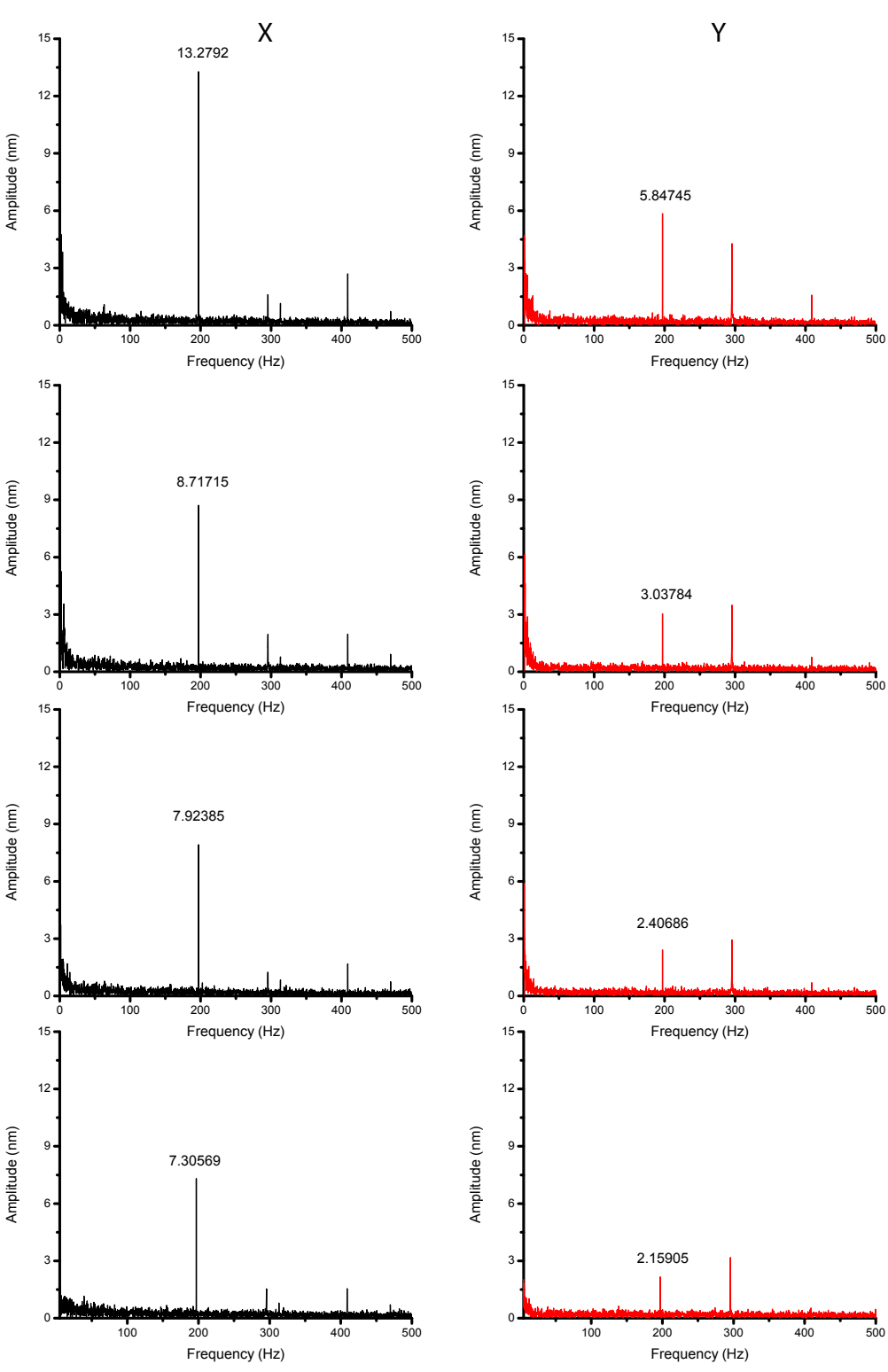
X
Y
13.2792
5.84745
8.71715
3.03784
7.92385
2.40686
7.30569
2.15905
Amplitude (nm)
Frequency (Hz)
37
38
39
40

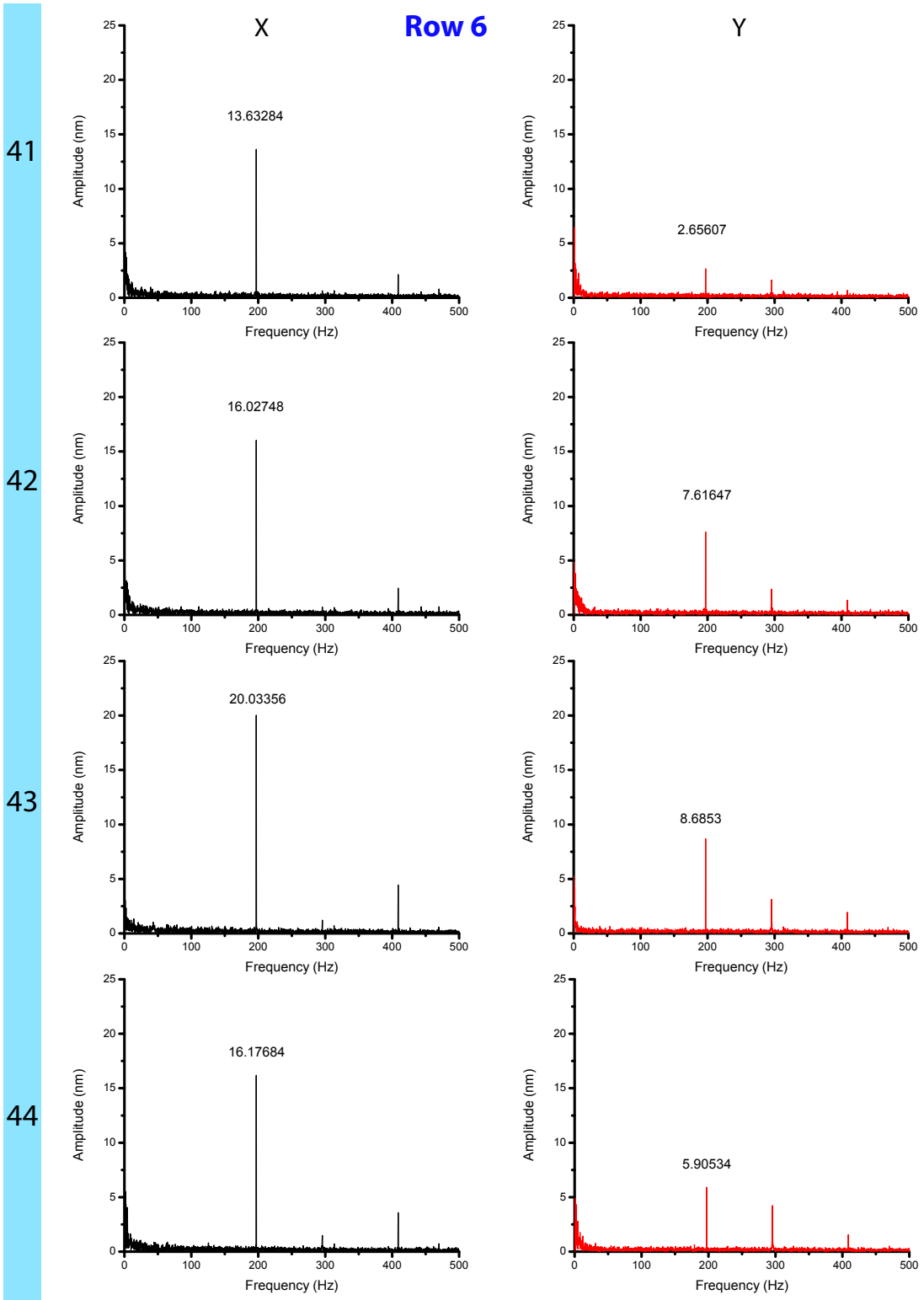
Row 6
X
Y
41
42
43
44
13.63284
2.65607
16.02748
7.61647
20.03356
8.6853
16.17684
5.90534
Amplitude (nm)
Frequency (Hz)
0
5
10
15
20
25
0
100
200
300
400
500

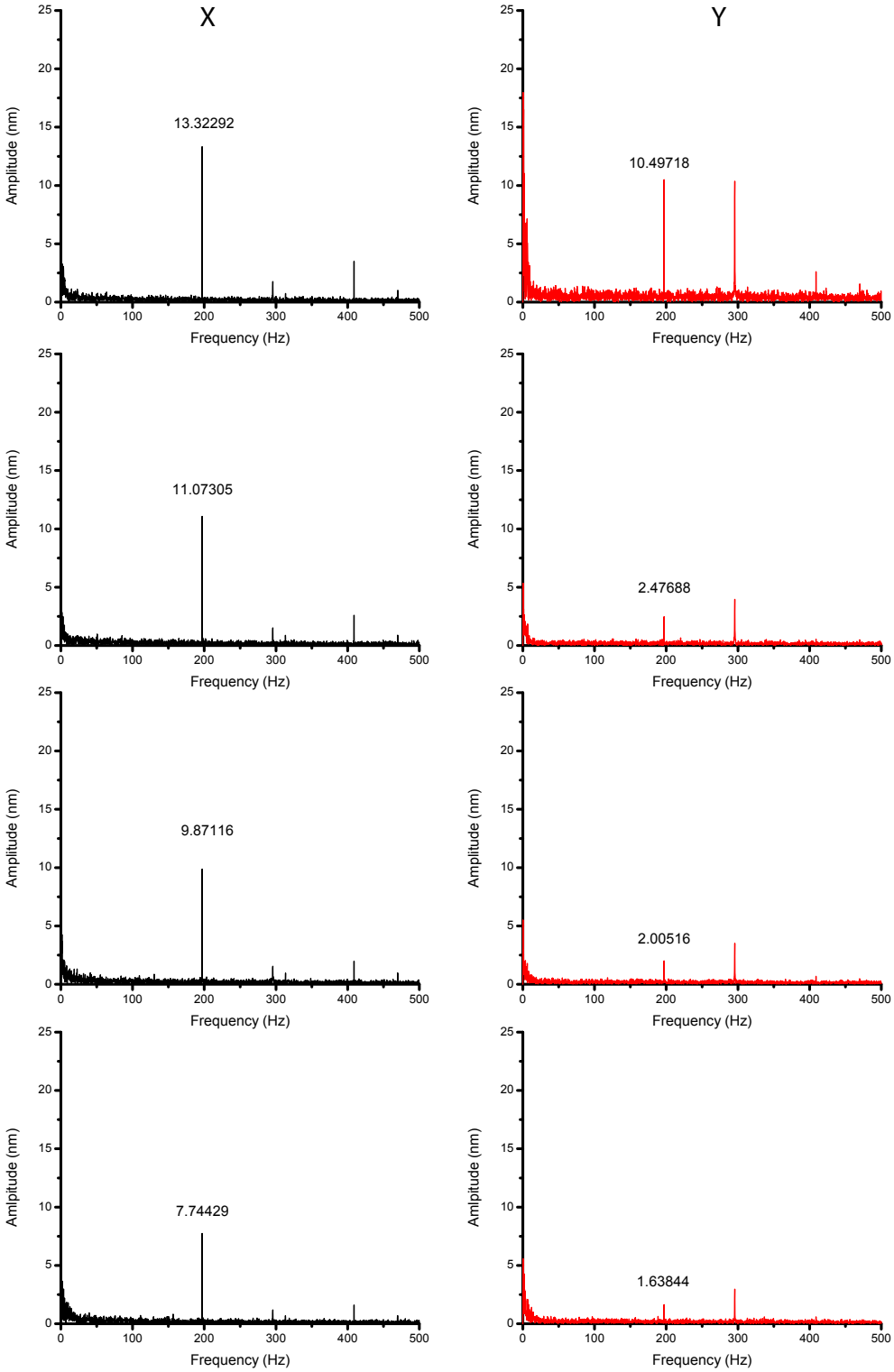
X
Y
13.32292
10.49718
11.07305
2.47688
9.87116
2.00516
7.74429
1.63844
Amplitude (nm)
Frequency (Hz)
45
46
47
48

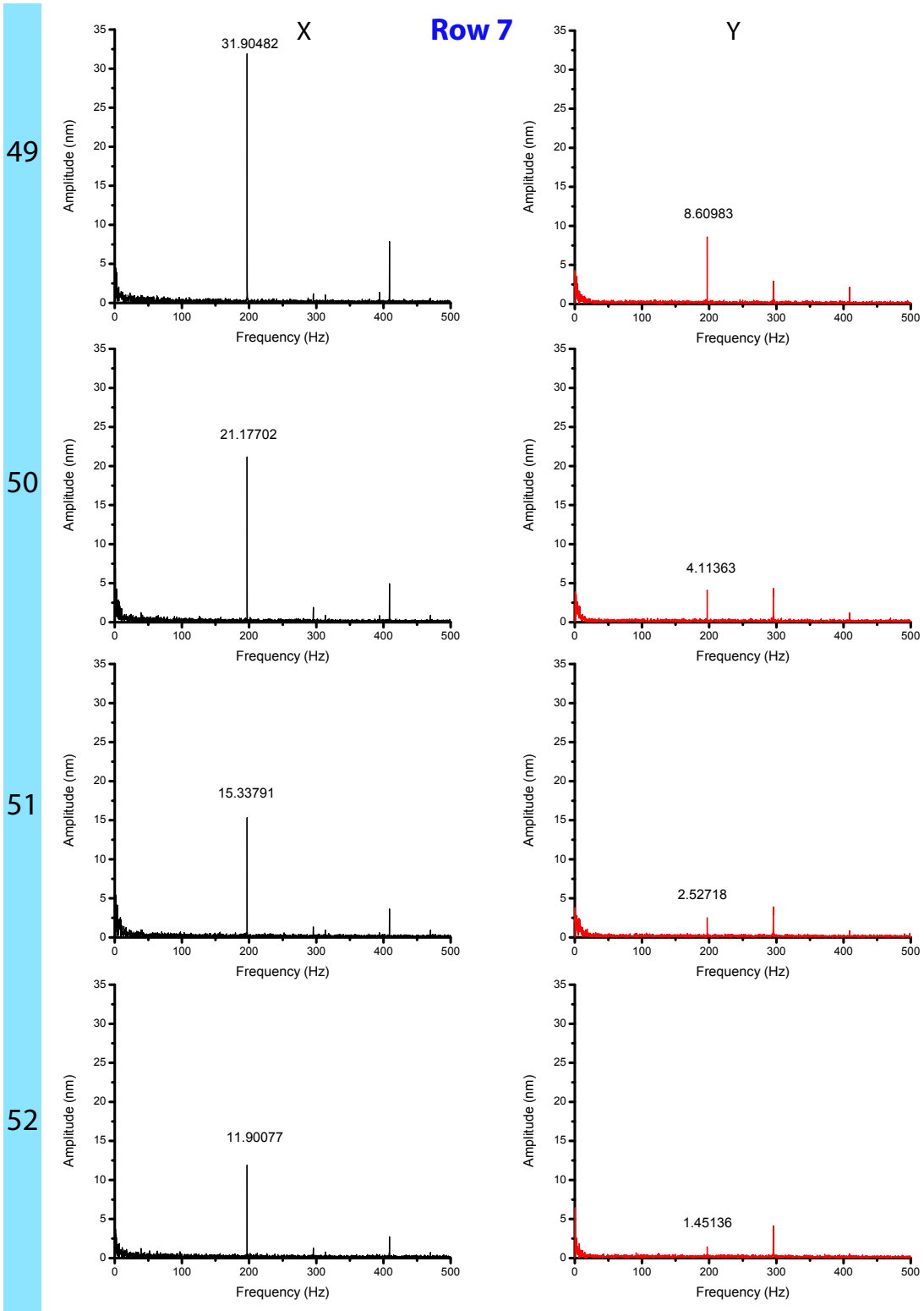
Row 7
X
Y
49
50
51
52
31.90482
8.60983
21.17702
4.11363
15.33791
2.52718
11.90077
1.45136
Amplitude (nm)
Frequency (Hz)

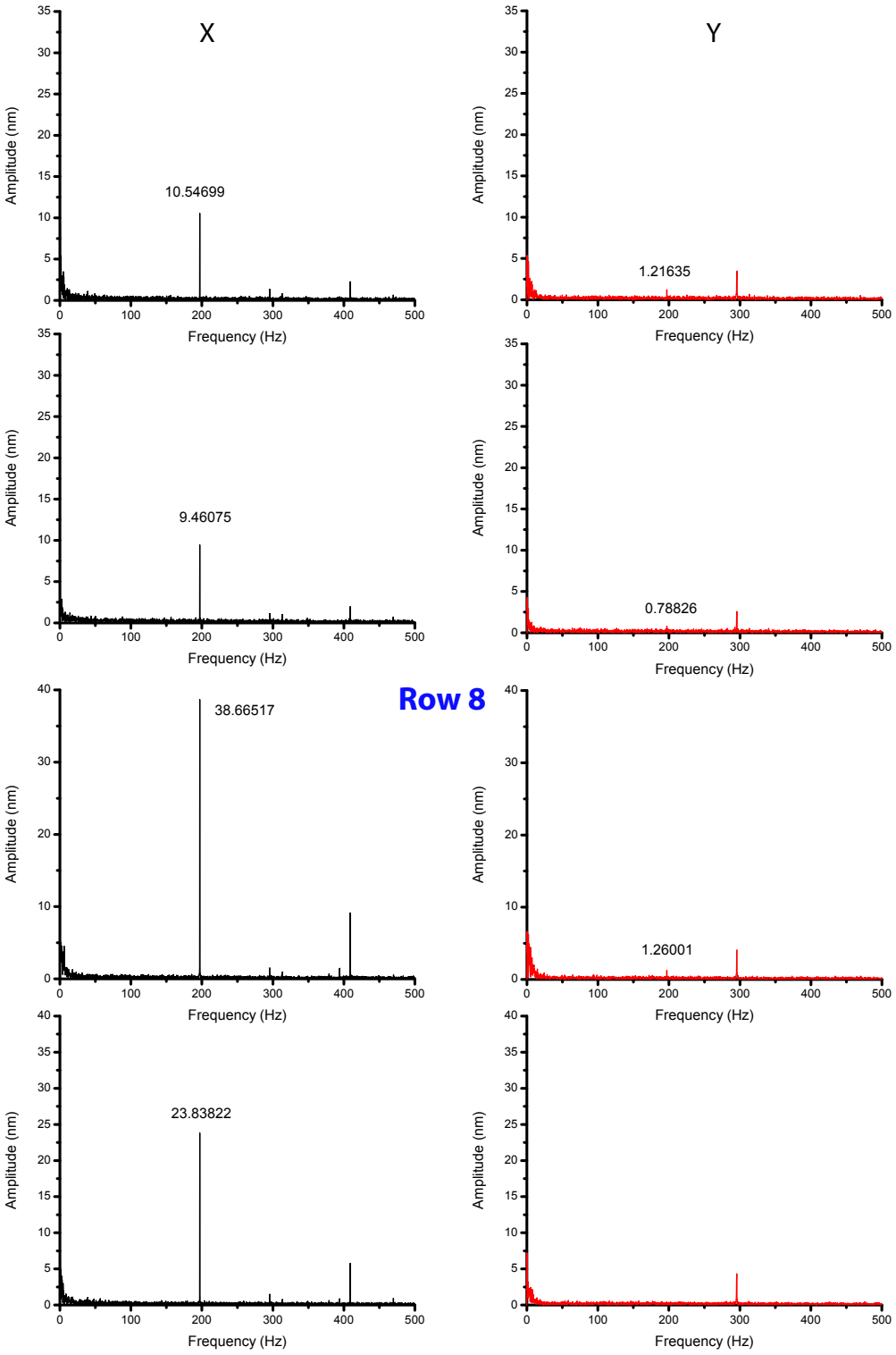
X
Y
Amplitude (nm)
Frequency (Hz)
10.54699
1.21635
9.46075
0.78826
Row 8
38.66517
1.26001
23.83822
53
54
55
56

57

58

59

60

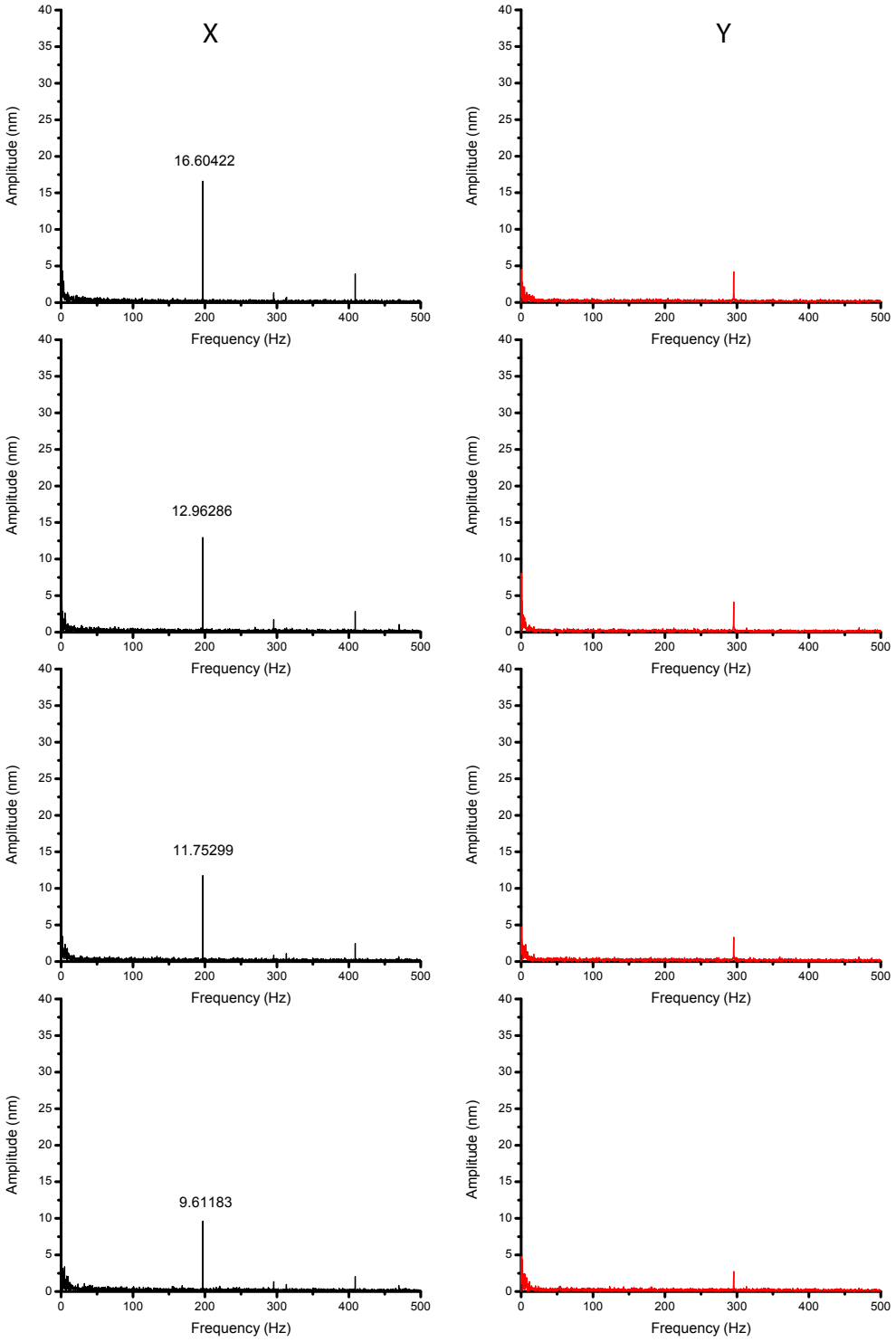
X
Y
16.60422
12.96286
11.75299
9.61183
Amplitude (nm)
Frequency (Hz)

References

[1] J. Kepler. *De cometis libelli tres*. Augustae Vindelicorum, 1619. [cited on pp. 1,6]

[2] K. Svoboda and S. M. Block. Optical trapping of metallic rayleigh particles. *Opt. Lett.*, 19(13): 930–932, Jul 1994. doi: 10.1364/OL.19.000930. URL http://ol.osa.org/abstract.cfm?URI=ol-19-13-930. [cited on p. 1]

[3] P. C. Ke and M. Gu. Characterization of trapping force on metallic mie particles. *Appl. Opt.*, 38(1):160–167, Jan 1999. doi: 10.1364/AO.38.000160. URL http://ao.osa.org/abstract.cfm?URI=ao-38-1-160. [cited on p. 1]

[4] L. P. Ghislain, N. A. Switz, and W. W. Webb. Measurement of small forces using an optical trap. *Review of Scientific Instruments*, 65(9):2762–2768, September 1994. ISSN 0034-6748, 1089-7623. doi: 10.1063/1.1144613. URL http://scitation.aip.org/content/aip/journal/rsi/65/9/10.1063/1.1144613. [cited on pp. 1,17]

[5] R. I. Litvinov, H. Shuman, J. S. Bennett, and J. W. Weisel. Binding strength and activation state of single fibrinogen-integrin pairs on living cells. *Proceedings of the National Academy of Sciences of the United States of America*, 99(11):7426–7431, May 2002. ISSN 0027-8424. doi: 10.1073/pnas.112194999. URL http://www.ncbi.nlm.nih.gov/pmc/articles/PMC124247/. [cited on pp.]

[6] A. Rohrbach and E. H. K. Stelzer. Trapping forces, force constants, and potential depths for dielectric spheres in the presence of spherical aberrations. *Applied Optics*, 41(13):2494–2507, May 2002. doi: 10.1364/AO.41.002494. URL http://ao.osa.org/abstract.cfm?URI=ao-41-13-2494. [cited on pp. 1,17]

[7] F. Gittes and C. F. Schmidt. Chapter 8 signals and noise in micromechanical measurements. In Michael P. Sheetz, editor, *Methods in Cell Biology*, volume 55, pages 129–156. Academic Press, 1997. URL http://www.sciencedirect.com/science/article/pii/S0091679X08604069. [cited on pp. 1,21]

[8] F. Gittes and C. F. Schmidt. Interference model for back-focal-plane displacement detection in optical tweezers. *Opt. Lett.*, 23(1):7–9, Jan 1998. doi: 10.1364/OL.23.000007. URL http://ol.osa.org/abstract.cfm?URI=ol-23-1-7. [cited on p. 19]

[9] A. Pralle, M. Prummer, E.-L. Florin, E.H.K. Stelzer, and J.K.H. HÃ¶rber. Three-dimensional high-resolution particle tracking for optical tweezers by forward scattered light. *Microscopy Research and Technique*, 44(5):378–386, 1999. ISSN 1097-0029. doi: 10.1002/(SICI)1097-0029(19990301)44:5<378::AID-JEMT10>3.0.CO;2-Z. URL http://dx.doi.org/10.1002/(SICI)1097-0029(19990301)44:5<378::AID-JEMT10>3.0.CO;2-Z. [cited on p. 19]

[10] D. G. Grier. A revolution in optical manipulation. *Nature*, 424(6950):810–816, August 2003. ISSN 0028-0836. doi: 10.1038/nature01935. URL http://www.nature.com/nature/journal/v424/n6950/full/nature01935.html. [cited on pp. 1,7]

[11] A. S. Urban, S. Carretero-Palacios, A. A. Lutich, T. Lohmuller, J. Feldmann, and F. Jackel. Optical trapping and manipulation of plasmonic nanoparticles: fundamentals, applications, and perspectives. *Nanoscale*, 6:4458–4474, 2014. doi: 10.1039/C3NR06617G. URL http://dx.doi.org/10.1039/C3NR06617G. [cited on p. 7]

[12] A. Lehmuskero, P. Johansson, H. Rubinsztein-Dunlop, L. Tong, and M. Käll. Laser trapping of colloidal metal nanoparticles. *ACS Nano*, 9(4):3453–3469, 2015. doi: 10.1021/acsnano.5b00286. URL http://dx.doi.org/10.1021/acsnano.5b00286. PMID: 25808609. [cited on p. 1]

[13] S. J. Ebbens and J. R. Howse. In pursuit of propulsion at the nanoscale. *Soft Matter*, 6:726–738, 2010. doi: 10.1039/B918598D. URL http://dx.doi.org/10.1039/B918598D. [cited on p. 1]

[14] B. J. Nelson, I. K. Kaliakatsos, and J. J. Abbott. Microrobots for minimally invasive medicine. *Annual Review of Biomedical Engineering*, 12(1):55–85, 2010. doi: 10.1146/annurev-bioeng-010510-103409. URL http://dx.doi.org/10.1146/annurev-bioeng-010510-103409. PMID: 20415589. [cited on pp.]

[15] K. E. Peyer, L. Zhang, and B. J. Nelson. Bio-inspired magnetic swimming microrobots for biomedical applications. *Nanoscale*, 5:1259–1272, 2013. doi: 10.1039/C2NR32554C. URL http://dx.doi.org/10.1039/C2NR32554C. [cited on p. 1]

[16] M. Leoni, J. Kotar, B. Bassetti, P. Cicuta, and M. Cosentino Lagomarsino. A basic swimmer at low reynolds number. *Soft Matter*, 5:472–476, 2009. doi: 10.1039/B812393D. URL http://dx.doi.org/10.1039/B812393D. [cited on p. 1]

[17] E. M. Purcell. Life at low reynolds number. *Am. J. Phys*, 45(1):3–11, 1977. [cited on pp.]

[18] A. Snezhko, M. Belkin, I. S. Aranson, and W.-K. Kwok. Self-assembled magnetic surface swimmers. *Phys. Rev. Lett.*, 102:118103, Mar 2009. doi: 10.1103/PhysRevLett.102.118103. URL http://link.aps.org/doi/10.1103/PhysRevLett.102.118103. [cited on pp.]

[19] B. J. Williams, S. V. Anand, J. Rajagopalan, and M. T. A. Saif. A self-propelled biohybrid swimmer at low reynolds number. *Nat Commun*, 5, January 2014. URL http://dx.doi.org/10.1038/ncomms4081. [cited on p. 1]

[20] A. Walther and A. H. E. Müller. Janus Particles: Synthesis, Self-Assembly, Physical Properties, and Applications. *Chemical Reviews*, 113(7):5194–5261, July 2013. ISSN 0009-2665. doi: 10.1021/cr300089t. URL http://dx.doi.org/10.1021/cr300089t. [cited on p. 1]

[21] H.-R. Jiang, N. Yoshinaga, and M. Sano. Active motion of a janus particle by self-thermophoresis in a defocused laser beam. *Phys. Rev. Lett.*, 105:268302, Dec 2010. doi: 10.1103/PhysRevLett.105.268302. URL http://link.aps.org/doi/10.1103/PhysRevLett.105.268302. [cited on pp. 1,29]

[22] K. C. Neuman and S. M. Block. Optical trapping. *Review of Scientific Instruments*, 75(9):2787–2809, 2004. doi: http://dx.doi.org/10.1063/1.1785844. URL http://scitation.aip.org/content/aip/journal/rsi/75/9/10.1063/1.1785844. [cited on pp. 2, 7,46]

[23] F. S. Merkt, A. Erbe, and P. Leiderer. Capped colloids as light-mills in optical traps. *New Journal of Physics*, 8(9):216, September 2006. ISSN 1367-2630. doi: 10.1088/1367-2630/8/9/216. URL http://iopscience.iop.org/1367-2630/8/9/216. [cited on pp. 2,46]

[24] C.-D Huang, D.-Y. Kang, and C.-C. Hsieh. Simulations of dna stretching by flow field in microchannels with complex geometry. *Biomicrofluidics*, 8(1):014106, 2014. doi: http://dx.doi.org/10.1063/1.4863802. URL http://scitation.aip.org/content/aip/journal/bmf/8/1/10.1063/1.4863802. [cited on p. 2]

[25] Y.-L. Chen, M. D. Graham, J. J. de Pablo, K. Jo, and D. C. Schwartz. Dna molecules in microfluidic oscillatory flow. *Macromolecules*, 38(15):6680–6687, 2005. doi: 10.1021/ma050238d. URL http://dx.doi.org/10.1021/ma050238d. PMID: 19057656. [cited on p. 2]

[26] J. R. Hove, R. W. Köster, A. S. Forouhar, G. Acevedo-Bolton, S. E. Fraser, and M. Gharib. Intracardiac fluid forces are an essential epigenetic factor for embryonic cardiogenesis. *Nature*, 421(6919):172–177, January 2003. ISSN 0028-0836. doi: 10.1038/nature01282. URL http://www.nature.com/nature/journal/v421/n6919/full/nature01282.html. [cited on p. 2]

[27] S. R. Kirchner, S. Nedev, S. Carretero-Palacios, A. Mader, M. Opitz, T. LohmÃ¼ller, and Jochen Feldmann. Direct optical monitoring of flow generated by bacterial flagellar rotation. *Applied Physics Letters*, 104(9):093701, 2014. doi: http://dx.doi.org/10.1063/1.4867196. URL http://scitation.aip.org/content/aip/journal/apl/104/9/10.1063/1.4867196. [cited on p. 2]

[28] H. Mushfique, J. Leach, H. Yin, R. Di Leonardo, M. J. Padgett, and J. M. Cooper. 3d mapping of microfluidic flow in laboratory-on-a-chip structures using optical tweezers. *Analytical Chemistry*, 80(11):4237–4240, 2008. doi: 10.1021/ac8002006. URL http://dx.doi.org/10.1021/ac8002006. PMID: 18442263. [cited on p. 2]

[29] R. Di Leonardo, J. Leach, H. Mushfique, J. M. Cooper, G. Ruocco, and M. J. Padgett. Multipoint holographic optical velocimetry in microfluidic systems. *Phys. Rev. Lett.*, 96:134502, Apr 2006. doi: 10.1103/PhysRevLett.96.134502. URL http://link.aps.org/doi/10.1103/PhysRevLett.96.134502. [cited on p. 2]

[30] T. M. Squires and S. R. Quake. Microfluidics: Fluid physics at the nanoliter scale. *Rev. Mod. Phys.*, 77:977–1026, Oct 2005. doi: 10.1103/RevModPhys.77.977. URL http://link.aps.org/doi/10.1103/RevModPhys.77.977. [cited on p. 2]

[31] F. R. Phelan, N. R. Hughes, and J. A. Pathak. Chaotic mixing in microfluidic devices driven by oscillatory cross flow. *Physics of Fluids (1994-present)*, 20(2):023101, 2008. doi: http://dx.doi.org/10.1063/1.2830550. URL http://scitation.aip.org/content/aip/journal/pof2/20/2/10.1063/1.2830550. [cited on p. 2]

[32] L Euler. Memoire sur l'effet de la propagation successive de la lumiere dans l'apparition tant des planetes que des cometes. *Memoires de l'academie des sciences de Berlin 2*, pages 141–181, 1746. URL http://eulerarchive.maa.org/docs/originals/E104.pdf. [cited on p. 6]

[33] J. C. Maxwell. *A treatise on electricity and magnetism*. Oxford: Clarendon Press, 1873. [cited on p. 6]

[34] A. Bartoli. Il calorico raggiante e il secondo principio di termodinamica. *Il Nuovo Cimento Series 3*, 15:193–202, December 1884. doi: 10.1007/BF02737234. [cited on p. 6]

[35] P. Lebedev. Untersuchungen über die druckkräfte des lichtes. *Ann. Phys.*, 311(11):433–458, 1901. doi: 10.1002/andp.19013111102. [cited on p. 6]

[36] J. Liouville. Sur la théorie de la variation des constantes arbitraires. *J. Math. Pures Appl.*, 3(3):342–349, 1838. [cited on p. 6]

[37] T. Heidarzadeh. *A history of physical theories of comets, from Aristotle to Whipple*, volume 19. Springer, 2008. [cited on p. 6]

[38] A. Ashkin. Acceleration and trapping of particles by radiation pressure. *Physical review letters*, 24(4):156, 1970. [cited on p. 7]

[39] A. Ashkin and JM Dziedzic. Optical levitation by radiation pressure. *Applied Physics Letters*, 19 (8):283–285, 1971. [cited on p. 7]

[40] A. Ashkin, J. M. Dziedzic, J. E. Bjorkholm, and Steven Chu. Observation of a single-beam gradient force optical trap for dielectric particles. *Optics Letters*, 11(5):288–290, May

1986. doi: 10.1364/OL.11.000288. URL http://ol.osa.org/abstract.cfm?URI=ol-11-5-288. [cited on p. 7]

[41] S. Chu. Nobel lecture: The manipulation of neutral particles. *Rev. Mod. Phys.*, 70:685–706, Jul 1998. doi: 10.1103/RevModPhys.70.685. URL http://link.aps.org/doi/10.1103/RevModPhys.70.685. [cited on p. 7]

[42] C. N. Cohen-Tannoudji. Nobel lecture: Manipulating atoms with photons. *Rev. Mod. Phys.*, 70:707–719, Jul 1998. doi: 10.1103/RevModPhys.70.707. URL http://link.aps.org/doi/10.1103/RevModPhys.70.707. [cited on pp.]

[43] W. D. Phillips. Nobel lecture: Laser cooling and trapping of neutral atoms. *Rev. Mod. Phys.*, 70:721–741, Jul 1998. doi: 10.1103/RevModPhys.70.721. URL http://link.aps.org/doi/10.1103/RevModPhys.70.721. [cited on p. 7]

[44] E. A. Cornell and C. E. Wieman. Nobel lecture: Bose-einstein condensation in a dilute gas, the first 70 years and some recent experiments. *Rev. Mod. Phys.*, 74:875–893, Aug 2002. doi: 10.1103/RevModPhys.74.875. URL http://link.aps.org/doi/10.1103/RevModPhys.74.875. [cited on p. 7]

[45] W. Ketterle. Nobel lecture: When atoms behave as waves: Bose-einstein condensation and the atom laser. *Rev. Mod. Phys.*, 74:1131–1151, Nov 2002. doi: 10.1103/RevModPhys.74.1131. URL http://link.aps.org/doi/10.1103/RevModPhys.74.1131. [cited on p. 7]

[46] A. Jonáš and P. Zemánek. Light at work: The use of optical forces for particle manipulation, sorting, and analysis. *ELECTROPHORESIS*, 29(24):4813–4851, 2008. ISSN 1522-2683. doi: 10.1002/elps.200800484. URL http://dx.doi.org/10.1002/elps.200800484. [cited on pp. 7, 10,12]

[47] M. Dienerowitz, M. Mazilu, and K. Dholakia. Optical manipulation of nanoparticles: a review. *Journal of Nanophotonics*, 2(1):021875–021875–32, 2008. doi: 10.1117/1.2992045. URL http://dx.doi.org/10.1117/1.2992045. [cited on pp.]

[48] O. M. Maragò, P. H. Jones, P. G. Gucciardi, G. Volpe, and A. C. Ferrari. Optical trapping and manipulation of nanostructures. *Nature Nanotechnology*, 8(11):807–819, November 2013. ISSN 1748-3387. doi: 10.1038/nnano.2013.208. URL http://www.nature.com/nnano/journal/v8/n11/full/nnano.2013.208.html. [cited on p. 7]

[49] P. C. Chaumet and M. Nieto-Vesperinas. Time-averaged total force on a dipolar sphere in an electromagnetic field. *Optics Letters*, 25(15):1065–1067, August 2000. doi: 10.1364/OL.25.001065. URL http://ol.osa.org/abstract.cfm?URI=ol-25-15-1065. [cited on p. 10]

[50] B. T. Draine. The discrete-dipole approximation and its application to interstellar graphite grains. *Astrophysical Journal*, 333:848–872, 1988. [cited on p. 11]

[51] A. Ashkin. Forces of a single-beam gradient laser trap on a dielectric sphere in the ray optics regime. *Biophysical Journal*, 61(2):569–582, February 1992. ISSN 0006-3495. URL http://www.ncbi.nlm.nih.gov/pmc/articles/PMC1260270/. PMID: 19431818 PMCID: PMC1260270. [cited on p. 13]

[52] G. Mie. Beiträge zur optik trüber medien, speziell kolloidaler metallösungen. *Annalen der Physik*, (25):377–452, 1908. [cited on p. 15]

[53] W.-C. Tsai and R. G. Pogorzelski. Eigenfunction solution of the scattering of beam radiation fields by spherical objects. *J. Opt. Soc. Am.*, 65(12):1457–1463, Dec 1975. doi: 10.1364/JOSA.65.001457. URL http://www.opticsinfobase.org/abstract.cfm?URI=josa-65-12-1457. [cited on p. 15]

[54] W. G. Tam and R. Corriveau. Scattering of electromagnetic beams by spherical objects. *J. Opt. Soc. Am.*, 68(6):763, Jun 1978. doi: 10.1364/JOSA.68.000763. URL http://www.opticsinfobase.org/abstract.cfm?URI=josa-68-6-763. [cited on pp.]

[55] R. J. Pogorzelski. Provision of exact formulations for the "forward scattering of a gaussian beam by a nonabsorbing sphere": comment. *Appl. Opt.*, 34(36):8474–8474, Dec 1995. doi: 10.1364/AO.34.008474. URL http://ao.osa.org/abstract.cfm?URI=ao-34-36-8474. [cited on pp.]

[56] J. A. Lock and G. Gouesbet. Generalized lorenz-mie theory and applications. *Journal of Quantitative Spectroscopy and Radiative Transfer*, 110(11):800 – 807, 2009. ISSN 0022-4073. doi: http://dx.doi.org/10.1016/j.jqsrt.2008.11.013. URL http://www.sciencedirect.com/science/article/pii/S0022407308002653. Light Scattering: Mie and More Commemorating 100 years of Mie's 1908 publication. [cited on p. 16]

[57] G. Gouesbet and G. Gréhan. *Generalized Lorenz-Mie Theories*. Springer Science & Business Media, 2011. [cited on p. 15]

[58] T. A. Nieminen, H. Rubinsztein-Dunlop, and N. R. Heckenberg. Multipole expansion of strongly focussed laser beams. *Journal of Quantitative Spectroscopy and Radiative Transfer*, 79-80(0):1005 – 1017, 2003. ISSN 0022-4073. doi: http://dx.doi.org/10.1016/S0022-4073(02)00335-7. URL http://www.sciencedirect.com/science/article/pii/S0022407302003357. Electromagnetic and Light Scattering by Non-Spherical Particles. [cited on p. 15]

[59] P. C. Waterman. Symmetry, unitarity, and geometry in electromagnetic scattering. *Phys. Rev. D*, 3:825–839, Feb 1971. doi: 10.1103/PhysRevD.3.825. URL http://link.aps.org/doi/10.1103/PhysRevD.3.825. [cited on p. 16]

[60] M. I. Mishchenko. Light scattering by randomly oriented axially symmetric particles. *J. Opt. Soc. Am. A*, 8(6):871–882, Jun 1991. doi: 10.1364/JOSAA.8.000871. URL http://josaa.osa.org/abstract.cfm?URI=josaa-8-6-871. [cited on pp.]

[61] T. A. Nieminen, H. Rubinsztein-Dunlop, and N. R. Heckenberg. Calculation of the t-matrix: general considerations and application of the point-matching method. *Journal of Quantitative Spectroscopy and Radiative Transfer*, 79-80(0):1019 – 1029, 2003. ISSN 0022-4073. doi: http://dx.doi.org/10.1016/S0022-4073(02)00336-9. URL http://www.sciencedirect.com/science/article/pii/S0022407302003369. Electromagnetic and Light Scattering by Non-Spherical Particles. [cited on pp. 15,16]

[62] B. Brock. Using vector spherical harmonics to compute antenna mutual impedance from measured or computed fields. *Sandia Report SAND2000-2217-Revised Sandia National Laboratories, Albuquerque, NM*, 2001. [cited on p. 15]

[63] G. Gouesbet, B. Maheu, and G. Gréhan. Light scattering from a sphere arbitrarily located in a gaussian beam, using a bromwich formulation. *J. Opt. Soc. Am. A*, 5(9):1427–1443, Sep 1988. doi: 10.1364/JOSAA.5.001427. URL http://josaa.osa.org/abstract.cfm?URI=josaa-5-9-1427. [cited on p. 16]

[64] B. Maheu, G. Gouesbet, and G. Grehan. A concise presentation of the generalized lorenz-mie theory for arbitrary location of the scatterer in an arbitrary incident profile. *Journal of Optics*, 19(2):59, 1988. URL http://stacks.iop.org/0150-536X/19/i=2/a=002. [cited on pp.]

[65] G. Gouesbet, G. Grehan, and B. Maheu. Expressions to compute the coefficients g m n in the generalized lorenz-mie theory using finite series. *Journal of Optics*, 19(1):35, 1988. URL http://stacks.iop.org/0150-536X/19/i=1/a=005. [cited on pp.]

[66] J. A. Lock. Calculation of the radiation trapping force for laser tweezers by use of generalized lorenz-mie theory. i. localized model description of an on-axis tightly focused laser beam with spherical aberration. *Appl. Opt.*, 43(12):2532–2544, Apr 2004. doi: 10.1364/AO.43.002532. URL http://ao.osa.org/abstract.cfm?URI=ao-43-12-2532. [cited on pp.]

[67] J. A. Lock. Calculation of the radiation trapping force for laser tweezers by use of generalized lorenz-mie theory. ii. on-axis trapping force. *Appl. Opt.*, 43(12):2545–2554, Apr 2004. doi: 10.1364/AO.43.002545. URL http://ao.osa.org/abstract.cfm?URI=ao-43-12-2545. [cited on pp.]

[68] J. A. Lock, S. Y. Wrbanek, and K. E. Weiland. Scattering of a tightly focused beam by an optically trapped particle. *Appl. Opt.*, 45(15):3634–3645, May 2006. doi: 10.1364/AO.45.003634. URL http://ao.osa.org/abstract.cfm?URI=ao-45-15-3634. [cited on pp.]

[69] T. A. Nieminen, N. du Preez-Wilkinson, A. B. Stilgoe, V. L. Y. Loke, A. A. M. Bui, and H. Rubinsztein-Dunlop. Optical tweezers: Theory and modelling. *Journal of Quantitative Spectroscopy and Radiative Transfer*, 146(0):59 – 80, 2014. ISSN 0022-4073. doi: http://dx.doi.org/10.1016/j.jqsrt.2014.04.003. URL http://www.sciencedirect.com/science/article/pii/S0022407314001587. Electromagnetic and Light Scattering by Nonspherical Particles {XIV}. [cited on pp. 16,46]

[70] T. A. Nieminen, V. L. Y. Loke, A. B. Stilgoe, G. KnÃ¶ner, A. M. BraÅ„czyk, N. R. Heckenberg, and H. Rubinsztein-Dunlop. Optical tweezers computational toolbox. *Journal of Optics A: Pure and Applied Optics*, 9(8):S196, 2007. URL http://stacks.iop.org/1464-4258/9/i=8/a=S12. [cited on p. 16]

[71] J. C. Crocker and D. G. Grier. Microscopic measurement of the pair interaction potential of charge-stabilized colloid. *Physical Review Letters*, 73(2):352–355, July 1994. doi: 10.1103/PhysRevLett.73.352. URL http://link.aps.org/doi/10.1103/PhysRevLett.73.352. [cited on p. 17]

[72] J. C. Crocker and D. G. Grier. When like charges attract: The effects of geometrical confinement on long-range colloidal interactions. *Physical Review Letters*, 77(9):1897–1900, August 1996. doi: 10.1103/PhysRevLett.77.1897. URL http://link.aps.org/doi/10.1103/PhysRevLett.77.1897. [cited on pp.]

[73] J. C. Crocker, J. A. Matteo, A. D. Dinsmore, and A. G. Yodh. Entropic attraction and repulsion in binary colloids probed with a line optical tweezer. *Physical Review Letters*, 82(21):4352–4355, May 1999. doi: 10.1103/PhysRevLett.82.4352. URL http://link.aps.org/doi/10.1103/PhysRevLett.82.4352. [cited on pp.]

[74] Y. N. Ohshima, H. Sakagami, K. Okumoto, A. Tokoyoda, T. Igarashi, K. B. Shintaku, S. Toride, H. Sekino, K. Kabuto, and I. Nishio. Direct measurement of infinitesimal depletion force in a colloid-polymer mixture by laser radiation pressure. *Physical Review Letters*, 78(20):3963–3966, May 1997. doi: 10.1103/PhysRevLett.78.3963. URL http://link.aps.org/doi/10.1103/PhysRevLett.78.3963. [cited on pp.]

[75] R. Verma, J. C. Crocker, T. C. Lubensky, and A. G. Yodh. Attractions between hard colloidal spheres in semiflexible polymer solutions. *Macromolecules*, 33(1):177–186, January 2000. ISSN 0024-9297. doi: 10.1021/ma990362v. URL http://dx.doi.org/10.1021/ma990362v. [cited on pp.]

[76] G. M. Wang, E. M. Sevick, E. Mittag, D. J. Searles, and D. J. Evans. Experimental demonstration of violations of the second law of thermodynamics for small systems and short time scales. *Physical Review Letters*, 89(5):050601, July 2002. doi: 10.1103/PhysRevLett.89.050601. URL http://link.aps.org/doi/10.1103/PhysRevLett.89.050601. [cited on pp.]

[77] A. G. Yodh, K. Lin, J. C. Crocker, A. D. Dinsmore, R. Verma, and P. D. Kaplan. Entropically driven self–assembly and interaction in suspension. *Philosophical Transactions of the Royal Society of London A: Mathematical, Physical and Engineering Sciences*, 359(1782):921–937, May 2001. ISSN 1364-503X, 1471-2962. doi: 10.1098/rsta.2000.0810. URL http://rsta.royalsocietypublishing.org/content/359/1782/921. [cited on p. 17]

[78] A. Ashkin. History of optical trapping and manipulation of small-neutral particle, atoms, and molecules. *IEEE Journal of Selected Topics in Quantum Electronics*, 6(6):841–856, November 2000. ISSN 1077-260X. doi: 10.1109/2944.902132. [cited on p. 17]

[79] M. W. Berns. Laser scissors and tweezers. *Scientific American*, 278(4):62–67, April 1998. ISSN 0036-8733. doi: 10.1038/scientificamerican0498-62. URL http://www.nature.com/doifinder/10.1038/scientificamerican0498-62. [cited on pp.]

[80] S. M. Block. Real engines of creation. *Nature*, 386(6622):217–219, March 1997. doi: 10.1038/386217a0. URL http://www.nature.com/nature/journal/v386/n6622/abs/386217a0.html. [cited on pp.]

[81] M. S. Z. Kellermayer, S. B. Smith, H. L. Granzier, and C. Bustamante. Folding-unfolding transitions in single titin molecules characterized with laser tweezers. *Science*, 276(5315):1112–1116, May 1997. ISSN 0036-8075. URL http://www.jstor.org/stable/2893522. [cited on pp.]

[82] R. G. Larson, T. T. Perkins, D. E. Smith, and S. Chu. Hydrodynamics of a DNA molecule in a flow field. *Physical Review E*, 55(2):1794–1797, February 1997. doi: 10.1103/PhysRevE.55.1794. URL http://link.aps.org/doi/10.1103/PhysRevE.55.1794. [cited on pp.]

[83] A. D. Mehta, M. Rief, J. A. Spudich, D. A. Smith, and R. M. Simmons. Single-molecule biomechanics with optical methods. *Science*, 283(5408):1689–1695, March 1999. ISSN 0036-8075. URL http://www.jstor.org/stable/2897501. [cited on pp.]

[84] S. B. Smith, Y. Cui, and C. Bustamante. Overstretching b-DNA: The elastic response of individual double-stranded and single-stranded DNA molecules. *Science*, 271(5250):795–799, February 1996. ISSN 0036-8075. URL http://www.jstor.org/stable/2889889. [cited on pp.]

[85] M. D. Wang, H. Yin, R. Landick, J. Gelles, and S. M. Block. Stretching DNA with optical tweezers. *Biophysical Journal*, 72(3):1335–1346, March 1997. ISSN 0006-3495. doi: 10.1016/S0006-3495(97)78780-0. URL http://www.sciencedirect.com/science/article/pii/S0006349597787800. [cited on p. 17]

[86] W.i Ni, H. Ba, A. A. Lutich, F. Jäckel, and J. Feldmann. Enhancing single-nanoparticle surface-chemistry by plasmonic overheating in an optical trap. *Nano Letters*, 12(9):4647–4650, September 2012. ISSN 1530-6984. doi: 10.1021/nl301937j. URL http://dx.doi.org/10.1021/nl301937j. [cited on p. 17]

[87] S. Nedev, A. S. Urban, A. A. Lutich, and J. Feldmann. Optical force stamping lithography. *Nano Letters*, 11(11):5066–5070, 2011. doi: 10.1021/nl203214n. URL http://dx.doi.org/10.1021/nl203214n. PMID: 21992538. [cited on p. 17]

[88] K. Berg-Sørensen and H. Flyvbjerg. Power spectrum analysis for optical tweezers. *Review of Scientific Instruments*, 75(3):594–612, March 2004. ISSN 0034-6748, 1089-7623. doi: 10.1063/1.1645654. URL http://scitation.aip.org/content/aip/journal/rsi/75/3/10.1063/1.1645654. [cited on pp. 19, 21,40]

[89] F Reif. *Fundamentals of Statistical and Thermal Physics*. McGraw-Hill, 1965. [cited on pp. 19,20]

[90] N. Wax, editor. *Selected Papers on Noise and Stochastic Processes*. Dover Publications, Incorporated, 1954. [cited on p. 21]

[91] P. M. Hansen, I. M. Tolic-Nørrelykke, H. Flyvbjerg, and K. Berg-Sørensen. tweezercalib 2.1: Faster version of matlab package for precise calibration of optical tweezers. *Computer Physics Communications*, 175(8):572 – 573, 2006. ISSN 0010-4655. doi: http://dx.doi.org/10.1016/j.cpc.2006.07.009. URL http://www.sciencedirect.com/science/article/pii/S001046550600289X. [cited on pp. 21, 40,68]

[92] S. F. Tolić-Nørrelykke, E. Schäffer, J. Howard, F. S. Pavone, F. Jülicher, and H. Flyvbjerg. Calibration of optical tweezers with positional detection in the back focal plane. *Review of*

Scientific Instruments, 77(10):103101, October 2006. ISSN 0034-6748, 1089-7623. doi: 10.1063/1.2356852. URL http://scitation.aip.org/content/aip/journal/rsi/77/10/10.1063/1.2356852. [cited on p. 21]

[93] T. Wohland, A. Rosin, and E. H. K. Stelzer. Theoretical determination of the influence of the polarization on forces exerted by optical tweezers. *Optik*, 102(4):181–190, 1996. ISSN 0030-4026. URL http://cat.inist.fr/?aModele=afficheN&cpsidt=3109875. [cited on pp. 22,68]

[94] S. R. De Groot and P. Mazur. *Non-Equilibrium Thermodynamics*. Amsterdam: North Holland, January 1962. ISBN 978-0-486-15350-6. [cited on p. 22]

[95] C. Ludwig. Diffusion zwischen ungleich erw armten orten gleich zusammen-gesetzter l osungen. *Sitzber. Akad. Wiss. Wien, Math.-naturw. Kl.*, 20:539, 1859. [cited on p. 22]

[96] C. Soret. Sur l'état d'équilibre que prend, du point de vue de sa concentration, une dissolution saline primitivement homogène, dont deux parties sont portées à des températures différentes. *Arch. Sci. Phys. Nat. Genève*, 2:48–61, 1879. [cited on p. 22]

[97] J. V. Tyrrell. *Diffusion and Heat Flow in Liquids*. Butterworths, London, 1961. [cited on p. 22]

[98] W. C. Hinds. *Aerosol Technology: Properties, Behavior, and Measurement of Airborne Particles*. Wiley, 2 edition, 1999. URL http://eu.wiley.com/WileyCDA/WileyTitle/productCd-0471194107.html. [cited on p. 22]

[99] John Tyndall. *Scientific Addresses*. New Haven, Conn., C.C. Chatfield & Co., 1870. URL http://archive.org/details/scientificaddre01tyndgoog/. [cited on p. 23]

[100] A. Würger. Heat capacity-driven inverse soret effect of colloidal nanoparticles. *EPL (Europhysics Letters)*, 74(4):658, 2006. URL http://stacks.iop.org/0295-5075/74/i=4/a=658. [cited on p. 23]

[101] R. Piazza. Thermophoresis: moving particles with thermal gradients. *Soft Matter*, 4:1740–1744, 2008. doi: 10.1039/B805888C. URL http://dx.doi.org/10.1039/B805888C. [cited on pp. 23,74]

[102] R. Piazza and A. Parola. Thermophoresis in colloidal suspensions. *Journal of Physics: Condensed Matter*, 20(15):153102, 2008. URL http://stacks.iop.org/0953-8984/20/i=15/a=153102. [cited on pp. 23,74]

[103] E. Ruckenstein. Can phoretic motions be treated as interfacial tension gradient driven phenomena? *Journal of Colloid and Interface Science*, 83(1):77 – 81, 1981. ISSN 0021-9797. doi: http://dx.doi.org/10.1016/0021-9797(81)90011-4. URL http://www.sciencedirect.com/science/article/pii/0021979781900114. [cited on pp. 23,24]

[104] R. Piazza and A. Guarino. Soret effect in interacting micellar solutions. *Physical Review Letters*, 88(20):208302, May 2002. doi: 10.1103/PhysRevLett.88.208302. URL http://link.aps.org/doi/10.1103/PhysRevLett.88.208302. [cited on p. 23]

[105] S. A. Putnam and D. G. Cahill. Transport of nanoscale latex spheres in a temperature gradient. *Langmuir*, 21(12):5317–5323, June 2005. ISSN 0743-7463. doi: 10.1021/la047056h. URL http://dx.doi.org/10.1021/la047056h. [cited on pp.]

[106] S. Duhr and D. Braun. Why molecules move along a temperature gradient. *Proceedings of the National Academy of Sciences*, 103(52):19678–19682, December 2006. ISSN 0027-8424, 1091-6490. doi: 10.1073/pnas.0603873103. URL http://www.pnas.org/content/103/52/19678. [cited on p. 23]

[107] H. Ning, J. K. G. Dhont, and S. Wiegand. Thermal-diffusive behavior of a dilute solution of charged colloids. *Langmuir*, 24(6):2426–2432, March 2008. ISSN 0743-7463. doi: 10.1021/la703517u. URL http://dx.doi.org/10.1021/la703517u. [cited on p. 23]

[108] D. Stadelmaier and W. Köhler. From small molecules to high polymers: Investigation of the crossover of thermal diffusion in dilute polystyrene solutions. *Macromolecules*, 41(16):6205–

6209, August 2008. ISSN 0024-9297. doi: 10.1021/ma800891p. URL http://dx.doi.org/10.1021/ma800891p. [cited on p. 23]

[109] S. Wiegand. Thermal diffusion in liquid mixtures and polymer solutions. *Journal of Physics: Condensed Matter*, 16(10):R357, March 2004. ISSN 0953-8984. doi: 10.1088/0953-8984/16/10/R02. URL http://iopscience.iop.org/0953-8984/16/10/R02. [cited on p. 23]

[110] A. Würger. Thermal non-equilibrium transport in colloids. *Reports on Progress in Physics*, 73(12):126601, December 2010. ISSN 0034-4885. doi: 10.1088/0034-4885/73/12/126601. URL http://iopscience.iop.org/0034-4885/73/12/126601. [cited on p. 24]

[111] E. Bringuier and A. Bourdon. Colloid transport in nonuniform temperature. *Phys. Rev. E*, 67: 011404, Jan 2003. doi: 10.1103/PhysRevE.67.011404. URL http://link.aps.org/doi/10.1103/PhysRevE.67.011404. [cited on pp.]

[112] S. Fayolle, T. Bickel, S. Le Boiteux, and A. Würger. Thermodiffusion of charged micelles. *Phys. Rev. Lett.*, 95:208301, Nov 2005. doi: 10.1103/PhysRevLett.95.208301. URL http://link.aps.org/doi/10.1103/PhysRevLett.95.208301. [cited on pp.]

[113] K.I. Morozov. Thermal diffusion in disperse systems. *Journal of Experimental and Theoretical Physics*, 88(5):944–946, 1999. ISSN 1063-7761. doi: 10.1134/1.558875. URL http://dx.doi.org/10.1134/1.558875. [cited on p. 24]

[114] A. Parola and R. Piazza. Particle thermophoresis in liquids. *Eur. Phys. J. E*, 15(3):255–263, 2004. doi: 10.1140/epje/i2004-10065-5. URL http://dx.doi.org/10.1140/epje/i2004-10065-5. [cited on pp. 24,74]

[115] I. Doron-Mor, Z. Barkay, N. Filip-Granit, A. Vaskevich, and I. Rubinstein. Ultrathin gold island films on silanized glass. morphology and optical properties. *Chemistry of Materials*, 16(18): 3476–3483, September 2004. ISSN 0897-4756. doi: 10.1021/cm049605a. URL http://dx.doi.org/10.1021/cm049605a. [cited on p. 25]

[116] T. Andersson. The resistance of ultra-thin gold films during and after deposition. *Thin Solid Films*, 29(1):L21–L23, September 1975. ISSN 0040-6090. doi: 10.1016/0040-6090(75)90233-3. URL http://www.sciencedirect.com/science/article/pii/0040609075902333. [cited on p. 25]

[117] N. Goutev and M. Futamata. Attenuated total reflection surface-enhanced infrared absorption spectroscopy of carboxyl terminated self-assembled monolayers on gold. *Applied Spectroscopy*, 57(5):506–513, May 2003. doi: 10.1366/000370203321666506. [cited on p. 25]

[118] R. Gupta, M. J. Dyer, and W. A. Weimer. Preparation and characterization of surface plasmon resonance tunable gold and silver films. *Journal of Applied Physics*, 92(9):5264–5271, November 2002. ISSN 0021-8979, 1089-7550. doi: 10.1063/1.1511275. URL http://scitation.aip.org/content/aip/journal/jap/92/9/10.1063/1.1511275. [cited on pp.]

[119] R. Gupta and W. A. Weimer. High enhancement factor gold films for surface enhanced raman spectroscopy. *Chemical Physics Letters*, 374(3–4):302–306, June 2003. ISSN 0009-2614. doi: 10.1016/S0009-2614(03)00737-1. URL http://www.sciencedirect.com/science/article/pii/S0009261403007371. [cited on pp.]

[120] T. Jensen, L. Kelly, A. Lazarides, and G. C. Schatz. Electrodynamics of noble metal nanoparticles and nanoparticle clusters. *Journal of Cluster Science*, 10(2):295–317, June 1999. ISSN 1040-7278, 1572-8862. doi: 10.1023/A:1021977613319. URL http://link.springer.com/article/10.1023/A%3A1021977613319. [cited on pp.]

[121] P. A. Mosier-Boss and S. H. Lieberman. Comparison of three methods to improve adherence of thin gold films to glass substrates and their effect on the SERS response. *Applied Spectroscopy*, 53(7):862–873, July 1999. doi: 10.1366/0003702991947469. [cited on pp.]

[122] G. A. Niklasson and C. G. Granqvist. Noble-metal-based transparent infrared reflectors: Improved performance caused by nonhomogeneous film structure. *Applied Physics*

Letters, 46(8):713–715, April 1985. ISSN 0003-6951, 1077-3118. doi: 10.1063/1.95484. URL http://scitation.aip.org/content/aip/journal/apl/46/8/10.1063/1.95484. [cited on pp.]

[123] M. Osawa, K.-I. Ataka, K. Yoshii, and Y. Nishikawa. Surface-enhanced infrared spectroscopy: The origin of the absorption enhancement and band selection rule in the infrared spectra of molecules adsorbed on fine metal particles. *Applied Spectroscopy*, 47(9):1497–1502, September 1993. doi: 10.1366/0003702934067478. [cited on pp.]

[124] G. B. Smith. Very thin gold films produced with ion plating for improved transparent infrared reflectors. *Applied Physics Letters*, 46(8):716–718, April 1985. ISSN 0003-6951, 1077-3118. doi: 10.1063/1.95485. URL http://scitation.aip.org/content/aip/journal/apl/46/8/10.1063/1.95485. [cited on pp.]

[125] G. B. Smith, G. A. Niklasson, J. S. E. M. Svensson, and C. G. Granqvist. Noble-metal-based transparent infrared reflectors: Experiments and theoretical analyses for very thin gold films. *Journal of Applied Physics*, 59(2):571–581, January 1986. ISSN 0021-8979, 1089-7550. doi: 10.1063/1.336615. URL http://scitation.aip.org/content/aip/journal/jap/59/2/10.1063/1.336615. [cited on pp.]

[126] G. B. Smith, G. A. Niklasson, J. S. E. M. Svensson, and C. G. Granqvist. Noble-metal-based transparent infrared-reflectors: Preparation and analysis of thin gold films. *Solar Energy Materials*, 14(3–5):257–268, November 1986. ISSN 0165-1633. doi: 10.1016/0165-1633(86)90052-3. URL http://www.sciencedirect.com/science/article/pii/0165163386900523. [cited on pp.]

[127] G. D. Sockalingum, A. Beljebbar, H. Morjani, J. F. Angiboust, and M. Manfait. Characterization of island films as surface-enhanced raman spectroscopy substrates for detecting low antitumor drug concentrations at single cell level. *Biospectroscopy*, 4(S5):S71–S78, January 1998. ISSN 1520-6343. doi: 10.1002/(SICI)1520-6343(1998)4:5+3.0.CO;2-Z. URL http://onlinelibrary.wiley.com/doi/10.1002/(SICI)1520-6343(1998)4:5+<S71::AID-BSPY8>3.0.CO;2-Z/abstract. [cited on pp.]

[128] M. Tsen and L. Sun. Surface-enhanced raman scattering from functionalized self-assembled monolayers: Part 1. distance dependence of enhanced raman scattering from a terminal phenyl group. *Analytica Chimica Acta*, 307(2–3):333–340, May 1995. ISSN 0003-2670. doi: 10.1016/0003-2670(94)00594-C. URL http://www.sciencedirect.com/science/article/pii/000326709400594C. [cited on pp.]

[129] J. Ye, Q.and Fang and L. Sun. Surface-enhanced raman scattering from functionalized self-assembled monolayers. 2. distance dependence of enhanced raman scattering from an azobenzene terminal group. *The Journal of Physical Chemistry B*, 101(41):8221–8224, October 1997. ISSN 1520-6106. doi: 10.1021/jp970869c. URL http://dx.doi.org/10.1021/jp970869c. [cited on p. 25]

[130] U. Kreibig and M. Vollmer. *Optical Properties of Metal Clusters*. Springer-Verlag Berlin Heidelberg, 1995. doi: 10.1007/978-3-662-09109-8. [cited on p. 26]

[131] S. C. Warren and E. Thimsen. Plasmonic solar water splitting. *Energy & Environmental Science*, 5(1):5133–5146, January 2012. ISSN 1754-5706. doi: 10.1039/C1EE02875H. URL http://pubs.rsc.org/en/content/articlelanding/2012/ee/c1ee02875h. [cited on p. 27]

[132] T. Klar, M. Perner, S. Grosse, G. von Plessen, W. Spirkl, and J. Feldmann. Surface-plasmon resonances in single metallic nanoparticles. *Phys. Rev. Lett.*, 80:4249–4252, May 1998. doi: 10.1103/PhysRevLett.80.4249. URL http://link.aps.org/doi/10.1103/PhysRevLett.80.4249. [cited on p. 27]

[133] W. S. Fann, R. Storz, H. W. K. Tom, and J. Bokor. Electron thermalization in gold. *Phys. Rev. B*, 46:13592–13595, Nov 1992. doi: 10.1103/PhysRevB.46.13592. URL http://link.aps.org/doi/10.1103/PhysRevB.46.13592. [cited on p. 27]

[134] C.-K. Sun, F. Vallée, L. H. Acioli, E. P. Ippen, and J. G. Fujimoto. Femtosecond-tunable measurement of electron thermalization in gold. *Phys. Rev. B*, 50:15337–15348, Nov 1994. doi: 10.1103/PhysRevB.50.15337. URL http://link.aps.org/doi/10.1103/PhysRevB.50.15337. [cited on p. 27]

[135] R. W. Schoenlein, W. Z. Lin, J. G. Fujimoto, and G. L. Eesley. Femtosecond studies of nonequilibrium electronic processes in metals. *Phys. Rev. Lett.*, 58:1680–1683, Apr 1987. doi: 10.1103/PhysRevLett.58.1680. URL http://link.aps.org/doi/10.1103/PhysRevLett.58.1680. [cited on p. 27]

[136] H. E. Elsayed-Ali, T. Juhasz, G. O. Smith, and W. E. Bron. Femtosecond thermoreflectivity and thermotransmissivity of polycrystalline and single-crystalline gold films. *Phys. Rev. B*, 43:4488–4491, Feb 1991. doi: 10.1103/PhysRevB.43.4488. URL http://link.aps.org/doi/10.1103/PhysRevB.43.4488. [cited on pp.]

[137] J. Hodak, I. Martini, and G. V. Hartland. Ultrafast study of electronâ€“phonon coupling in colloidal gold particles. *Chemical Physics Letters*, 284(1â€“2):135 – 141, 1998. ISSN 0009-2614. doi: http://dx.doi.org/10.1016/S0009-2614(97)01369-9. URL http://www.sciencedirect.com/science/article/pii/S0009261497013699. [cited on p. 27]

[138] M. Hu and G. V. Hartland. Heat dissipation for au particles in aqueous solution: Relaxation time versus size. *The Journal of Physical Chemistry B*, 106(28):7029–7033, 2002. doi: 10.1021/jp020581+. URL http://dx.doi.org/10.1021/jp020581+. [cited on p. 27]

[139] A. Ohlinger, A. Deak, A. A. Lutich, and J. Feldmann. Optically trapped gold nanoparticle enables listening at the microscale. *Phys. Rev. Lett.*, 108:018101, Jan 2012. doi: 10.1103/PhysRevLett.108.018101. URL http://link.aps.org/doi/10.1103/PhysRevLett.108.018101. [cited on pp. 30, 31, 32,61]

[140] Research Highlights. Physics: 'nanoear' hears small sounds. *Nature*, 481(7380):116–116, January 2012. ISSN 0028-0836. doi: 10.1038/481116b. URL http://www.nature.com/nature/journal/v481/n7380/full/481116b.html. [cited on p. 31]

[141] P. M. Hansen, V. K. Bhatia, N. Harrit, and L. Oddershede. Expanding the Optical Trapping Range of Gold Nanoparticles. *Nano Letters*, 5(10):1937–1942, October 2005. ISSN 1530-6984. doi: 10.1021/nl051289r. URL http://dx.doi.org/10.1021/nl051289r. [cited on p. 36]

[142] D. Ott, S. Nader, S. Reihani, and Lene B. Oddershede. Simultaneous three-dimensional tracking of individual signals from multi-trap optical tweezers using fast and accurate photodiode detection. *Optics Express*, 22(19):23661, September 2014. ISSN 1094-4087. doi: 10.1364/OE.22.023661. URL http://www.opticsinfobase.org/abstract.cfm?URI=oe-22-19-23661. [cited on p. 40]

[143] F. Caruso, H. Lichtenfeld, E. Donath, and H. Möhwald. Investigation of Electrostatic Interactions in Polyelectrolyte Multilayer Films: Binding of Anionic Fluorescent Probes to Layers Assembled onto Colloids. *Macromolecules*, 32(7):2317–2328, 1999. ISSN 0024-9297. doi: 10.1021/ma980674i. URL http://dx.doi.org/10.1021/ma980674i. [cited on p. 43]

[144] S.-H. Lee, Y. Roichman, G.-R. Yi, S.-H. Kim, S.-M. Yang, A. van Blaaderen, P. van Oostrum, and D. G. Grier. Characterizing and tracking single colloidal particles with video holographic microscopy. *Opt. Express*, 15(26):18275–18282, Dec 2007. doi: 10.1364/OE.15.018275. URL http://www.opticsexpress.org/abstract.cfm?URI=oe-15-26-18275. [cited on p. 48]

[145] M. Speidel, A. Jonáš, and E.-L. Florin. Three-dimensional tracking of fluorescent nanoparticles with subnanometer precision by use of off-focus imaging. *Opt. Lett.*, 28(2):69–71, Jan 2003. doi: 10.1364/OL.28.000069. URL http://ol.osa.org/abstract.cfm?URI=ol-28-2-69. [cited on p. 48]

[146] Y. Li and E. Wolf. Three-dimensional intensity distribution near the focus in systems of different fresnel numbers. *J. Opt. Soc. Am. A*, 1(8):801–808, Aug 1984. doi: 10.1364/JOSAA.1.000801. URL http://josaa.osa.org/abstract.cfm?URI=josaa-1-8-801. [cited on p. 54]

[147] Y. Li and F.T.S. Yu. Intensity distribution near the focus of an apertured focused gaussian beam. *Optics Communications*, 70(1):1 – 7, 1989. ISSN 0030-4018. doi: http://dx.doi.org/10.1016/0030-4018(89)90197-1. URL http://www.sciencedirect.com/science/article/pii/0030401889901971. [cited on pp.]

[148] M. J. Nasse and J. C. Woehl. Realistic modeling of the illumination point spread function in confocal scanning optical microscopy. *J. Opt. Soc. Am. A*, 27(2):295–302, Feb 2010. doi: 10.1364/JOSAA.27.000295. URL http://josaa.osa.org/abstract.cfm?URI=josaa-27-2-295. [cited on pp.]

[149] James B. Pawley, editor. *Handbook Of Biological Confocal Microscopy*, chapter Aberrations in Confocal and Multi-Photon Fluorescence Microscopy Induced by Refractive Index Mismatch. Springer US, 2006. [cited on p. 54]

[150] A. Kyrsting, P. M. Bendix, and L. B. Oddershede. Mapping 3d focal intensity exposes the stable trapping positions of single nanoparticles. *Nano Letters*, 13(1):31–35, January 2013. ISSN 1530-6984. doi: 10.1021/nl3032263. URL http://dx.doi.org/10.1021/nl3032263. [cited on p. 56]

[151] O. Brzobohatý, M. Šiler, J. Ježek, P. Jákl, and P. Zemánek. Optical manipulation of aerosol droplets using a holographic dual and single beam trap. *Opt. Lett.*, 38(22):4601–4604, Nov 2013. doi: 10.1364/OL.38.004601. URL http://ol.osa.org/abstract.cfm?URI=ol-38-22-4601. [cited on p. 56]

[152] S. Nedev, S. Carretero-Palacios, S. R. Kirchner, F. Jäckel, and J. Feldmann. Microscale mapping of oscillatory flows. *Applied Physics Letters*, 105(16):161113, October 2014. ISSN 0003-6951, 1077-3118. doi: 10.1063/1.4900483. URL http://scitation.aip.org/content/aip/journal/apl/105/16/10.1063/1.4900483. [cited on p. 63]

[153] R. Calhoun, A. Yadav, P. Phelan, A. Vuppu, A. Garcia, and M. Hayes. Paramagnetic particles and mixing in micro-scale flows. *Lab Chip*, 6:247–257, 2006. doi: 10.1039/B509043A. URL http://dx.doi.org/10.1039/B509043A. [cited on p. 63]

[154] M. J. Kim and K. S. Breuer. Enhanced diffusion due to motile bacteria. *Physics of Fluids (1994-present)*, 16(9):L78–L81, 2004. doi: http://dx.doi.org/10.1063/1.1787527. URL http://scitation.aip.org/content/aip/journal/pof2/16/9/10.1063/1.1787527. [cited on p. 63]

[155] K. C. Vermeulen, G. J. L. Wuite, G. J. M. Stienen, and C . F. Schmidt. Optical trap stiffness in the presence and absence of spherical aberrations. *Appl. Opt.*, 45(8):1812–1819, Mar 2006. doi: 10.1364/AO.45.001812. URL http://ao.osa.org/abstract.cfm?URI=ao-45-8-1812. [cited on p. 68]

[156] P. M. Morse. *Vibration and Sound*. McGraw-HillMcGraw-Hill, New York, 2 edition, 1948. URL https://archive.org/details/VibrationAndSound. [cited on p. 69]

[157] G. G. Harris and W. A. van Bergeijk. Evidence that the lateral-line organ responds to near-field displacements of sound sources in water. *The Journal of the Acoustical Society of America*, 34(12):1831–1841, 1962. doi: http://dx.doi.org/10.1121/1.1909138. URL http://scitation.aip.org/content/asa/journal/jasa/

34/12/10.1121/1.1909138. [cited on pp.]

[158] Ad. J. Kalmijn. Hydrodynamic and acoustic field detection. In Jelle Atema, RichardR. Fay, ArthurN. Popper, and WilliamN. Tavolga, editors, *Sensory Biology of Aquatic Animals*, pages 83–130. Springer New York, 1988. ISBN 978-1-4612-8317-1. doi: 10.1007/978-1-4612-3714-3_4. URL http://dx.doi.org/10.1007/978-1-4612-3714-3_4. [cited on p. 69]

[159] N. Riley. On a sphere oscillating in a viscous fluid. *The Quarterly Journal of Mechanics and Applied Mathematics*, 19(4):461–472, 1966. doi: 10.1093/qjmam/19.4.461. URL http://qjmam.oxfordjournals.org/content/19/4/461.abstract. [cited on p. 71]

Acknowledgments

The last years have been a wonderful time for me, both scientifically and personally. Many people were involved in this and I would like to thank every one of them for their friendship, help, time, guidance and understanding.

Professor **Jochen Feldmann**, my doctoral thesis supervisor and group leader, I would like to thank for giving me the opportunity to conduct my research here in this group. I have greatly benefited from the support he provided, the highly productive discussions we had and the chances he gave me to present my work and meet other scientists at high level conferences. During my time here, he has helped me to become a better scientist. I am very grateful for the excellent scientific environment I encountered during my time here.

Dr. **Sol Carretero-Palacios** for the high throughput, enjoyable discussions of physics at all levels and for the great contributions in both of the scientific papers of which this thesis is based on.

Dr. **Lindsey Anderson** for the high throughput, enjoyable discussions on the elevator paper and for showing me how a paper can be written in a very accessible and clear way.

Dr. **Frank Jäckel**, for giving me an excellent example of how a scientist should be organised.

Thanks to Dr. **Frank Jäckel**, Dr. **Michael Carlson**, Dr. **Alexander Urban** and Dr. **Lindsey Anderson** for the great support on correcting this dissertation.

Here I want to thank my colleagues **Paul Kühler** and **Dr. Jaekwon Do** for the great fun we had in the workshops we attended together.

Many thanks to Dr. **Silke Kirchner** for her constant support during my days as PhD student.

Everyone else from this group with whom I had the pleasure to work and relax with.